Quantum States of Neutrons in the Gravitational Field

Claude Krantz

January 2006

Quantum States of Neutrons in the Gravitational Field: We present an experiment performed between February and April 2005 at the *Institut Laue Langevin* (ILL) in Grenoble, France. Using neutron detectors of very high spatial resolution, we measured the height distribution of ultracold neutrons bouncing above a reflecting glass surface under the effect of gravity. Within the framework of quantum mechanics this distribution is equivalent to the absolute square of the neutron's wavefunction in position space.

In a detailed theoretical analysis, we show that the measurement is in good agreement with the quantum mechanical expectation for a bound state in the Earth's gravitational potential. We further demonstrate that the results can neither be explained within the framework of a classical calculation nor under the assumption that gravitational effects can be neglected. Thus we conclude that the measurement manifests strong evidence for quantisation of motion in the gravitational field as is expected from quantum mechanics and as has already been observed in another type of measurement using the same experimental setup.

Finally, we study the possibilities of using the mentioned position resolving measurement in order to derive upper limits for additional, short-ranged forces that would cause deviations from Newtonian gravity at lenght scales below one millimeter.

Quantenzustände von Neutronen im Gravitationsfeld Es wird ein Experiment vorgestellt, das von Februar bis April 2005 am *Institut Laue Langevin* (ILL) in Grenoble, Frankreich, durchgeführt wurde. Dabei wurde mit Hilfe von Neutronendetektoren mit sehr hoher Ortsauflösung die Höhenverteilung ultrakalter Neutronen gemessen, die unter dem Einfluss der Schwerkraft über einer reflektierenden Glasoberfläche hüpfen. In der Quantenmechanik entspricht diese Höhenverteilung dem Betragsquadrat der Ortswellenfunktion eines Neutrons.

Eine genaue Analyse der Messdaten ergibt, dass sich diese in guter Übereinstimmung mit der quantenmechanischen Erwartung für einen gravitativ gebundenen Zustand befinden. Es wird gezeigt, dass die Messergebnisse weder rein klassisch, noch unter Vernachlässigung des Schwerepotentials beschreiben werden können. Aus dieser Tatsache wird geschlossen, dass das Experiment starke Hinweise auf eine Quantisierung der Bewegung im Gravitationsfeld liefert, wie sie von der Quantenmechanik vorhergesagt wird und in systematisch anderen Messungen mit dem selben experimentellen Aufbau bereits nachgewiesen wurde.

Schließlich wird untersucht, inwiefern aus besagten ortsauflösenden Messungen Obergrenzen für zusätzliche, kurzreichweitige Kräfte abgeleitet werden können. Solche Kräfte würden – bei Abständen unterhalb eines Millimeters – Abweichungen vom Newton'schen Gravitationsgesetz bewirken.

Contents

Introduction

What is gravity? In many respects this may be one of the most important questions ever asked. Answers to it have always been milestones on the way from ancient natural philosophy to modern science. Every physicist knows the legendary free fall experiments of Galileo Galilei at the dawn of empiricism, forshadowing Newton's later formalism of the attraction of masses, itself the very starting point of modern physics and science as a whole.

Since then, our comprehension of nature has changed. And paradoxally, the question that triggered it all is still one of the most obscure. The Standard Models of Cosmology and Particle Physics describe our world up to its largest and down to its smallest scales. Doubtlessly, both of these theories deserve being considered among the grandest cultural achievements in the history of mankind. Yet, they stand separate. The presently adopted view of gravity is provided by Einstein's General Theory of Relativity and has been unchallenged for almost a century. During this time, particle physics has firmly established that the three non-gravitational interactions are governed by the principles of quantum physics, which are inherently incompatible to the classical field concept of General Relativity. The latter is therefore expected to, sooner or later, have to be replaced by a quantised theory of gravity.

Since 1999, an experiment at the *Institut Laue Langevin* in France is redoing Galilei's free fall experiments using as probe mass an elementary particle: the neutron. Although earlier attempts using atoms have been undertaken, this experiment is the first to have detected quantum states in the gravitational field by observing, at very high spatial resolutions, the motion of ultracold neutrons under the effect of gravity [Nesv02]. Its results may be considered as a first timid step on the way to bridge the gap separating gravitation and quantum physics.

This diploma thesis presents a further measurement performed in 2005 using the mentioned experiment. By means of position resolving detectors, we directly imaged the height distribution of neutrons bouncing, under the effect of gravity, a few tens of micrometers above a reflecting surface. Within the framework of quantum mechanics, this distribution is equivalent to the absolute square of the neutron's wavefunction in position space.

In a first chapter of this text, we develop the basic concepts of quantised motion of an elementary particle in the field of gravity as they can be derived from quantum mechanics. Additionally, we provide the fundamentals of neutron physics as far as they are relevant to our experiment. Special attention is payed to the unique properties of ultracold neutrons, without which the mentioned measurement would be impossible to realise. The latter is throughoutly described in chapter 2, where we give an overview of the experimental techniques put into operation and discuss the data taking processes.

The main focus of this thesis lies on chapter 3, where we further develop the results from the first chapter into a detailed theoretical description of the experiment and the measurement process. Within the framework of quantum mechanics, this yields a prediction of the density distribution of low-energetic neutrons bouncing under the effect of gravity. In order to rule out possible misinterpretations of the data, we subsequently oppose this quantum mechanical expectation to two alternative ones described in chapter 4: The first neglects the effects of quantum mechanics, the second those of gravity. All three models are compared to the neutron height distributions that have actually been measured.

Over the last years, a number of theories have arisen which, in an effort to derive a quantum description of gravity, predict deviations from the Newtonian gravitational potential at length scales below one millimeter [Ark98] [Ark99]. Thus, in a last chapter, we study possible upper limits on such deviations that could be obtained from the type of measurement we have performed.

Chapter 1

Ultracold Neutrons and Gravity

1.1 The Neutron

Over the last decades the neutron has has become a tool of ever increasing importance to both the fields of fundamental and applied physics.

With a rest mass $m = 939.485(51)$ MeV/c^2, the neutron is the second-lightest member of the baryon octet. As such, it can in principle be used to probe all four of the fundamental interactions. While this is not astonishing in itself, there are a few notable properties that do make the neutron special among all baryons: It is electrically neutral, easy enough to produce and sufficiently long-lived to be a very practical probe particle.

Additionnally, neutrons may be *cooled* down to kinetic energies of less than 1 meV, which are then of the same order of magnitude than the potentials of their fundamental interactions. At the latter we will have a closer look in the following subsection.

1.1.1 Fundamental Interactions

Neutrons are *electrically neutral.* In the valence quark model, the neutron consists of one up and two down quarks and therefore carries an electric charge equal to 0. The most precise measurement of the neutron charge was performed by Gähler *et al.* by observing the deviation of a neutron beam in an electrostatic field [Gähl89]. The experiment yields

$$q_{\mathrm{n}} = (-0.4 \pm 1.1) \cdot 10^{-21}\ e$$

with e being the electron charge magnitude. It's neutrality renders the neutron immune to otherwise all-overwhelming electromagnetic forces and ensures the possibility to probe other, weaker interactions on low energy scales. It makes the neutron the particle of choice for low-energy physics [Abe02], in contrast to its charged counterpart the proton, typically used in high-energy experiments which overcome the dominion of electromagnetism at the expense of enormous energy densities.

This having been said, the neutron does take part in electromagnetic interactions through its *magnetic moment* $\vec{\mu}_\mathrm{n}$. It's interaction potential with an external magnetic field $\vec{B}$ reads

$$V_\mathrm{mag} = -\vec{\mu}_\mathrm{n} \cdot \vec{B} \ .$$

The neutron magnetic moment is proportional to the *nuclear magneton* $\vec{\mu}_\mathrm{N}$:

$$\vec{\mu}_\mathrm{n} = -1.9130427(4)\ \vec{\mu}_\mathrm{N}$$

itself linked to the proton mass m_p

$$\mu_\mathrm{N} = |\vec{\mu}_\mathrm{N}| = \frac{e\hbar}{2m_\mathrm{p}} \approx 3.152 \cdot 10^{-8}\ \mathrm{eV/T} \ .$$

Thus a neutron inside an exterior magnetic field has got a potential energy of

$$V_\mathrm{mag} \approx 60\ \mathrm{neV/T}.$$

Weak interaction manifests itself most notably through the fact that the free neutron is unstable. It decays spontaneously into a proton, an electron and an anti-electron-neutrino:

$$\mathrm{n} \longrightarrow \mathrm{p} + \mathrm{e}^- + \bar{\nu}_\mathrm{e} \qquad (+782\ \mathrm{keV}) \ . \tag{1.1}$$

Since the proton is the only baryon with lower rest mass than the neutron and since the energy release is to low to produce heavy leptons, there are no other decay channels. The decay being governed by weak interaction, the mean lifetime of a neutron is still quite long. The world average value as of 2004 is [Pdg04]

$$\tau_\mathrm{n} = (885.7 \pm 0.8)\ \mathrm{s}$$

This time is long enough to provide the opportunity to use neutrons in low-energy storage experiments.

Being, alongside with the proton, the constituent of atomic nuclei, the neutron obviously also takes part in *strong interactions.* A free neutron may be scattered at or absorbed into the strong potential of a nucleus. Neutrons coupling only very weakly to electromagnetic fields, strong scattering is the standard way of manipulating them. With the help of suitably crafted strong potentials, neutrons may be reflected at surfaces, guided along tubes, cooled or heated into predefined kinetic energy spectra.

Strong interaction is also the key to *neutron detection*: Particle detectors are typically sensitive to ionising particles only. The neutron being electrically neutral, it usually needs to be *converted*, i.e. absorbed into a nucleus which in turn reacts by either emission of γ-rays or charged particles. These can then be detected through their electromagnetic interaction with surrounding matter.

Within the framework of this text, we are mainly interested in *gravitational interaction* of neutrons with the Earth. Given its mass $m = 1.67495 \cdot 10^{-27}$ kg [Pdg04], a neutron's potential energy as a function of altitude z evaluates to

$$V(z) = mgz \approx 100 \frac{\mathrm{neV}}{\mathrm{m}} \cdot z[\mathrm{m}]$$

For a neutron, a kinetic energy of 100 neV corresponds to a velocity $v \approx 2.2$ m/s. This means that slow neutrons may be significantly accelerated or decelerated by falling or raising in the Earth's gravitational field. It is noteworthy that gravity can easily be the strongest long-ranged interaction affecting the neutron. The strong interaction being short-ranged and V_{mag} being weak and easily controlled by magnetic shielding, low energetic neutrons are prime candidates for the observation of gravitational effects in systems formed by elementary particles. The quantum mechanics arising from this will be discussed in quite extensive a manner in section 1.2.

1.1.2 Ultracold Neutron Production

As indicated above, *free* neutrons have a lifetime of approximately a quarter of an hour. There is therefore little hope of finding them in large quantities in nature as is true for protons and electrons which are readily available in the form of hydrogen. Neutrons naturally only occur tightly packed in degenerate, strongly-interacting Fermi gases. In such systems it is possible that the β-decay (1.1) would be net *endothermic* and therefore cannot take place. Nature manifests two realisations of this situation: In *atomic nuclei* both neutrons and protons form degenerate Fermi gases bound in their common strong potential well. For stable (i.e. non-β-active) nuclei the energy amount required in order to add a proton to the system is greater than the 782 keV released by the reaction (1.1), as a result, the decay is thermodynamically prohibited. At sufficiently high matter densities, the strong binding potential may be replaced by a gravitational one. Inside *neutron stars*, remnants of red supergiants, neutrons are subject to gravity fields so intense that the increase in volume of the system related to neutron decay would require a rise in gravitational potential energy of more than 782 keV. With diameters of order ten kilometres, such stars therefore almost exclusively consist of neutrons with no possibility to decay.

For obvious reasons neutron stars could never be very practical devices for laboratory use. The spectrum of possible *neutron sources* for experimental ends therefore reduces to atomic nuclei. There are a number of isotopes (e.g. ^{252}Cf) that produce free neutrons through spontaneous fission reactions. Such sources are small and easy to maintain but of low intensity. In order to get high neutron fluxes, one has to turn towards sources involving *induced* nuclear reactions. Among these there are two main types: *Spallation* sources consist of a particle accelerator 'firing' onto a target made of heavy nuclei. Given a suitable choice of isotopes, the incident particle is absorbed into the target nucleus which reacts to this excitation by evaporation of neutrons. Although several spallation sources worldwide are expected to come into operation in the near future, any powerful neutron sources available today provide stimulated neutron emission through the use of *nuclear fission reactors*.

The neutron source of the *Institut Laue-Langevin* (ILL) located in Grenoble (France), at which the experiment described hereafter was performed, is of this latter type. We shall therefore explain the production of neutrons on the basis of this particular setup depicted in figure 1.1. Independently of the reaction being spontaneous or induced, neutrons emerging from a nuclear fission process will always carry high kinetic energies of order 1 MeV. The core of the reactor at the ILL consists of a highly-enriched uranium fuel element immersed into a heavy water tank. Each fission reaction produces an average number of 2.4 neutrons. Close to the core the neutron flux density is of the order of 10^{15} cm^{-2}s^{-1}. By strong scattering at the deuterons contained in the heavy water (D_2O), these high energetic neutrons are *thermalised*, i.e. the temperature of the neutron gas adapts itself to that of the D_2O-moderator which is kept at a constant value of 300 K by heat-exchange with a light water reservoir.

One part of these *thermal neutrons* is used up in the production of further fission reactions in the fuel material, the other part is piped through neutron guides towards the instrumentation halls surrounding the reactor building. Having energies around 25 meV, corresponding to wavelengths of approximately 2 Å, these neutrons are mainly used in scattering experiments of solid state physics.

For some types of experiments slower neutrons are needed. In a "cold source", another, smaller moderator tank filled with liquid deuterium (D_2) cooled down to 25 K, the neutrons are further decelerated to have energies of approximately 2 meV and are then called *cold neutrons*.

Experiments like the one to be described in this text rely on neutrons of even much lower energy: *Very cold neutrons* (VCN, few μeV) and *ultracold neutrons* (UCN, below 0.3 μeV). These cannot be obtained through thermalisation but have to be *selected* from the lowest energetic tail of the cold Maxwellian spectrum. This is done by vertically extracting the neutrons using a *curved* guide (see figure 1.1). The curvature ensures that incident angles of neutrons onto the guide's walls are

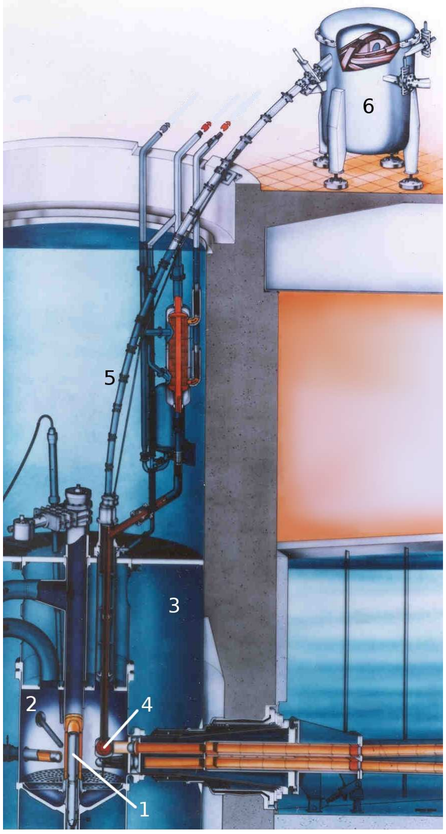

Figure 1.1: The UCN source at the ILL: The illustration shows the fuel element (1), the D_2O-moderator tank (2) itself immersed into the light water tank (3), the cold source (4) from which cold neutrons are vertically extracted and piped through the curved VCN guide (5) and the turbine (6) feeding UCN experiments. (picture taken from *www.ill.fr*)

large. Neutrons with velocities above a threshold v_{max} are unable to follow the guide as they will penetrate the wall material rather than be reflected at its surface. At the exit of the curved guide, located 13 m above the cold source, only very cold and ultracold neutrons are present.

The particle density in the UCN part of the spectrum is then enhanced by means of the so-called UCN turbine. The turbine consists of 690 nickel coated blades revolving inside a vacuum chamber connected to the curved guide in such a way that they recede from the VCN beam at half the speed of the arriving neutrons. Upon collision with the blades VCN therefore loose longitudinal momentum in the laboratory frame and are slowed down into the UCN regime. It should be emphasised that the turbine cannot enhance the phase space density in the UCN energy interval above its value inside the cold source. This is in agreement with Liouville's theorem: In a thermodynamically closed system, the phase space density is constant for all times. The turbine is therefore designed to only repopulate the phase space volume of UCN that have been lost on their way from the cold source.

1.1.3 Interaction of Ultracold Neutrons with Surfaces

Ultracold neutrons have the faculty of being totally reflected at a wide range of material surfaces under *any* incident angle. As this unique feature is of crucial importance to the experiment discussed hereafter, we want to gain some insight into the underlying principles. As indicated above, the dominating effect in the interaction of neutrons with matter is strong scattering between neutrons and atomic nuclei.

Let us sketch very briefly the mechanism of scattering at a nucleus, a detailed calculation can be found e.g. in [Gol91]: An ultracold neutron with kinetic energy $E \leq 100$ neV is characterised by a de Broglie wavelength of

$$\lambda = \frac{h}{\sqrt{2mE}} \geq 90 \text{ nm} . \tag{1.2}$$

The strong potential of a nucleus can be approximated by a spherical square well potential:

$$V_{\text{nuc}}(r) = \begin{cases} -V_0 & : \quad r \leq R \\ 0 & : \quad r > R \end{cases} \tag{1.3}$$

The strong interaction being very short ranged, R is about equal to the radius of the nucleus of order 1 fm and the depth of the well V_0 is approximately 40 MeV. If we represent the incident neutron by a plane wave, the overall wave function in free space has got the form

$$\psi = \mathrm{e}^{\mathrm{i}\vec{k}\cdot\vec{r}} + f(\theta)\,\frac{\mathrm{e}^{\mathrm{i}kr}}{r} \tag{1.4}$$

as derived in any standard text on quantum mechanics [Schwa98]. We call θ the scattering angle and $f(\theta)$ the *scattering amplitude* which contains the matrix element of the interaction and thereby depends on the shape of the potential $V_{\text{nuc}}(r)$. However, because of $\lambda \gg R$, we expect the reflected wave to be of spherical shape (s-wave scattering), which means that $f(\theta)$ will not contain any angular dependence:

$$f(\theta) = -a . \tag{1.5}$$

We call a the *scattering length* of the nucleus. It is obvious that a has to have the dimension of a length as from scattering theory one derives that $|f|^2$ is the differential cross-section of the process:

$$\frac{\mathrm{d}\sigma}{\mathrm{d}\Omega} = |f(\theta)|^2$$

In our case f is independent of the solid angle and the *total scattering cross-section* reads

$$\sigma_{\text{tot}} = 4\pi a^2 \ .$$

The question arises how to link the measurable quantity a to the scattering potential $V_{\text{nuc}}(r)$. It is in principle not possible to use perturbation theory to describe the scattering process, as the perturbation V_0 is much larger than the neutron energy E. However, the range of the potential $V_{\text{nuc}}(r)$ is limited to R and we are only interested in the shape of the wave function at $r \gg R$, i.e. well outside the range of interaction, where the wave function can be assumed to be only lightly disturbed. In 1936 Fermi found that under these circumstances $V_{\text{nuc}}(r)$ may be replaced by an effective, delta-shaped potential [Gol91]

$$U_F(r) = \frac{2\pi\hbar^2 a}{m}\delta^{(3)}(\vec{r}) \ , \tag{1.6}$$

where m is the mass of the scattered neutron and a the scattering length. Named *Fermi Potential* after it's creator, U_F permits to compute the scattering matrix elements in the Born approximation.

A slow neutron impinging onto condensed matter will now feel the superposition of the nuclei's individual Fermi potentials:

$$U(\vec{r}) = \frac{2\pi\hbar^2}{m}\sum_i a_i \delta^{(3)}(\vec{r} - \vec{r}_i) \ . \tag{1.7}$$

At each $\vec{r}_i$ scattering produces a spherical reflected wave. For ultracold neutrons, the wavelength λ 3 orders of magnitude larger than the distances separating the nuclei. Interaction will therefore take place through a large number of simultaneous scattering processes and equation (1.7) can be approximated by a homogeneous Fermi potential

$$U(\vec{r}) \approx U = \frac{2\pi\hbar^2}{m} \cdot \bar{a} \cdot n \ ,$$

where the sum over the δ-distributions has been replaced by the *particle density* n of the material and $\bar{a}$ is the averaged scattering length of the nuclei. U may be regarded as a *macroscopic* property of the material. In the last step we have thereby reduced our complicated scattering problem to a very simple and yet quite correct mathematical description. The normal motion component of a neutron hitting a smooth material surface can now be described as one dimensional scattering of a free particle state at a step potential. For a large variety of materials, $|U|$ is larger than the typical energy of an ultracold neutron ($\leq$ 100 neV). Their surfaces then correspond to potential barriers impenetrable to the particles.

In the experiment discussed hereafter, neutrons bounce above glass surfaces. Optical glass essentially consists of silicon dioxide which is characterised by a Fermi potential of

$$U_{\text{glass}} \approx 100 \text{ neV}.$$

Thus *ultracold* neutrons can safely be assumed to be totally reflected at its surface.

In fact, UCN may even be defined as being those neutrons which are totally reflected from the inner walls of neutron guides *at all angles of incidence.*

1.2 Gravity and Quantum Mechanics

The experiment discussed hereafter measures the gravitational free fall of neutrons over very small length scales. The dynamics of low-energetic elementary particles being naturally governed by non-relativistic quantum mechanics, we are therefore facing the problem of solving the Schrödinger equation in the case of a gravitational potential.

Although we shall later have to refine and generalise the results obtained from the following treatment and although the problem of a linear potential is throughoutly discussed in many standard texts on quantum mechanics [Flü99], it is useful to address it at this early stage as it allows us to develop most of the concepts needed in the later chapters of this text.

1.2.1 The Schrödinger Equation

Consider a system formed by the Earth and a particle gravitationally bound to it. Let M_E and m be the masses of Earth and particle respectively. According to Newton's Law, the potential energy of such a system is

$$\tilde{V}(r) = -G\,\frac{M_E\,m}{r}\ , \tag{1.8}$$

where r denotes the distance separating the two centres of mass and G the gravitational constant. We are interested in the case where the particle is located at a height z above the surface of the Earth which is very small compared to the planet's radius R_E:

$$r = R_E + z \quad \text{with} \quad z \ll R_E$$

Equation (1.8) can then be expanded up to the first order in z:

$$\tilde{V}(z) \approx \underbrace{-G\frac{M_E\,m}{R_E}}_{=\tilde{V}(R_E)} + \underbrace{G\frac{M_E}{R_E^2}}_{=:g}\,mz \tag{1.9}$$

Dropping the additive constant to the left, we finally write

$$V(z) = mgz \ ,$$

where g is the Earth's *gravitational acceleration* at sea level as defined in equation (1.9). The Hamiltonian of the above system therefore writes

$$\mathcal{H} = \frac{p^2}{2m} + mgz \ .$$

It may be worth pointing out that in the last step we have identified inertial and gravitational mass, i.e. we assume that the Weak Equivalence Principle holds for our system.

This leads to the following time-independent Schrödinger equation for the particle's probability amplitude in position space $\psi(z)$:

$$\left(-\frac{\hbar^2}{2m}\frac{\partial^2}{\partial z^2} + mgz\right)\psi(z) = E\ \psi(z) \tag{1.10}$$

In order to simplify mathematical expressions, it is useful and quite common to introduce a *scaling factor* R given by

$$R := \left(\frac{\hbar^2}{2m^2 g}\right)^{1/3} \tag{1.11}$$

and to define the dimensionless quantities

$$\zeta := \frac{z}{R}\ ; \quad \epsilon := \frac{E}{mgR}\ . \tag{1.12}$$

Substituting $z \longrightarrow \zeta$ and $E \longrightarrow \epsilon$ in equation (1.10) yields

$$\left(-\frac{\hbar^2}{2m}\frac{1}{R^2}\frac{\partial^2}{\partial \zeta^2} + mgR\zeta\right)\psi(\zeta) = mgR\epsilon\ \psi(\zeta)\ ,$$

and according to the definition (1.11) of R this leads to the following dimensionless eigenvalue equation:

$$\boxed{\left(-\frac{\partial^2}{\partial \zeta^2} + (\zeta - \epsilon)\right)\psi(\zeta) = 0} \tag{1.13}$$

1.2.2 Airy Functions

The differential equation (1.13) is well known in mathematics. Its eigenfunctions are linear combinations of the *Airy Functions* Ai and Bi. The Airy Functions are transcendental mathematical objects which can be expressed in terms of Bessel Functions. For our purposes, we may safely regard them as 'normal' real-valued functions with the two notable properties depicted in figure 1.2:

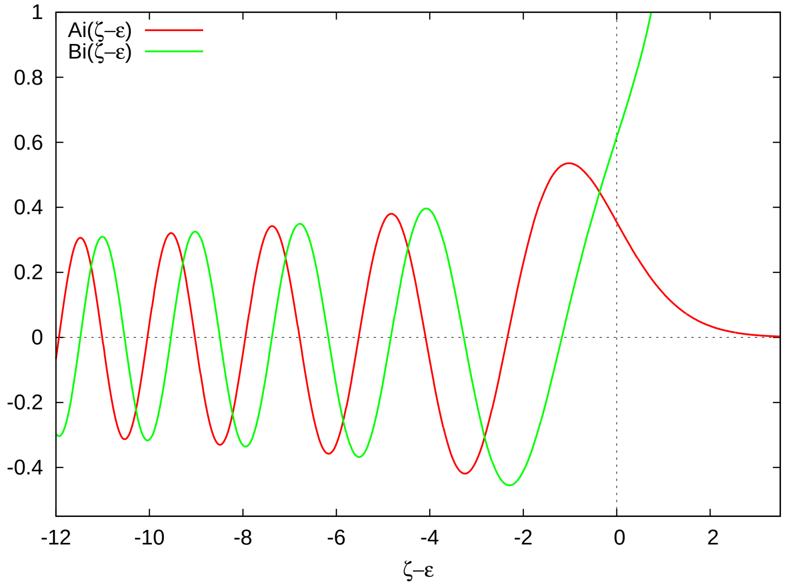

Figure 1.2: The Airy Functions Ai and Bi

1. For $\zeta \to -\infty$ both Ai and Bi manifest a $\sin(\zeta)$-like oscillating behaviour.
2. For $\zeta \to +\infty$ their behaviours are radically different: Ai *converges* exponentially fast towards 0 while Bi *diverges* at the same pace.

Armed with this knowledge, we can return to our Schrödinger equation. The most general solution $\psi(\zeta)$ of (1.13) has the form:

$$\psi(\zeta) = c_A \, \mathrm{Ai}(\zeta - \epsilon) + c_B \, \mathrm{Bi}(\zeta - \epsilon) \tag{1.14}$$

As usual in quantum mechanics, the possible values for the coefficients c_A and c_B are determined by the boundary conditions of the system at hand. We shall have to return to this point at a later stage but, for now, let us consider the case of the particle falling freely above a reflecting floor placed at $z = 0$. In addition, the wave function must be normalisable in order to be a Hilbert-vector. Thus we request

$$\psi(\zeta) = 0 \qquad (\zeta \leq 0) \tag{1.15}$$

$$\psi(\zeta) \to 0 \qquad (\zeta \to +\infty) \tag{1.16}$$

This system is often referred to as the 'quantum bouncer'. Because of

$$\lim_{\zeta \to +\infty} \mathrm{Bi}(\zeta - \epsilon) = +\infty$$

the latter condition can only be fulfilled by setting

$$c_B = 0 \; .$$

Together with the boundary at $z = 0$, this means that eigenstates of our system have got the form

$$\psi(\zeta) = \begin{cases} N^{-1}\mathrm{Ai}(\zeta - \epsilon) & : \quad \zeta > 0 \\ 0 & : \quad \zeta \leq 0 \end{cases}$$

where N^{-1} is a factor ensuring the normalisation of the functions. Derivability of the solution at $\zeta = 0$ requires

$$\mathrm{Ai}(-\epsilon) = 0 \ . \tag{1.17}$$

Because of the oscillatory nature of Ai, this means that only particular $\epsilon \in \{\epsilon_n\}$ are allowed. Recalling that $E = mgR\epsilon$, we see from equation (1.17) that our system is characterised by a *discrete* energy spectrum as expected for any quantum mechanical bound state.

1.2.3 The WKB Approximation

Ai being a transcendental function, solutions to equation (1.17) can be found by numerical computation alone. However a very good approximation for the ϵ_n can be given using the Wentzel-Kramers-Brillouin (WKB) method. A detailed description of the procedure can be found e.g. in [Rueß00]. It yields

$$\epsilon_n^{\mathrm{WKB}} = \left[\frac{3\pi}{2}\left(n - \frac{1}{4}\right)\right]^{2/3} \quad ; \ n \in \mathbb{N}^* \tag{1.18}$$

The relations (1.12) can be used to express the energy spectrum in physical units

$$E_n^{\mathrm{WKB}} = mgR\epsilon_n^{\mathrm{WKB}} =: mgz_n \ , \tag{1.19}$$

where the entity $z_n = \epsilon_n^{\mathrm{WKB}} R$ corresponds to the *classical* jump height of a pointlike particle with energy E_n. The final result for the solutions of the Schrödinger equation (1.10) with the boundary conditions given by (1.15) and (1.16) reads

$$\boxed{\psi_n^{\mathrm{WKB}}(z) = \begin{cases} N^{-1}\mathrm{Ai}\left(\frac{z}{R} - \epsilon_n^{\mathrm{WKB}}\right) & : \quad z \geq 0 \\ 0 & : \quad z < 0 \end{cases}} \ . \tag{1.20}$$

Since the WKB method is a semi-classical approximation, one could expect it to be valid only in the limit of very high quantum numbers n. However the energies obtained from (1.18) turn out to deviate from the true eigenvalues by no more than one percent even for the lowest states. In table (1.1) the WKB eigenvalues of the first eigenstates as given by (1.18) are compared to those obtained from a numerical solution of equation (1.17).

Both eigenstates and eigenvalues to the Schrödinger equation (1.10) having been found, the 'quantum bouncer' is now solved. Adopting the values

$$m = 1.67495 \cdot 10^{-27} \ \mathrm{kg} \quad \text{and} \quad g = 9.80665 \ \mathrm{m/s^2}$$

n	E_n^{true} [peV]	E_n^{WKB} [peV]	$\Delta E/E_n^{\text{true}}$ [%]
1	1.4067	1.3960	0.76
2	2.4595	2.4558	0.15
3	3.3215	3.3194	0.06
4	4.0832	4.0819	0.03
5	4.7796	4.7786	0.02

Table 1.1: True eigenvalues compared to their WKB approximations

for the neutron mass and the gravitational acceleration, equation (1.20) gives the probability amplitude in position space for the free-falling particle for a given quantum number n. Figure 1.3 depicts the shapes of the wavefunctions for the first three quantum states.

1.2.4 Remarks

On the Scaling Factor R: In the case of a free falling neutron as described above, the scaling factor R, defined by equation (1.11), evaluates to

$$R \approx 5.87\ \mu\text{m} .$$

It is the *characteristic length scale* of the system and closely related to the Heisenberg Uncertainty Principle, as can be seen as follows [Abe05]: The uncertainty relation for position and momentum reads

$$\Delta z \Delta p \geq \frac{\hbar}{2} . \tag{1.21}$$

If we identify the uncertainty of the momentum p with its maximum value and the uncertainty of the position with the classical jump height of the particle, we can write

$$\Delta p = p_{\max} = \sqrt{2mE} = \sqrt{2m^2 g \Delta z}$$

Inserting this into (1.21) leads to

$$\Delta z^{3/2} \sqrt{2m^2 g} \geq \frac{\hbar}{2}$$

or

$$\Delta z \geq \left(\frac{\hbar^2}{8m^2 g} \right)^{1/3} = 4^{-1/3}\ R .$$

Hence, up to a numerical factor of magnitude $\mathcal{O}(1)$, R is equal to the position uncertainty of the bound particle.

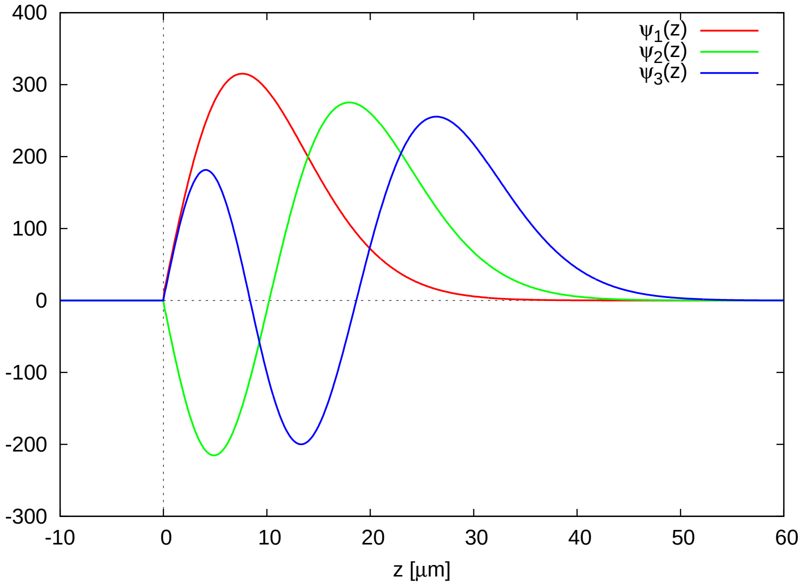

Figure 1.3: The probability amplitudes in position space for the first three eigenstates ψ_n^{WKB} of the 'quantum bouncer'

On Gravitationally Bound States: In connection with the 'quantum bouncer' it is often stated that quantisation of energies arises because the particle is *confined* inside a cavity formed by the gravitational potential and the potential barrier of the reflecting floor which we have taken to be infinitely high. This potential well is depicted in figure 1.4.

In the above treatment, quantisation indeed arose due to the introduction of the boundary condition (1.15). However this does *not* mean that the absence of a reflecting floor would result in a continuous energy spectrum. The mathematical need for a confining potential barrier actually arises from the Taylor expansion (1.9) of the potential $\tilde{V}(r)$ which is valid for small absolute values of z only:

$$\tilde{V}(z) \approx -G\frac{M_E\, m}{R_E} + G\frac{M_E\, m}{R_E^2}\, z \ .$$

It is perfectly possible to solve the Schrödinger equation without this limitation, by directly plugging $\tilde{V}(r)$ from equation (1.8) into it. We would then get the standard $1/r$ central potential problem well-known from the quantum mechanics of the hydrogen atom. With r being the distance separating the centre of the Earth and the free falling neutron, the particle's probability amplitude would then be of the form [Schwa98]

$$u_{n,l}(r) \sim r^{l+1} \mathrm{e}^{-\kappa r} L_{n+1}^{2l+1}(2\kappa r) \ ,$$

where n and l are the principal and angular momentum quantum numbers and L

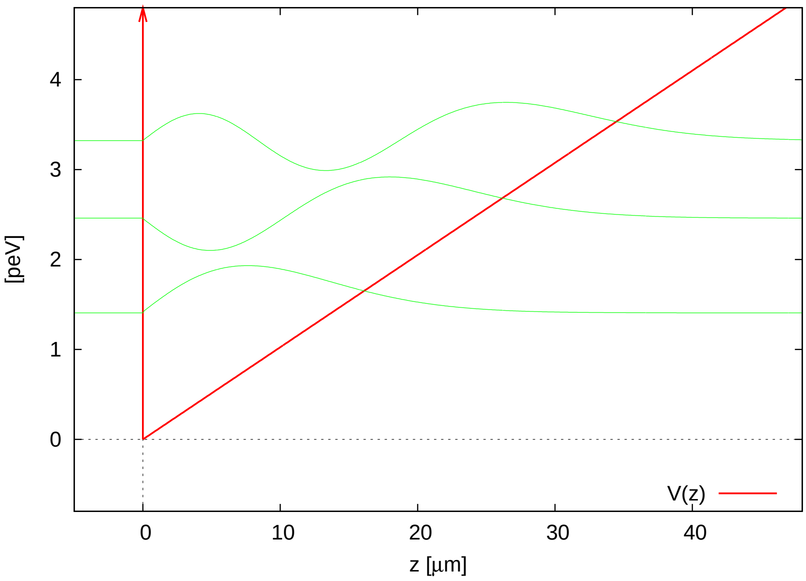

Figure 1.4: The potential well confining the particle and the first three eigenstates

denotes the Associated Laguerre Polynomials. The case of a particle located close to R_E would then just correspond to a very high value of n. It can be shown that for large values of n and r, $u_{n,l}(r)$ is well approximated by the Airy function Ai we have found under the assumption of a perfectly linear potential.

In classical mechanics one derives parabolic trajectories for free-falling pointlike masses. In fact these are correct only in the case of not-too-high falling altitudes, the general solutions of the problem being Kepler ellipses. In the very same way one might state that the solutions (1.20) are approximations of bound central potential states valid in the *homogenous field limit* (1.9).

Chapter 2

The Experiment

In the preceding chapter we have discussed the behaviour of an elementary particle subject to a linear gravitational potential as it is expected from quantum mechanics. Since 1999 our experiment at the *Institut Laue Langevin* (ILL) analyses this phenomenon empirically by observing the motion of ultracold neutrons falling onto totally reflecting glass mirrors at very high spatial resolutions of the order of 1 μm. The following chapter will describe this setup, will provide an overview of the experimental techniques involved and explain the measurement performed within the framework of this diploma thesis in 2005.

2.1 Overview of the Installation

The experimental setup is mounted on the UCN instrumentation platform PF2 of the ILL, located directly above the reactor core as has been described in section 1.1 (see figure 1.1). In an experiment seeking to observe such faint an effect as quantisation in gravitationally bound neutron states, some care obviously needs to be taken in order to protect the setup against mechanical and electromagnetic perturbations omnipresent inside a research reactor.

As shown in figure 2.1 the setup consists of a vacuum chamber build on top of a massive granitic stone table. Accurately polished and plane to very high standards, this stone supports all the critical components of the setup. The system contains two high precision digital inclinometers normally used in geophysics and rests upon three piezo elements. The inclinometers provide information about the setup's current inclination with respect to the horizon. This data is fed into a computer which in turn controls the voltage applied to the piezo elements. Working as a closed loop, this inclination control system can actively correct the pitch of the stone table and

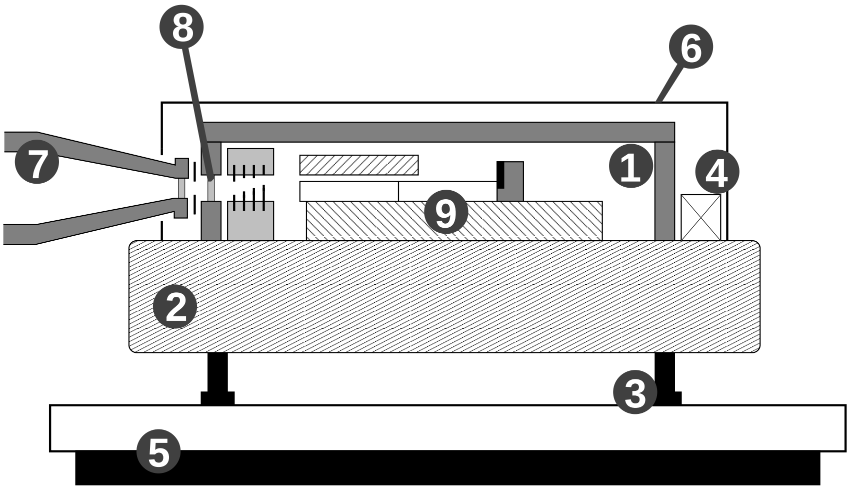

Figure 2.1: Longitudinal section through the installation. Depicted are the vacuum chamber (1), the granitic stone table (2), the piezo legs (3), the inclinometers (4), the optical table (5), the magnetic shielding (6), the end of the neutron guide (7), the aluminium entrance window (8) and the actual experimental setup (9). A detailed view of the latter is shown in figure 2.2.

keep it coplanar to the surface of the Earth with a maximum deviation of 10 μrad or better. However, the active control system can prevent only slow drifts in the system's inclination. In order to provide protection against vibrations and sudden mechanical perturbations the entire installation is based on an optical platform hovering on top of an air cushion.

From section 1.1 we recall that the potential energy of a neutron in an external magnetic field is approximately 10^{-10} eV/mT. In contrast to this we have seen in section 1.2 that energy eigenvalues of the lowest gravitationally bound states of a neutron are of the order of 10^{-12} eV. The setup therefore has to be given some protection against magnetic fields. This is done by wrapping it up into a box made of diamagnetic material (μ-metal), which reduces the field intensity inside the vacuum chamber by many orders of magnitude and ensures that gravity is effectively the only long-ranged interaction felt by a neutron.

The experiment is mounted in close proximity to the UCN turbine (c.f. section 1.1) which provides the necessary supply of ultracold neutrons. The final segment of the neutron guide is designed in order to change the beam cross-section from circular to rectangular shape and fits onto an entrance window in the vacuum chamber covered by a 30 μm thick aluminium foil. This entrance window was designed to be as transparent as possible for neutrons while still being able to withstand the

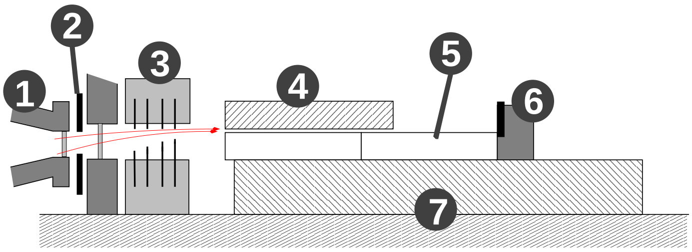

Figure 2.2: Detailed view of the interior of the vacuum chamber: Shown are the UCN guide (1), the collimating blades (2), the static collimator (3), the waveguide consisting of scatterer (4) and bottom mirrors (5), the detector (6) and the supporting glass plate (7). Two possible trajectories of neutrons capable of entering the waveguide are indicated in red.

atmospheric pressure onto it's surface. Because of it's low Fermi potential

$$U_{\mathrm{Al}} \approx 54 \text{ neV}$$

aluminium is the standard material used for neutron windows. Still, UCN with too small a velocity component normal to the metal surface cannot pass it (c.f. section 1.1). If we assume that any neutron with a a kinetic energy of less than U_{Al} will be totally reflected at the window while those with higher energy will pass, the threshold normal velocity component for neutrons entering the vacuum chamber is

$$v_{\perp} \approx 3.2 \text{ m/s}.$$

Additionally, there is a small gap of approximately 1 cm between the end of the neutron guide and the entrance window of the vacuum chamber. Although it further attenuates the beam, this gap is inevitable, as a direct fixation of the guide to the vacuum chamber would make vibration protection impossible.

Up to now, we have focused on the peripherals of the setup, whose aim is simply to screen ultracold neutrons inside the vacuum chamber from all external perturbations but the terrestrial field of gravity. Let us now have a look at the interior of the chamber, where the actual experiment takes place.

2.2 The Waveguide

We want to observe quantum states of ultracold neutrons bouncing above a totally reflecting floor under the effect of gravity, as discussed in chapter 1.2. Physically, the reflecting floor is realised by a set of two optical glass mirrors. The glass is characterised by a positive Fermi potential of around 100 neV. On the other hand we know, from our preceding theoretical treatment, that characteristic energies of vertical motion for the lowest bound states are of the order of a few peV, i.e. 5 orders of magnitude lower. The potential of the glass may therefore as well be considered as infinitely high.

The experimental setup is depicted in figure 2.2. Through the use of a *collimating system*, neutrons arriving from the left of the picture are guided along ballistic trajectories onto the surface of the first of the glass mirrors (5), which they hit at an angle close to zero. The collimating system consists of a static collimator (3) inside the vacuum chamber as well as of two adjustable titanium blades (2) masking part of the entrance window. It will be throughoutly discussed in the next chapter. For the moment we state without proof that the effect of the collimator is that neutrons reaching the glass surface have got *horizontal* velocities of 6-7 m/s while their *vertical* velocities are of the order of a few cm/s only. Thus only a very narrow part of the original, isotropic velocity spectrum delivered by the turbine is selected, which drastically reduces the neutron flux. However this selection is necessary as even the typical energies around 10 neV of ultracold neutrons are several orders of magnitude higher than the energies of the lowest gravitationally bound states.

The *glass mirrors* have sizes of $10 \cdot 10$ cm^2 each and are crafted to the highest standards achievable in order to have surfaces both microscopically smooth and macroscopically plane to very high degrees. In 1999, A. Westphal analysed the surface of a mirror similar to the ones described in this text by means of X-ray scattering [Wes01] [Wes99]. It was found that the root mean square amplitude of the surface roughness was

$$\rho_{\text{mirror}} = (2.20 \pm 0.01) \text{ nm}.$$

This value is perfectly negligible compared to the neutron wavelength of around 100 nm, hence we may safely regard the mirror surfaces as planes in the mathematical sense and assume that UCN hitting them are reflected in a completely specular manner. This allows us to decouple the two components of motion: The *vertical* motion is expected to show the quantum behavior we have derived in section 1.2. The horizontal velocity component of the neutrons, i.e. their motion along the mirrors, is completely unaffected by the setup and corresponds to that of a free particle.

Coplanar to the first bottom mirror, typically placed a few tens of μm above it, we placed the so-called *scatterer* (4). In order to observe quantum effects, we will have to concentrate on the very first few quantum states and it turns out that, even after the severe velocity selection performed by the collimator, neutrons with too high a transverse energy are found on top of the mirror. Using a mechanism known to work but not well understood, the scatterer is supposed to ‘remove’ those neutrons occupying states too high to be useful to discriminate between classical and quantum mechanical dynamics. It is made out of the same optical glass as the bottom mirrors and features the same degree of macroscopic flatness. But, in contrast to the mirrors, it has been treated in order to ensure a large microscopic roughness of it's surface which is thought to scatter impinging neutrons in a totally diffuse manner, such that they are effectively lost to the system. In 2001, the surface of a typical scatterer was imaged by means of an atomic force microscope [Wes01]. The measurement revealed an RMS roughness amplitude of

$$\rho_{\text{scatterer}} = (0.76 \pm 0.02)\ \mu\text{m}.$$

In contrast to the mirror roughness, this value is larger than the typical neutron wavelength which corroborates the diffuse scattering hypothesis. The part of the setup consisting of the two bottom mirrors and the scatterer will hereafter often be referred to as the *'waveguide'*. This term is however not to be understood in the sense it is used e.g. in optics, where it commonly denotes a device that transmits *all* field modes indifferently, without the selection effect that characterises our scatterer/mirror system.

One important aspect of the waveguide is not visible in figure 2.2: The second glass mirror is shifted downwards relative to the first one by 13.5 μm. Neutrons propagating along the mirrors will gain some vertical velocity and thereby energy by falling down this step. Its effect can be completely understood only within the framework of a detailed quantum mechanical treatment to follow in the next chapter, it is however noteworthy that the size of the step has not been chosen randomly: Recalling equation (1.19), we see that it approximately corresponds to the *classical jump height* z_n of the first quantum state:

$$z_1 \approx 13.7\ \mu\text{m}$$

Hence, after passing the step, no neutron will occupy the gravitational ground state, as all will have energies at least equal to the second eigenvalue. A correct mathematical analysis of the system will show that in this regime, the quantum nature of the system will be more pronounced and therefore easier to detect.

After having travelled the 20-cm long mirror surface, neutrons impinge onto a neutron detector (6) mounted directly at the back edge of the second mirror. The experiment uses two types of detectors, both of which can be used in order to measure quantisation of the vertical motion component of neutrons passing the waveguide:

1. A ^{3}He proportional counter is used to measure the integral neutron flux transmitted by the setup.
2. High resolution position sensitive detectors directly measure the neutron's probability density in position space.

While this work heavily focus on the latter type of measurement, both detectors will be presented in the following sections.

2.3 Integral Flux Measurements

One possible way of detecting gravitationally bound quantum states above the mirrors is to vary the waveguide width w, i.e. the height of the scatterer above the first mirror and measure the neutron flux arriving at the end of the second mirror as a function of it. The first such measurement was performed by V. Nesvizhevsky, H. Abele *et al.* in 1999 and has been published in [Nesv02].

The neutron flux was measured using a ^{3}He proportional counter with a thin aluminium entrance window placed directly at the end of the second mirror. As indicated in the preceding chapter neutrons are lacking electric charge and are consecutively incapable of ionising atoms or molecules by interaction with their electronic shells. 'Normal' proportional counters as used in dosimetry of charged particles and γ-rays are therefore insensitive to neutron radiation. This limitation can however be overcome by admixture of a *neutron converter* to the counting gas.

^{3}He is the standard converter for gas proportional counters. A neutron entering the counting volume is absorbed by a ^{3}He nucleus via a neutron capture reaction:

$$\mathrm{n} + {}^3\mathrm{He} \longrightarrow {}^3\mathrm{H} + \mathrm{p} \qquad (+764\ \mathrm{keV})$$

The released energy is carried by the emerging proton and triton and subsequently absorbed into ionisation of counting gas particles. From here on the detection process proceeds as in any proportional counter: The clouds of free charge carriers are accelerated and amplified by an intense electric field and lead to a discharge inside the capacitor enclosing the decay volume. The counting tube used in this experiment was designed by A. Strelkov to have a very low background at a detection efficiency for ultracold neutrons close to 100%.

Figure 2.3 depicts the flux measurement of 1999: The width of the waveguide was varied using a piezo levelling system which permitted to adjust the height of the scatterer above the bottom mirror with an accuracy of about 1 μm. Classically, one would expect the count rate to rise monotonously as the width of the waveguide increases. However the data reveals a threshold behavior: At scatterer heights smaller than

$$w_{\mathrm{thres}} = (13 \pm 2)\ \mu\mathrm{m},$$

the count rate of the detector is constant at background level. It rises noticeably only at slit sizes w larger than 15 μm. This height precisely corresponds to the semiclassical turning point of the first quantum state

$$z_1^{\mathrm{WKB}} \approx 13.7\ \mu\mathrm{m},$$

as given by equation (1.19). It was therefore concluded therefore concluded that the threshold effect in the count rate is due to quantisation of vertical motion within

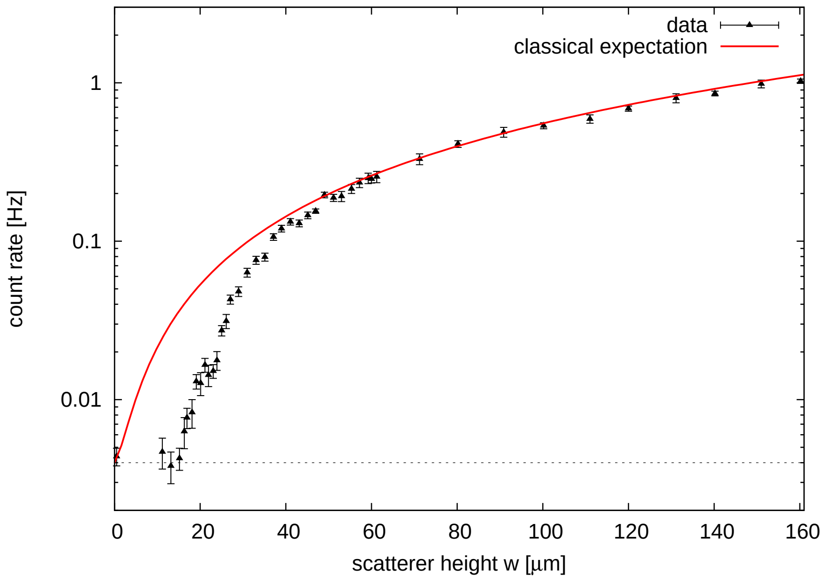

Figure 2.3: The integral flux measurement of 1999. The solid red line represents the flux expected from classical mechanics. (V. Nesvizhevsky, H. Abele *et al.*)

the waveguide. In a simplified view of things one may argue that at slit widths smaller than z_1^{WKB}, no quantum state 'fits' beneath the scatterer and that as, a consequence, no neutron can pass the waveguide.

This measurement is generally considered as the first observation of gravitationally bound quantum states worldwide. Details about data taking and analysis can be found e.g. in [Rueß00] or in [Wes01].

2.4 Position Sensitive Measurements

Although the integral flux measurements have been a tremendous success, they were always thought of as an interim solution. The final goal of the experiment has always been the *direct* observation of quantisation of vertical motion through the use of position resolving detectors. The idea is to measure the height above the second mirror for each neutron arriving at its back end. If this can be achieved at sufficiently high spatial resolution, the measured height distribution should correspond to the absolute square of the probability amplitude in position space for one neutron as derived in chapter 1.

2.4.1 The CR39 Nuclear Track Detector

Over the last years such detectors has been developed and refined, much of this work having been done by A. Gagarsky, S. Nahrwold *et al.*. S. Nahrwold devotes a major part of her diploma thesis [Nahr05] to the position sensitive detector and the data extraction process and presents some further detail we shall omit for the sake of clarity.

Nuclear track detectors are devices commonly used in nuclear physics as well as in medical dosimetry. Their operating principle is very simple: The detector consists of a homogeneous, transparent material, mostly a glass or, as in our case, a solid polymer. A high energetic charged particle impacting into the material disrupts any chemical bonds on its path through the polymer. It thereby leaves a *track* in the form of submicroscopic defects in the resin. Subsequently the detector is immersed into an etching solution such as $\mathrm{NaOH_{(aq)}}$. Along the nuclear traces, the polymer is corroded and dissolved at a faster rate than at the bulk of the material. Thus the etching corresponds to a development process, which enlarges the molecular damages left by the passage of charged particles up to a size detectable through standard optical microscopy.

The detector material we use is known under the brand name of CR39. Developed in the 1940's by the Columbia Southern Chemical Company, it is today manufactured under license worldwide, mainly to be used as optical lenses for sunglasses. Our detectors are supplied by Intercast Europe S.p.A. (Italy) and come in the shape of 1.5 mm thick blades of dimensions $1.5 \cdot 12\ \mathrm{cm}^2$, i.e. they perfectly suit the length of the mirror edge. In order to detect neutrons using the CR39 detector, just as in the case of the proportional counter tube, we have to first convert them into charged particles. This is achieved by coating the CR39 surface with a thin convertor layer. Of thickness around 200 nm, this layer can consist of either $^{235}\mathrm{UF}_4$ or $^{10}\mathrm{B}$, both of which are applied by evaporation and subsequent condensation at the polymer surface. Through capture reactions similar to that of $^3\mathrm{He}$, neutrons are converted into charged particles which then leave traces in the detector, as described above.

$$
\begin{aligned}
{}^{10}\mathrm{B} + \mathrm{n} &\longrightarrow \left\{ \begin{array}{ll} \alpha + {}^{7}\mathrm{Li} + \gamma & (93\%) \\ \alpha + {}^{7}\mathrm{Li} & (7\%) \end{array} \right. & & (+2.8\ \mathrm{MeV}) \\
{}^{235}\mathrm{U} + \mathrm{n} &\longrightarrow \quad \mathrm{X} + \mathrm{Y} + a\ \mathrm{n} & & (+Q)
\end{aligned}
$$

The latter is the very same fission reaction that takes place within a uranium-fueled nuclear reactor. The atomic weights of the *fission products* X and Y are statistically distributed around 95 and 135. The average number of produced neutrons a is 2.4. In contrast to the boron capture reaction, the energy release Q lies well above 100 MeV, most of which is carried by the heavy fission products which therefore

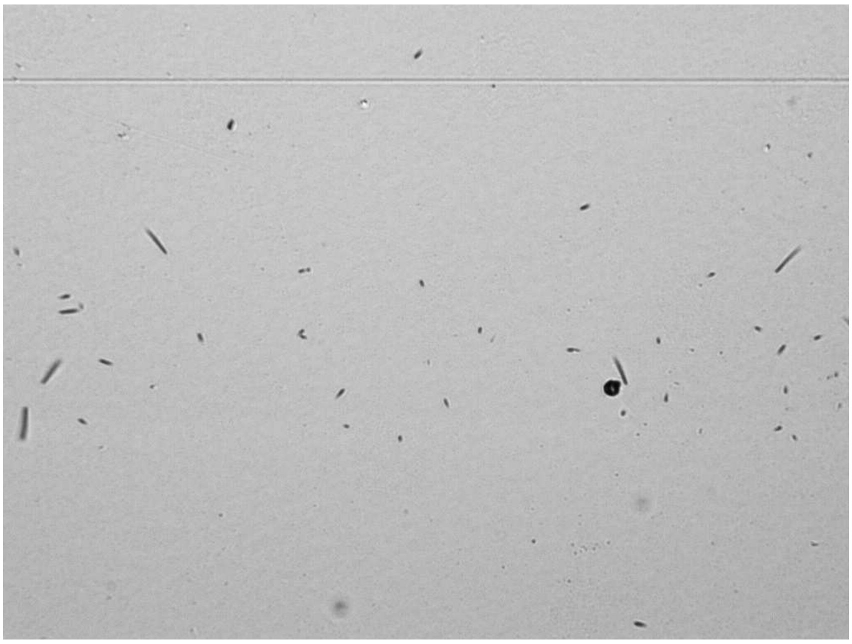

Figure 2.4: Photograph of a uranium-coated detector after irradiation and etching. The black 'darts' are traces left by fission fragments, unlike the dark spot to the right of the picture which results from a natural defect in the polymer. The horizontal line at the top is a scratch on the detector surface. The dimensions of the picture are approximately $300 \cdot 200\ \mu\mathrm{m}^2$.

essentially fly back-to-back. As stated above, the neutrons emerging from the decay carry energies around 1 MeV each, as a consequence the probability of a secondary capture reaction within the thin uranium fluoride coating is negligible. This ensures that the capture reaction will normally leave only a single, long nuclear trace in the detector.

Subsequent to irradiation with UCN, the detectors are developed for approximately one hour in a bath of sodium hydroxide of molarity 1, at a constant temperature of 45°C. This etching process enlarges the submicroscopic nuclear traces to small 'tunnels' of diameters around 1 μm and of depths of 10 μm or more. They are then easily visible under an optical microscope. Figure 2.4 shows the typical appearance of an irradiated detector surface after development.

detector no.	w (approx.)	exposure time	length read out	total counts
6	25 μm	60(1) h	73 mm	1883
7	50 μm	80(1) h	102 mm	13975

Table 2.1: Comparison of neutron exposures for the two detectors

2.4.2 The Measurements

The measurements described in this text were performed in 2005 using $^{235}UF_4$ coated detectors. Mounted into a brass holder designed to this end, the detector is placed directly against the edge of the second bottom mirror (see figure 2.2). Unlike for flux measurements, the height of the scatterer is now fixed at a chosen value while neutrons travel the waveguide and impact onto the conversion layer of the detector. Unfortunately the piezo leveling system which normally allows to adjust the scatterer height with an accuracy of better than 1 μm was unavailable during this experimental run. Therefore the width of the waveguide had to be set up using mechanical spacers placed between bottom mirror and scatterer and is not really a measured quantity.

Two measurements have been made: One detector ('detector 6') was irradiated with a waveguide width w of approximately 25 μm. For the second measurement ('detector 7') we aimed at a width of $w = 40$ μm, however analysis of the data shows that a true value of around 50 μm is more likely. Anyway, not having been determined independently with high enough accuracy, the scatterer height will have to be considered as a free parameter in any analysis of the data.

As can be seen in figure 2.3, the neutron flux transmitted by the waveguide at these scatterer heights can be expected to be of orders 0.01 s^{-1} and 0.1 s^{-1} for the 25-μm and 50-μm measurements respectively. In order to collect high enough statistics, the detectors therefore have to be exposed to the neutron beam for quite a while. Table 2.1 shows the exposure times for the two measurements. During measurement, our installation had to share the UCN beam with up to two other experiments on a turn-by-turn basis. Additionally mechanical perturbations caused by heavy machinery operating inside the reactor building often made it impossible to measure during normal working hours. Accumulating the 60 respectively 80 hours of net irradiation reported in table 2.1 thereby effectively required around a week's time for each of the two measurements.

2.4.3 The Data Extraction Process

Once irradiated, the convertor coating was removed from the detectors and the CR39 etched in $NaOH_{(aq)}$ as described above. Then the position of each track found on the

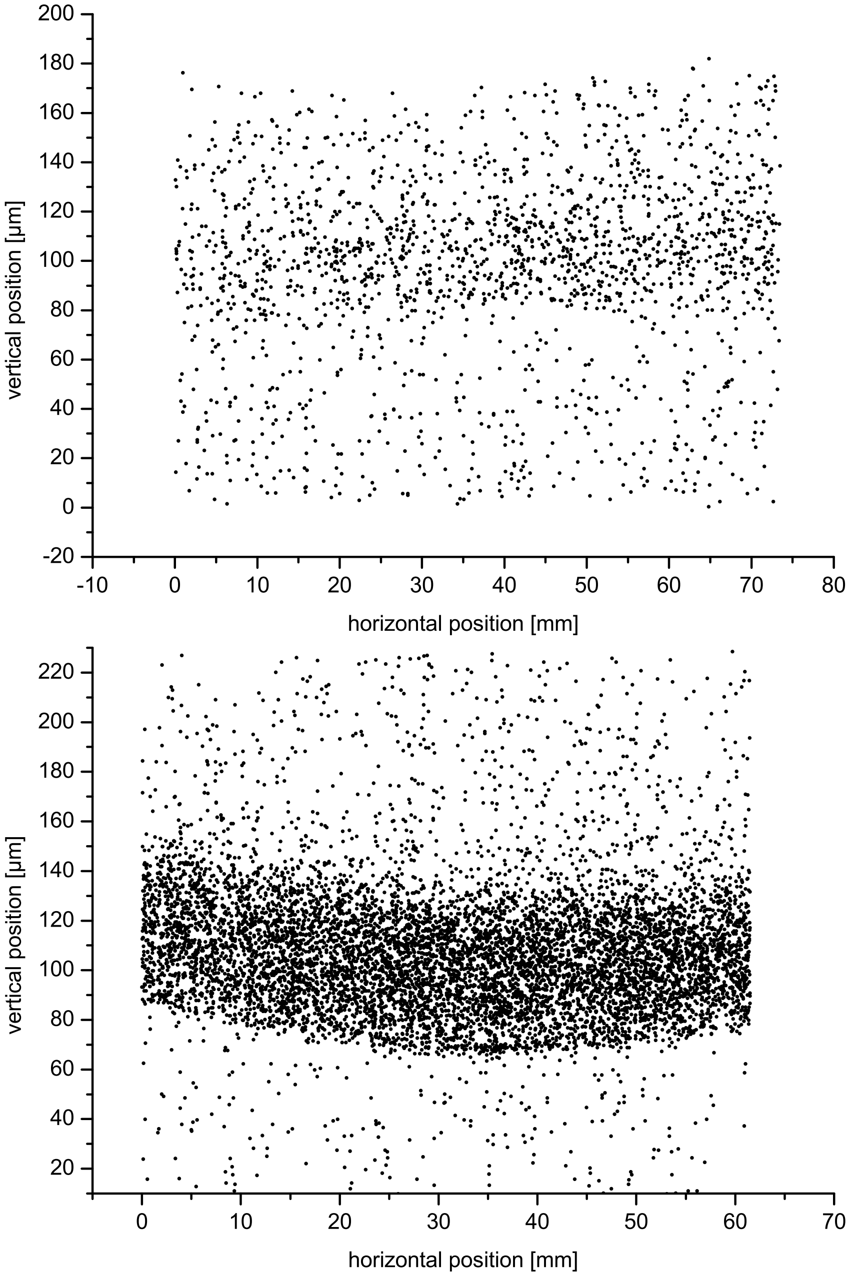

Figure 2.5: Raw data from the position sensitive detectors. Top: 25-μm measurement, bottom: 50-μm measurement. The effect of detector deformation is clearly visible.

detector needed to be recorded. This task is performed with the aid of a standard optical microscope equipped with a CCD camera. The area of the detector which was actually hit by neutrons emerging from the waveguide is clearly indicated by thousands of almost perfectly aligned fission fragment traces. The vertical extension of this line is approximately equal to the width of the waveguide and fits well inside the cameras field of view of $300 \cdot 200\ \mu\text{m}^2$ (see figure 2.4). Horizontally on the other hand, the traces are spread over the entire length of the detector. Using an automatic translation stage holding the detector we therefore had to take a series of over 300 pictures along the 10 cm of sensitive detector area for each of the two measurements.

There have been multiple attempts to write a computer program which would recognise the nuclear tracks on these photographs and thereby extract the position information from the detectors in an automated way. Up to now however, none of these programs works in a reliable manner. Too diverse are the shapes of the traces, too numerous the defects in the CR39 arising from other causes. This part of the readout process is therefore entirely manpowered. One by one, the pictures were visualised on a computer screen and the coordinates of each track recorded. In principle the accuracy with which the coordinates can be determined is limited by the resolution of the microscope alone and could be better than 1 μm. However, the idea that the resolution of the vertical neutron distribution measurement would be that good is illusory. The reasons for this are manifold:

1. As stated above, the etching process not only enlarges the nuclear tracks, but also removes material from the bulk of the detector. The entrance point of a track into the detector after development does therefore not exactly correspond to that of the original fission fragment.
2. The detector actually does not detect neutrons but fission fragments emerging from the above conversion reaction. This reaction takes place within the UF_4 coating, i.e. up to 200 nm *above* the CR39 surface. As a result, fragments impacting at a narrow angle hit the detector relatively far (up to half a μm) from the location of the actual capture reaction.
3. There is no guarantee that the translation axis of the microscope stage is parallel to that defined by the mirror edge during irradiation. We therefore expect the data to manifest an *inclination* relative to the true horizon.
4. During etching the detector heats up and bends under the effects of thermal stress. Although care is taken to render this process as gentle as possible, part of this deformation is irreversible.

In contrast to the first, the latter two resolution lowering effects can be measured and corrected as will be described in the next subsection. Figure 2.5 shows the raw

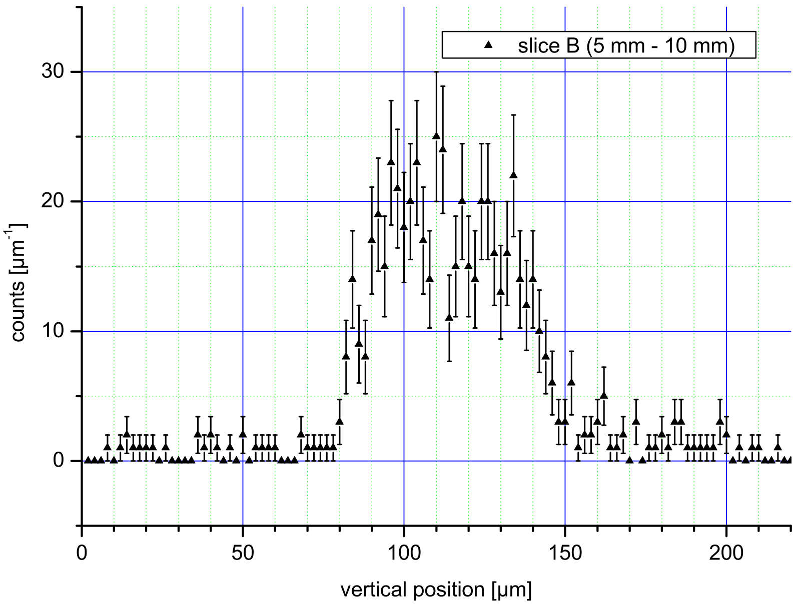

Figure 2.6: Track height distribution for a given slice of 5 mm for the 50-μm measurement. In this example, the onset of the distribution, i.e. the height corresponding to 20%maximal track density, corresponds to approxiamtely 80 μm.

data recorded from the two detectors. Especially for the 50-μm measurement, which collected a lot more statistics, curvature and inclination of the data are clearly visible. The deformation causes approximately 7 μm of vertical deviation per centimeter detector length.

2.4.4 Data Corrections

For the 50-μm measurement statistics is so high that inclination and curvature corrections could be determined from the dataset itself. Therefore we considered vertical slices of lengths 5 mm of the detector and had a look at height distribution histograms in each of them as shown in figure 2.6. For each of these small subsets of data the *onset* of the distribution, i.e. the height corresponding to 20% maximal track density, was determined. The data points obtained in this way were interpolated into a polynomial which was then used to correct curvature and inclination of the original dataset. A limitation of the microscope translation stage prevented taking datasets longer than 73 mm from the detector in one run. In order to extract all 10 cm of data, a similar procedure was used in order to pile-up three partial datasets.

As one easily sees in figure 2.5, statistics is much lower for the 25-μm measurement. The curvature of the detector therefore had to be determined in an independent way. After the main measurement, the detector was shifted downwards relative to the mirror edge by 100 μm and the waveguide opened to a very large width w. This results in a sharp 'edge' formed by tens of thousands of nuclear traces on the detector. Since the mirror is known to be flat to very high standards [Roc05], any curvature of this edge, which can be determined in a manner similar than presented for the 50-μm measurement, must be due to detector deformation. The detector having been shifted in between, the inclination of the edge obviously does not correspond to that of the actual measurement. The data having been corrected for curvature, the inclination was therefore corrected by minimising the width of the height distribution of nuclear traces. Due to the lack of statistics it was impossible to sum up different parts of this detector, hence only a part of 73 mm out of 10 cm has been taken into account.

Figure 2.7 shows the data from the two detectors after inclination and curvature corrections have been applied.

The information we are finally interested in is the height distribution of neutrons impinging onto the detectors. Figure 2.8 presents the height histograms obtained from the final (corrected) datasets using bin sizes of 1 μm. The errorbars indicated in the plots are Poisson-statistical standard deviations. It is noteworthy that, at the onset of the distribution, the track density rises to a maximum value within a few bins only (see especially the 50-μm measurement). This already indicates that the achieved detector resolution is as good as very few micrometers.

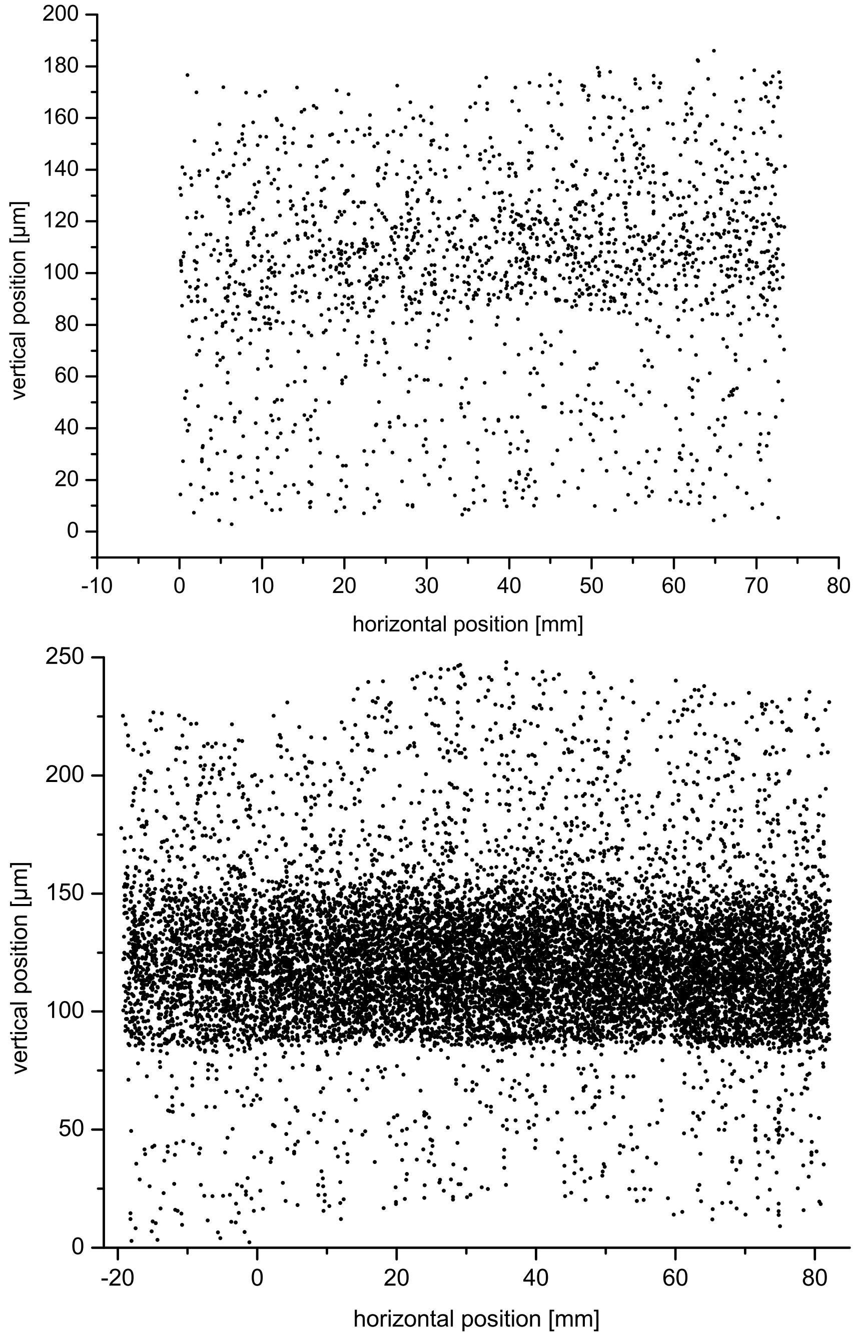

Figure 2.7: Data from the 25-μm (top) and 50-μm (bottom) measurements respectively, corrections for detector curvature and inclination having been applied

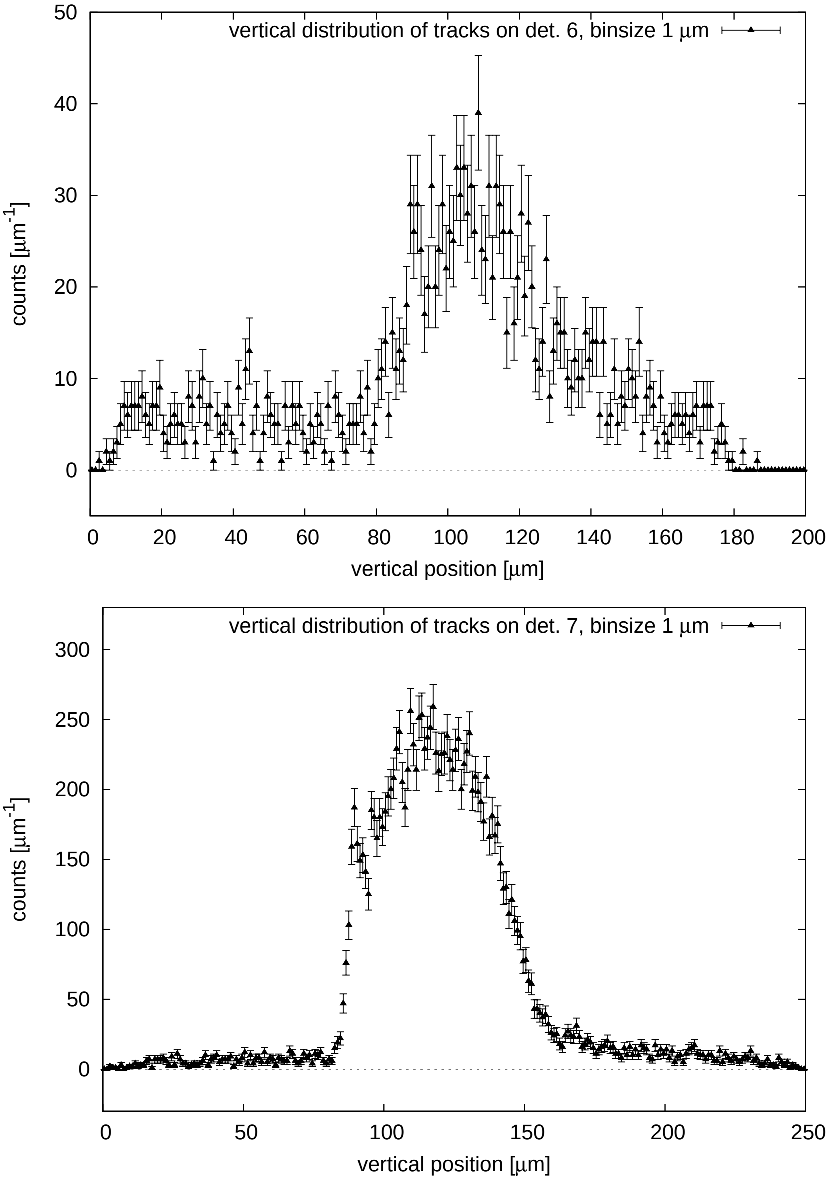

Figure 2.8: Neutron height distributions above the second mirror for the 25-μm ('detector 6') and 50-μm ('detector 7') measurements respectively.

Chapter 3

Quantum Mechanical Analysis

In the preceding chapter we have presented how the probability density distribution of neutrons bouncing above the mirror surface has been measured. In the following we will develop a model describing this experiment within the framework of quantum mechanics. In section 1.2 we already discussed the problem of a particle bouncing freely above a reflecting surface. Our physical system is however more complicated than this theoretical toy model. In order to understand all features found in the measurements we will therefore have to generalise and extend our previously obtained results.

3.1 Observables of the Measurement

The first question to ask is: "What has been measured?" Although it may seem obvious, the answer to this question is of so crucial an importance to any quantum system that it cannot be stressed enough. As we know from the fundamental principles of quantum theory [Schwa98], the measurement of a quantity related to a system can only yield *eigenvalues* a_n of the *operator* A corresponding to this measuring process. a_n having been measured, the system is projected into the *eigenstate* ψ_n. These three objects are related by the eigenvalue equation of the operator:

$$A\psi_n = a_n\psi_n$$

Furthermore, if a system's wavefunction can be written as a superposition of eigenfunctions of A

$$\Psi = \sum_n c_n\psi_n \ , \tag{3.1}$$

it follows from the axioms of quantum mechanics that the absolute square of an expansion coefficient $|c_n|^2$ corresponds to the *probability* of measuring the associated eigenvalue a_n.

In a language more suited to experimental physics, we say that the measurement of an *observable* A may yield one out a set of values $\{a_n\}$. The measurement modifies the system in such a way that from all subsequent measurements of this type we shall obtain the very same result than from the first one.

3.1.1 Quantum Mechanical Position Measurement

Let us have a look at how this formalism applies to our experiment. The solutions of a Schrödinger equation like (1.10) are eigenstates of the Hamilton operator H. The latter corresponds to the observable quantity *energy*. Thus the ψ_n we found in equation (1.14) are eigenstates corresponding to energy eigenvalues:

$$H\psi_n = E_n\psi_n$$

However, the position resolving detector does *not* measure energy. Our observable is the height z of a neutron above the mirror. There is therefore no reason to expect the neutron's wavefunction to be projected into one of the eigenvectors ψ_n of the Hamiltonian.

Let $\Psi(z)$ be the overall wavefunction of the neutron subject to the gravitational potential and the boundaries imposed by the waveguide. Let ζ be the eigenvalues of the position operator z. Our measurement inherently solves the eigenvalue equation

$$z\psi_\zeta(z) = \zeta\psi_\zeta(z)$$

with the obvious solutions

$$\psi_\zeta(z) = \delta(z-\zeta) \ .$$

The ψ_ζ form a continuous spectrum of eigenfunctions of the position operator z, fulfilling the orthogonality and completeness relations

$$\int \mathrm{d}z \ \psi^*_\zeta(z)\psi_{\zeta'}(z) = \delta(\zeta-\zeta') \ ,$$

$$\int \mathrm{d}\zeta \ \psi^*_\zeta(z)\psi_\zeta(z') = \delta(z-z') \ ,$$

which permits us to expand the wavefunction $\Psi(z)$ in eigenfunctions of z:

$$\Psi(z) = \int \mathrm{d}\zeta \ \Psi(\zeta)\psi_\zeta(z) \tag{3.2}$$

As we can see, equation (3.2) is the precise counterpart of (3.1) in the case of a continuous eigenvalue spectrum. Thus (3.2) states that the overall wavefunction $\Psi(z)$ is a superposition of position eigenstates $\psi_\zeta(z)$ with expansion coefficients given by $\Psi(\zeta)$. As a consequence, $|\Psi(\zeta)|^2$ is the *probability density* of measuring a position $z = \zeta$. The wavefunction Ψ being identical to it's position spectrum reflects the fact that $\Psi(z)$ is derived by solving the Schrödinger equation in position space, as indeed we have done in section 1.2.

Thus the height measurement z does not imply further restrictions on Ψ as long as the latter is expressed in position space. The only requirement is that Ψ must be a solution of the Schrödinger equation, i.e. that it can be expanded into a series of eigenfunctions ψ_n:

$$\Psi = \sum_n c_n \psi_n \tag{3.3}$$

The height distribution of neutrons above the mirror surface is then directly given by $|\Psi|^2$.

3.1.2 Time Dependence

Up to now, all of our calculations have been time-independent. However, this procedure is in principle not correct. If, through an equation like (3.3), we admit that the wavefunction Ψ may be not a pure but a superposition of eigenstates, we have to account for potentially arising *interference* terms. That is, we have to consider states ψ_n that are solutions of the *time-dependent* Schrödinger equation

$$H\psi_n(z,t) = \mathrm{i}\hbar \frac{\partial}{\partial t}\psi_n(z,t) \ .$$

Luckily, the $\psi_n(z,t)$ can be derived from the time-independent eigenstates $\psi_n(z)$ using the time development operator:

$$\psi_n(z,t) = \psi_n(z) \exp\left(-\frac{\mathrm{i}}{\hbar}E_n t\right)$$

As the position operator z does not act on the time-dependent parts of the functions, all of our above considerations continue to hold. However, we can now rewrite equation (3.3) emphasising the time dependence of Ψ:

$$\Psi(z,t) = \sum_n c_n \psi_n(z,t) = \sum_n c_n \psi_n(z) \exp\left(-\frac{\mathrm{i}}{\hbar}E_n t\right) \tag{3.4}$$

Expansion of this time-dependent $\Psi(z,t)$ analogous to equation (3.2) simply leads to coefficients which are also time-dependent and given by $\Psi(\zeta,t)$:

$$\Psi(z,t) = \int \mathrm{d}\zeta \ \Psi(\zeta,t)\psi_\zeta(z)$$

This means that, in principle, the height density distribution $|\Psi(z,t)|^2$ is time-dependent too:

$$\begin{aligned}
|\Psi(z,t)|^2 &= \Psi(z,t)\cdot\Psi^*(z,t) \\
&= \left(\sum_n c_n\psi_n(z,t)\right)\cdot\left(\sum_m c_m\psi_m(z,t)\right)^* \\
&\overset{(3.4)}{=} \sum_{n,m} c_n c_m^* \psi_n\psi_m^* \;\exp\left[-\frac{\mathrm{i}}{\hbar}(E_n-E_m)t\right] \\
&= \sum_n |c_n|^2|\psi_n|^2 + \sum_{n\neq m} c_n c_m^*\;\psi_n\psi_m^*\;\exp\left[-\frac{\mathrm{i}}{\hbar}(E_n-E_m)t\right] \\
&= \sum_n |c_n|^2|\psi_n|^2 + \frac{1}{2}\sum_{n\neq m} 2\;c_n c_m^*\;\psi_n\psi_m^*\;\cos\left[\frac{t}{\hbar}(E_n-E_m)\right]
\end{aligned}$$

The last identity holds since both the eigenstates $\psi_n(z)$ and the expansion coefficients c_n are real numbers, i.e. because of

$$c_n c_m^*\;\psi_n\psi_m^* = c_m c_n^*\;\psi_m\psi_n^*\;.$$

We shall now show that in our experiment the time dependent part of $|\Psi(z,t)|^2$ has an expectation value equal to zero, i.e. that

$$\left\langle \sum_{n\neq m} c_n c_m^*\;\psi_n\psi_m^*\;\cos\left[\frac{t}{\hbar}(E_n-E_m)\right]\right\rangle = 0\;. \tag{3.5}$$

The reason for this is that the horizontal velocity spectrum of neutrons entering the waveguide is quite broad. This velocity distribution has been measured in 2002 by V. Nesvizhevsky *et al.* using the system's collimating system. This measurement has been published in [Nesv05] and yielded an approximately Gaussian velocity spectrum

$$P_{vx}(v_x) = \frac{1}{\sqrt{2\pi}\sigma_{vx}}\exp\left(-\frac{1}{2}\frac{(v_x-\overline{v_x})^2}{\sigma_{vx}^2}\right) \tag{3.6}$$

of mean

$$\overline{v_x} = 6.3\ \mathrm{ms}^{-1} \tag{3.7}$$

and of width

$$\sigma_{vx} = 1.1\ \mathrm{ms}^{-1}\;.$$

Over a distance of 10 cm, i.e. over the length of one bottom mirror, this velocity distribution results in a time-of-flight spectrum of width

$$\Delta t_{\mathrm{ToF}} \approx 10^{-2}\ \mathrm{s}\;,$$

as can be seen from figure 3.1. On the other hand, the period τ of the cosine in

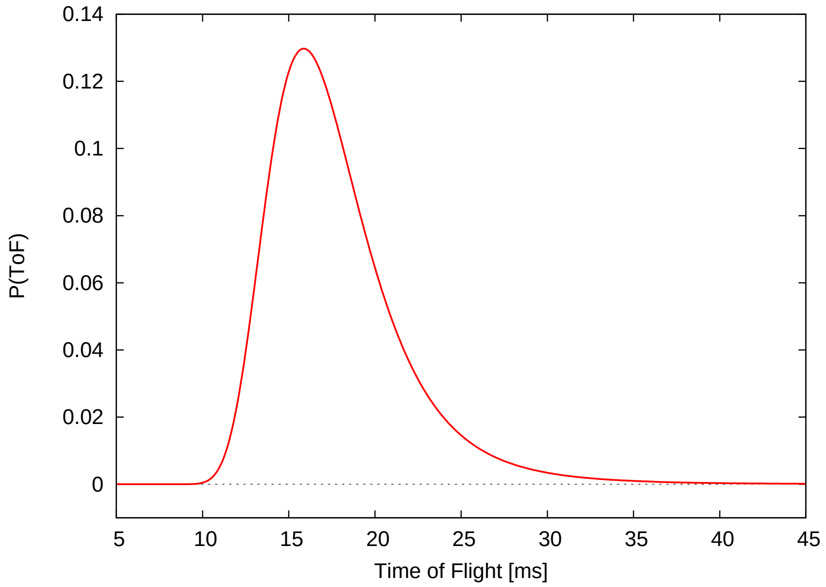

Figure 3.1: The time-of-flight spectrum derived from (3.6) for neutrons traveling a horizontal distance of 10 cm, corresponding to the length of one bottom mirror

equation (3.5) is

$$\tau = \frac{2\pi\hbar}{E_n - E_m} = \frac{2\pi\hbar}{\Delta E} \ .$$

Recalling from table 1.1 that energy differences in gravitationally bound states can hardly be smaller than about 1 peV, we can give an upper estimation on τ:

$$\tau = \frac{2\pi\hbar}{\Delta E} \leq \frac{2\pi \cdot 6.6 \cdot 10^{-16} \text{ eV} \cdot \text{s}}{10^{-12} \text{ eV}} \approx 4 \cdot 10^{-3} \text{ s}$$

Thus we have $\Delta t_{\text{ToF}} \geq 2\tau$, and we expect that the measurement of $|\Psi|^2$ will average over at least two periods of oscillation of the time-dependent cosine terms. As a consequence, the latter will cancel each other out. Equation (3.5) is thereby verified and $|\Psi(z,t)|^2$ reduces to

$$\boxed{|\Psi|^2 \equiv |\Psi(z)|^2 = \sum_n p_n \cdot |\psi_n(z)|^2} \ , \tag{3.8}$$

where we have introduced the *state populations*

$$p_n = |c_n|^2 \ .$$

Equation (3.8) states that the height distribution $|\Psi(z)|^2$ we expect to measure using a position resolving detector is a *purely incoherent* superposition of the time-independent eigenstates ψ_n of the Hamilton operator. The populations p_n reflect the contributions of the individual eigenstates to the integral probability density.

3.2 The Quantum Mechanical Waveguide

The results from the preceding section leave us with quite clear an idea about what is the observed quantity in our experiment. Additionally, we have gained a basic understanding of how the measured height distributions, as depicted in figure 2.8, have to be interpreted. Neutron heights above the mirror should be distributed following $|\Psi(z)|^2$. The latter is, according to equation (3.8), determined by

1. the *eigenstates* ψ_n of the time-independent Schrödinger equation and
2. the *populations* p_n of these states.

Thus, in order to come to a quantum mechanical understanding of the measurements, it is imperative to gain some insight into both of these factors.

3.2.1 Eigenstates

In section 1.2 we already solved the Schrödinger equation for a particle in a linear gravitational potential. This treatment led us to the eigenstates of the 'quantum bouncer' given by equation (1.20)

$$\psi_n^{\mathrm{WKB}}(z) = \begin{cases} N^{-1}\mathrm{Ai}\left(\frac{z}{R} - \epsilon_n^{\mathrm{WKB}}\right) & : \quad z \geq 0 \\ 0 & : \quad z < 0 \end{cases} ,$$

with the reduced energy eigenvalues $\epsilon_n^{\mathrm{WKB}}$ given by equation (1.18). These solutions were derived using the boundary conditions (1.15) and (1.16) which read

$$\begin{aligned} \psi(z) &= 0 \qquad (z \leq 0) \\ \psi(z) &\to 0 \qquad (z \to +\infty) \ . \end{aligned}$$

Let us have a look at the schematic drawing of the waveguide in figure 3.2. As depicted, we can discern three regions in the setup, defined by the positions of the mirror step and the edges of the mirrors and scatterer. It is clear that there is only one region that has boundary conditions similar to (1.15) and (1.16), namely the 7-cm long part of the second mirror (region III) which is not covered by the scatterer.

Eigenstates in Region III

Let us agree that the height $z = 0$ corresponds to the surface of the first mirror, the surface of the second mirror is then located at $z = -s$ where

$$s = (13.5 \pm 0.5)\ \mu\mathrm{m}$$

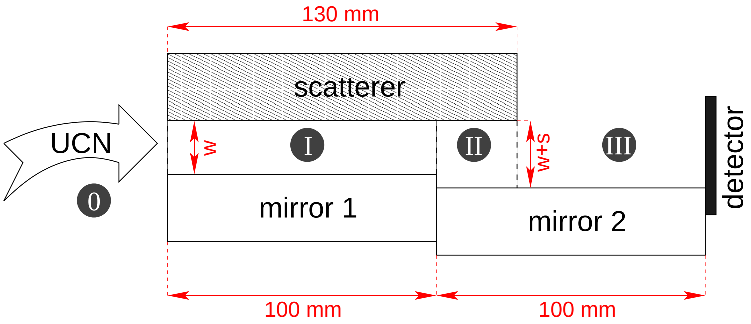

Figure 3.2: Schematic drawing of the waveguide. We distinguish three regions (I, II and III) with different boundary conditions. 0 denotes the free space between the collimator blades and the entrance slit. The waveguide width w and the size of the step s are expanded in order to be visible in the picture.

is the height of the mirror step, measured using a mechanical comparator (see chapter 2). As a consequence, the boundary conditions in region III are

$$\begin{aligned} \psi^{\mathrm{III}}(z) &= 0 \qquad (z \leq -s) \\ \psi^{\mathrm{III}}(z) &\to 0 \qquad (z \to +\infty)\ . \end{aligned}$$

The corresponding eigenstates are therefore of the form given by equation (1.20), with the origin of heights shifted towards $-s$:

$$\boxed{\psi_n^{\mathrm{III}}(z) = \begin{cases} N^{-1}\mathrm{Ai}\left(\frac{z+s}{R} - \epsilon_n^{\mathrm{WKB}}\right) & : \quad z \geq -s \\ 0 & : \quad z < -s \end{cases}} \tag{3.9}$$

The reduced energy eigenvalues $\epsilon_n^{\mathrm{WKB}}$ continue to be given by equation (1.18) and the factor N^{-1} ensures normalisation of the states.

Equation (3.9) is a very noteworthy result. As by 'region III' we understand the space directly in front of the detector, the ψ_n^{III} actually *are* the eigenstates ψ_n entering into equation (3.8) describing the height distribution. However, for reasons to become clear in the following subsection, we need to solve the Schrödinger equation in regions I and II of the waveguide as well, where, due to the presence of the scatterer, the boundary condition (1.16) is no longer correct.

Eigenstates in Regions I and II

The scatterer is manufactured out of the same optical glass than the bottom mirrors and therefore corresponds to a Fermi potential step of equal height

$$U \approx 100\ \mathrm{neV}\ .$$

With its surface placed at a height $z = w$, the wavefunction will thus have to vanish at a height close to w. However, in contrast to the mirrors, the scatterer is characterised by a large surface roughness (see chapter 2). The corresponding potential step will therefore not be infinitely sharp, but washed out over a length of about

$$2\rho = 2\rho_{\text{scatterer}} \approx 1.5\ \mu\text{m}\ ,$$

where $\rho_{\text{scatterer}}$ is the RMS roughness amplitude as reported in chapter 2. Because of this relatively smooth rise of the Fermi potential, the wavefunction does not have to vanish exactly at $z = w$ but may tunnel into the scatterer potential. A detailed analysis of this behavior can be found in [Wes01]. The penetration depth of the wavefunction into the scatterer will obviously be related to the roughness amplitude ρ, thus we *assume* that it is equal to 2ρ. The waveguide width w having been set up using spacers placed between mirror and scatterer, we further assume that w is the location of the lowest tips of the surface roughness. Consequently, the wavefunction has to vanish at a height h with

$$h = w + 2\rho\ . \tag{3.10}$$

Let us now have a look at region I of the waveguide. Independent of boundary conditions, we found that solutions of the Schrödinger equation (1.10) are given by equation (1.14):

$$\psi(\zeta) = c_A\ \text{Ai}(\zeta - \epsilon) + c_B\ \text{Bi}(\zeta - \epsilon)$$

We recall that ζ and ϵ are the reduced position and energy, related to the physical quantities z and E by the scaling factor R defined in equation (1.11):

$$\zeta := \frac{z}{R}\ ; \quad \epsilon := \frac{E}{mgR} \tag{3.11}$$

The boundary conditions in region I read

$$\psi^{\text{I}}(\zeta) = 0 \qquad (\zeta \leq 0) \tag{3.12}$$

$$\psi^{\text{I}}(\zeta) = 0 \qquad (\zeta \geq h/R) \tag{3.13}$$

and correspond to the set of linear equations

$$\begin{cases} c_A\ \text{Ai}(-\epsilon) + c_B\ \text{Bi}(-\epsilon) &= 0 \\ c_A\ \text{Ai}(h/R - \epsilon) + c_B\ \text{Bi}(h/R - \epsilon) &= 0 \end{cases} .$$

Thus equation (3.12) states

$$\frac{c_A}{c_B} = -\frac{\text{Bi}(-\epsilon)}{\text{Ai}(-\epsilon)} \tag{3.14}$$

which, together with (3.13), leads to an equation relating ϵ and the scatterer height[1] h:

$$\text{Ai}(h/R - \epsilon)\ \text{Bi}(-\epsilon) - \text{Ai}(-\epsilon)\ \text{Bi}(h/R - \epsilon) = 0 \tag{3.15}$$

---

[1] In order to account for the slight but important difference between h and w given by equation (3.10), we shall in the following name the first ‘scatterer height’ and the latter ‘waveguide width’.

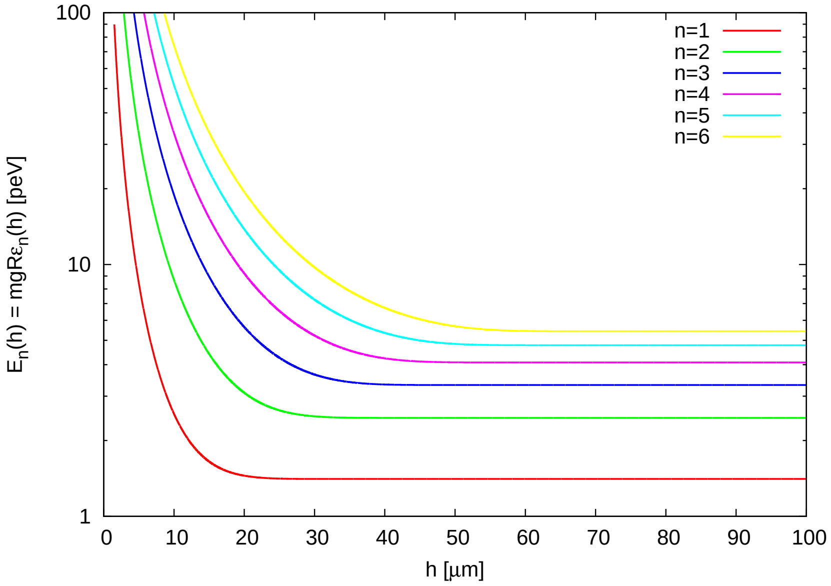

Figure 3.3: Energy eigenvalues obtained from equation (3.15) for the first six bound states in region I as a function of the scatterer height h

Equation (3.15) can be solved numerically. For each scatterer height h it yields a set of solutions $\{\epsilon_n(h)\}$, where n is again a quantum number. Figure 3.3 depicts the first six energy eigenvalues as a function of scatterer height h.

We clearly see that, for large scatterer heights, the eigenvalues converge towards their counterparts reported in table 1.1. This is expected, as in the limit $h \to \infty$ the boundary condition (3.13) becomes equivalent to (1.16). For $h \to 0$ on the other hand, the gravitational potential becomes more and more insignificant and the neutron essentially feels a square well potential. Thus we expect the eigenvalues to behave like $E_n \sim n^2$, which is also visible in figure 3.3.

Combining the general solution (1.14) of the Schrödinger equation with (3.14) and with the $\epsilon_n(h)$ obtained from (3.15), we obtain the eigenstates of the system in region I:

$$\boxed{\psi_n^{\mathrm{I}}(z) = \begin{cases} N^{-1}\left\{\mathrm{Ai}\left[\frac{z}{R} - \epsilon_n(h)\right] - \frac{\mathrm{Ai}[-\epsilon_n(h)]}{\mathrm{Bi}[-\epsilon_n(h)]}\,\mathrm{Bi}\left[\frac{z}{R} - \epsilon_n(h)\right]\right\} & : \quad 0 < z < h \\ 0 & : \quad \text{else} \end{cases}} \tag{3.16}$$

Again, N^{-1} is a normalisation factor.

The states in region II differ from those in region I only by the position of the

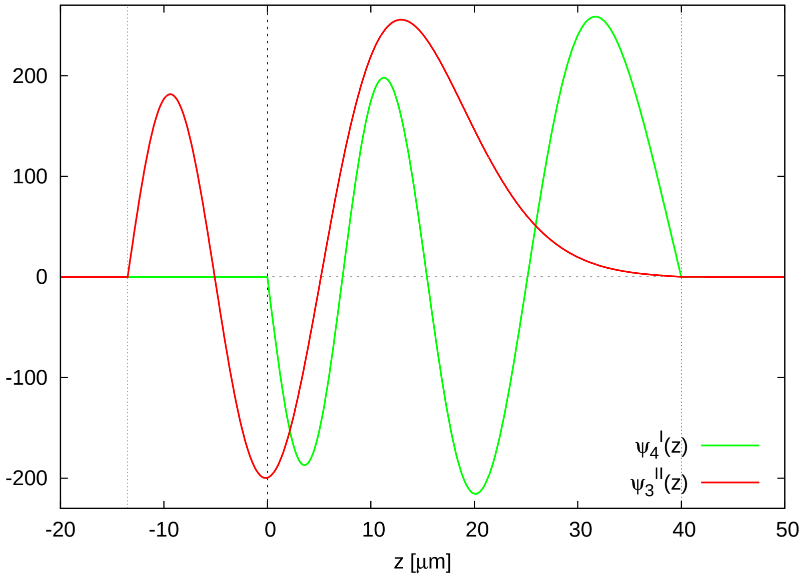

Figure 3.4: The fourth eigenstate in region I and the third eigenstate in region II of the waveguide. It is clearly visible, how ψ_4^{I} is 'squeezed' by the scatterer placed at $h = 40$ μm while ψ_3^{II} is largely unaffected by it.

lower boundary condition. Instead of (3.12) and (3.13) we now have

$$\begin{aligned} \psi^{\mathrm{II}}(\zeta) &= 0 \qquad (\zeta \leq -s/R) \\ \psi^{\mathrm{II}}(\zeta) &= 0 \qquad (\zeta \geq h/R) \ . \end{aligned}$$

Analogous to equation (3.16), we thus find the eigenstates in region II of the waveguide:

$$\boxed{\psi_n^{\mathrm{II}}(z) = \left\{ \begin{array}{ccc} \begin{array}{c} N^{-1} \left\{ \mathrm{Ai}\left[\frac{z+s}{R} - \epsilon_n(h+s)\right] \right. \\ \left. - \frac{\mathrm{Ai}[-\epsilon_n(h+s)]}{\mathrm{Bi}[-\epsilon_n(h+s)]} \, \mathrm{Bi}\left[\frac{z+s}{R} - \epsilon_n(h+s)\right] \right\} \end{array} & : & -s < z < h \\ 0 & : & \mathrm{else} \end{array} \right.} \tag{3.17}$$

In contrast to their counterparts in region III, the eigenstates (3.16) and (3.17) can only be computed numerically as we have no simple approximation formula for their eigenvalues. Nevertheless we have now solved the Schrödinger equation in all three of the regions of the waveguide. As an example, figure 3.4 shows an eigenstate of region I and II respectively.

3.2.2 Transitions within the Waveguide

Having found eigenstates for the waveguide we now turn towards the problem of determining the *populations* p_n of these states. As a neutron travels the waveguide it is represented by a different wavefunction Ψ in each of the three regions indicated in figure 3.2. At two points, namely at the transitions from region I to II and from region II to III, the neutron is subject to changes in the binding potential and the wavefunction has to adapt itself to a new set of boundary conditions. These perturbations of the wavefunction take place *suddenly* in the sense that the transit from one region to another is fast compared to the time it takes the wavefunction to 'rearrange' itself.

Supposed we know the shape of the wavefunction Ψ^{I} at the moment it leaves region I. What will be the shape of the function Ψ^{II} in region II after the perturbation caused by the mirror step?

Each of the wavefunctions can be expanded in a series of eigenstates, which, in general, may be time dependent:

$$|\Psi^{\mathrm{I}}, t\rangle = \sum_m c_m |m, t\rangle \tag{3.18}$$

$$|\Psi^{\mathrm{II}}, t\rangle = \sum_n d_n |n, t\rangle$$

In order to simplify mathematical expressions we have switched to *bra-ket* notation and introduced the shorthands

$$|m, t\rangle \equiv |\psi_m^{\mathrm{I}}, t\rangle$$

$$|n, t\rangle \equiv |\psi_n^{\mathrm{II}}, t\rangle \ .$$

We are interested in the question: What is the probability $P_{\Psi^{\mathrm{I}}\to n}$ that, upon transition, an eigenstate $|n, t\rangle$ of region II will be populated? For a transition between bound states, quantum mechanics [Schwa98] tells that this probability is given by

$$P_{\Psi^{\mathrm{I}}\to n} = \left|\langle n, t|\Psi^{\mathrm{I}}\rangle\right|^2 \ . \tag{3.19}$$

As this formula is correct only in the case of quick changes in the binding potential, it is commonly known as the *'sudden approximation'*. Recall from (3.8) that by a 'population' p_n^{II} we understand the probability $|d_n|^2$ of finding the neutron in an eigenstate $|n, t\rangle$ of region II. As a consequence, $P_{\Psi^{\mathrm{I}}\to n}$ and p_n^{II} are identical:

$$P_{\Psi^{\mathrm{I}}\to n} \equiv |d_n|^2 = p_n^{\mathrm{II}} \tag{3.20}$$

Combining equations (3.18), (3.19) and (3.20), we write

$$\begin{aligned}
P_{\Psi^{\mathrm{I}}\to n} &= p_n^{\mathrm{II}} = \left|\langle n,t|\Psi^{\mathrm{I}}\rangle\right|^2 \\
&= \left|\langle n,t|\sum_m c_m|m,t\rangle\right|^2 = \left|\sum_m c_m\langle n,t|m,t\rangle\right|^2 \\
&= \left|\sum_m c_m\langle n|m\rangle \exp[\mathrm{i}t(E_n-E_m)/\hbar]\right|^2 \\
&= \sum_{m,m'} c_m c_{m'}^*\langle n|m\rangle\langle m'|n\rangle \exp[\mathrm{i}t(E_{m'}-E_m)/\hbar] \\
&= \sum_m |c_m|^2\left|\langle n|m\rangle\right|^2 + \underbrace{\sum_{m\neq m'} c_m c_{m'}^*\langle n|m\rangle\langle m'|n\rangle \cos[(E_{m'}-E_m)t/\hbar]}_{\to 0}\ .
\end{aligned}$$

For the reasons already discussed in subsection 3.1.2 the time-dependent off-diagonal terms cancel each other out. Thus we find a direct connection between the state populations in region I (p_m^{I}) and those in region II (p_n^{II}):

$$\boxed{p_n^{\mathrm{II}} = \sum_m p_m^{\mathrm{I}}\left|\langle\psi_n^{\mathrm{II}}|\psi_m^{\mathrm{I}}\rangle\right|^2} \tag{3.21}$$

The quantities $\langle\psi_n^{\mathrm{II}}|\psi_m^{\mathrm{I}}\rangle$ are called the *transition matrix elements* and are given by

$$\langle\psi_n^{\mathrm{II}}|\psi_m^{\mathrm{I}}\rangle = \int \mathrm{d}z\ \psi_m^{\mathrm{I}}(z)\psi_n^{\mathrm{II}*}(z)\ .$$

In perfect analogy, we can link the populations in region III (p_n^{III}) to those in region II (p_m^{II}) and find

$$\boxed{p_n^{\mathrm{III}} = \sum_m p_m^{\mathrm{II}}\left|\langle\psi_n^{\mathrm{III}}|\psi_m^{\mathrm{II}}\rangle\right|^2}\ . \tag{3.22}$$

As an example, table 3.1 shows how an initially pure groundstate evolves due to the perturbations caused by the transitions from one region of the waveguide to another. The height of the scatterer is taken to be $h = 20\ \mu$m. As indicated already in chapter 2, the size of the step $s = 13.5\ \mu$m is chosen in such a way that the passage from region I to II causes the groundstate to be heavily suppressed. In contrast to this, the transition at the edge of the scatterer hardly affects the lowest states at all. It mainly causes a repopulation in the high quantum numbers which, as will be shown in the following sections, are suppressed by other factors anyway.

region	p_1	p_2	p_3	p_4	p_5
I	1	0	0	0	0
II	0.06	0.62	0.31	< 0.01	< 0.01
III	0.06	0.61	0.27	< 0.01	< 0.01

Table 3.1: The evolution of the populations p_n of an initially pure groundstate due to transitions between different regions of the waveguide. The scatterer height h used in the calculations is 20 μm.

3.2.3 The Scatterer

As a last step, we have to find a quantum mechanical model describing the effect of the scatterer. As indicated in chapter 2, the scatterer is supposed to ‘remove’ neutrons from the system that carry to high an energy in their vertical motion component. Such neutrons would occupy high quantum states and, according to Bohr’s Principle, the system’s dynamics would be dominated by classical mechanics. Obviously, tracking down quantum effects would be very hard in such a scenario.

This having been said, it should be emphasised that the scatterer *does* a very good job at removing high states. In an experiment designed to verify its good working condition, we placed the scatterer at the *bottom* of the waveguide and the mirror above it, i.e. we reversed the geometry of the setup. In this situation, the scatterer should prevent *all* neutrons from passing the waveguide, as all will collide with its surface, regardless of their quantum numbers being high or low. The results of this measurement are shown in figure 3.5. We see that even at slit widths of half a millimeter, the count rate measured using the ^{3}He detector does not rise to above 0.3 Hz. See for comparison figure 2.3: Here the same count rate is reached at a slit width of approximately 70 μm.

There have been multiple attempts to understand the action of the scatterer from first principles. In the early years of the experiment the scatterer surface was coated with a gadolinium alloy which was supposed to remove neutrons hitting it by nuclear capture reactions. Thus the scatterer used to be named ‘absorber’ at that time. However, a detailed analysis then revealed [Nesv05] that the dominating factor determining the scatterer’s efficiency is its surface roughness.

The presently adopted view of the removal mechanism is therefore based on the idea of diffuse neutron scattering: Non specular reflection of neutrons at the scatterer surface leads to randomly distributed vertical velocities of the order of several meters per second. Such neutrons then undergo a large number of collisions with the scatterer and mirrors. At each of these impacts they have a finite probability of penetrating the Fermi potential barrier, such that their overall probability of

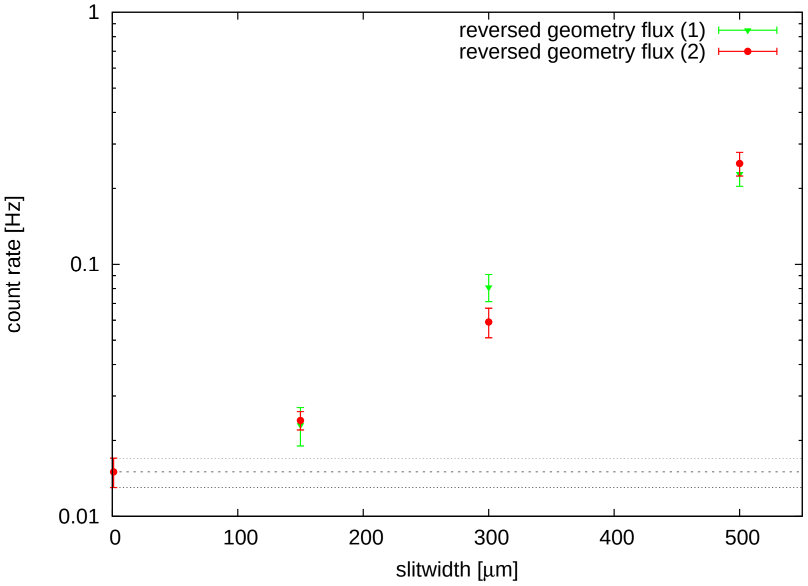

Figure 3.5: Flux measurement with reversed geometry, i.e. with the scatterer placed at the bottom of the waveguide.

'surviving' the passage through the waveguide is low. Even *if* they happen not to be absorbed, they are scattered all over the vacuum chamber and, in the worst case, cause a diffuse, perfectly homogeneous background that does not disturb the actual measurement at all.

In order to account for this scattering process in a proper way, A. Westphal [Wes06] treated it as s-wave scattering of the neutron's wavefunction at the tips of the surface roughness. A more recent model [Vor05], developed by A. Voronin, models the scatterer surface as a potential barrier oscillating in space as the neutron flies past it, thereby causing a periodic perturbation of the wavefunction. At this moment however, both of these models still seem to be incapable of predicting the scatterer efficiency *ab initio* and have to include free parameters in order to fit experimental data.

In this situation we may as well adopt a very simple parametrisation of the scatterer action [Abe05]. In equation (3.10) we have assumed that an eigenstate in region I or II does not vanish at the height w, corresponding to the slit width, but may tunnel into the scatterer roughness by up to a depth of 2ρ. It is quite sensible to assume that the probability Γ for a neutron to be removed through scattering is proportional to the probability to find it at some location within the surface roughness. We hence write

$$\Gamma_n(w) \sim \int_w^{w+2\rho} \mathrm{d}z \, |\psi_n(z)|^2 \tag{3.23}$$

for the probability per unit time for the eigenstate ψ_n to be destroyed by interaction with the scatterer. w is the width of the waveguide and ρ the RMS roughness amplitude taken to be (c.f. chapter 2)

$$\rho \approx 0.75 \ \mu\mathrm{m} \ .$$

For states with low quantum numbers n the value of the integral in (3.23) is close to zero due to the exponential decrease of the wavefunction at large z. Higher states, on the other hand, can be linearly approximated around $z = w$ and their probabilities Γ_n are correspondingly large. Figure 3.4 provides a good illustration of this property.

From equation (3.23) we immediately derive that the population p_n of a given eigenstate diminishes with time according to an exponential decay law:

$$p_n(t) = p_n(0) \exp(-\Gamma_n t) \tag{3.24}$$

Let L be the length of the waveguide region in which the state is exposed to the scatterer and v_x the horizontal velocity of the neutron. Then

$$t = \frac{L}{v_x}$$

and, using (3.23), we can rewrite (3.24) as

$$\boxed{p_n(L) = p_n(0) \exp\left(-\beta \ L \int_w^{w+2\rho} \mathrm{d}z \, |\psi_n(z)|^2\right)} \ , \tag{3.25}$$

where we have introduced the *scatterer efficiency per unit length* β, which is a free fit parameter in our model.

3.3 A First Attempt to Fit the Experimental Data

We have now reached a good level of understanding of the quantum mechanics that govern the neutron's behavior as it travels the waveguide. Thus we may undertake a first attempt to fit the theoretical model developed above to our experimental data shown in figure 2.8.

3.3.1 The Fit Function

The vertical distribution of neutrons above the second mirror is in principle governed by equation (3.8):

$$|\Psi(z)|^2 = \sum_n p_n \; |\psi_n(z)|^2$$

We want to derive a fit function $F(z)$ from this expression. As we have seen, the eigenstates $\psi_n(z)$ are those in region III. Additionally our fit function has to include free parameters for background, offset and norm of the distribution, i.e.

$$F(z) = a \left(\sum_{n=1}^{n_{\max}} p_n^{\mathrm{III}} \left|\psi_n^{\mathrm{III}}(z - z_{\mathrm{off}})\right|^2 \right) + b_{\mathrm{det}} + b_{\mathrm{scatt}} \Theta(z - z_{\mathrm{off}}) \; . \tag{3.26}$$

Therein a is the normalisation factor and z_{off} the offset between the origin of heights in figure 2.8 and the surface of the *second* mirror. b_{det} is the detector background *below* the measured distribution, i.e. the density of traces in that part of the detector that was covered by the mirror during measurement. This background is a measured quantity, it is equal to the average track density in the left parts of the histograms in figure 2.8. b_{scatt} is an additional background in the region *above* the height of the second mirror surface. This part of the detector was not covered during measurement and may have been irradiated by scattered neutrons present in the vacuum chamber. The step function in (3.26) ensures that b_{scatt} is taken into account in the corresponding data region only.

The state populations p_n^{III} entering into equation (3.26) are computed according to the quantum mechanical modeling of the waveguide we have developed throughout the preceding sections. In principle the series in equation (3.8) is infinite. However, we know that high quantum states are heavily suppressed by the scatterer, we may therefore introduce a sufficiently large $n_{\max}$ and ignore eigenstates with higher n. As they travel the waveguide, the states' populations will evolve as follows:

1. We *assume* that at the entrance of the waveguide of width w, all eigenstates are equally populated:
$$p_n^{\mathrm{I}}(0) \sim 1 \quad \text{for all } n \tag{3.27}$$
2. While traveling region I, the states are suppressed according to equation (3.25): $p_n^{\mathrm{I}}(0) \rightarrow p_n^{\mathrm{I}}(L^{\mathrm{I}} = 7 \text{ cm})$. At this point the scatterer efficiency β enters as a free fit parameter.
3. At the mirror step transitions cause a repopulation suppressing the ground state in region II: $p_n^{\mathrm{I}}(L^{\mathrm{I}}) \rightarrow p_n^{\mathrm{II}}(0)$
4. In the 3-cm long region II the eigenstates decay further following (3.25) due to the presence of the scatterer: $p_n^{\mathrm{II}}(0) \rightarrow p_n^{\mathrm{II}}(L^{\mathrm{II}} = 3 \text{ cm})$

5. At the end of region II, the 'surviving' states emerge into region III: $p_n^{\mathrm{II}}(L^{\mathrm{II}}) \to p_n^{\mathrm{III}}$.

These p_n^{III} are finally the populations entering into equation (3.26). They obviously depend on the scatterer's efficiency β as well as on the waveguide width w.

As stated in chapter 2, the resolution of the CR39 detectors is finite and determined by number of factors. In order to account for this, the fit function $F(z)$ has to be convoluted with a Gaussian distribution of width σ equal to the detector resolution:

$$\boxed{\tilde{F}(z) = \frac{1}{\sqrt{2\pi}\sigma} \int \mathrm{d}z' \; F(z') \cdot \exp\left[-\frac{1}{2} \left(\frac{z'-z}{\sigma} \right)^2 \right]} \tag{3.28}$$

This expression is used to describe the experimental data. In total our model thereby contains six free parameters. They are

1. the width of the waveguide w,
2. the efficiency of the scatterer per unit length β,
3. the detector resolution σ,
4. the offset of the measured distribution z_{off},
5. the norm of the distribution a
6. and the scattered neutron background b_{scatt}.

3.3.2 Fit Results

As a first test, we fit equation (3.28) to the data from the 50-μm measurement ('detector 7' in figure 2.8) which features by far higher statistics. The number of eigenstates taken into account is

$$n_{\max} = 50 \ .$$

The detector background b_{det} is determined from the data points in the height interval from 26 μm to 81 μm:

$$b_{\mathrm{det}.7} = (6.9 \pm 0.3) \ \mu\mathrm{m}^{-1}$$

The fit routine takes into account data points in the region 70 μm to 200 μm]. Figure 3.6 depicts the best fit of the model to the data. Corresponding values for the free parameters are summarised in table 3.2. Needless to say, the fit is bad. Although the

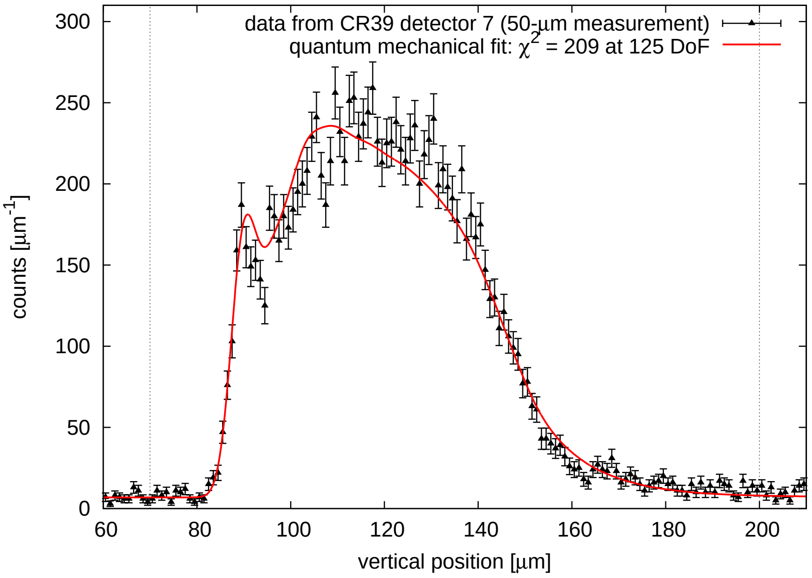

Figure 3.6: The best fit of the data to a quantum mechanical model assuming equally populated states at the entrance of the waveguide. Obviously the model cannot describe the data quantitatively.

parameter	best fit value
waveguide width w	$(52 \pm 2)\ \mu\mathrm{m}$
scatterer efficiency β	$(2900^{+800}_{-500})\ \mathrm{m}^{-1}$
detector resolution σ	$(2.3 \pm 0.4)\ \mu\mathrm{m}$
scattered background b_{scatt}	$(0 \pm 3)\ \mu\mathrm{m}^{-1}$
norm a	$(0.0122 \pm 0.0003)\ \mu\mathrm{m}^{-1}$
offset z_{off}	$(86.4 \pm 0.4)\ \mu\mathrm{m}$

Table 3.2: Best fit values for the free parameters in a quantum mechanical model of the experiment assuming equally populated states at the entrance of the waveguide.

calculation seems to qualitatively reproduce the shape of the measured distribution, the χ^2-test yields

$$\chi^2 = 209 \text{ at } 125 \text{ degrees of freedom,}$$

corresponding to a reduced χ^2 of

$$\tilde{\chi}^2 = 1.67 \ ,$$

or a probability

$$P(\chi^2) < 10^{-5} \ .$$

In plain words, our theory is statistically refuted even on a 1%-basis, which is the lowest generally accepted rejection threshold.

The reason for this disappointing result is obvious from figure 3.6: At low z, i.e. in the left part of the measured height distribution, the fit function lies systematically *above* the data points. From this fact we can directly conclude that, for the lowest eigenstates, our theory predicts populations p_n that are higher than in reality.

3.3.3 Groundstate Suppression Theories

At many occurrences [Nesv05] [Rueß00] [Wes01], data taken in the experiment could be modeled only under the assumption that the population of the *groundstate* was suppressed by an unknown mechanism. Ideas normally put forward in order to qualitatively explain such a suppression include microscopic pollutions of the bottom mirrors that would disturb the wavefunctions as they pass the mirror. Another ansatz [Nesv05b] involves depopulation of the lowest states due to acoustic vibrations of the mirrors against which the setup can hardly be protected.

Indeed, if, leaving the rest of fit procedure untouched, we introduce a further decay law analogous to (3.23), affecting the groundstate alone

$$p_1(t) = p_1(0) \exp(-\gamma t) \ , \tag{3.29}$$

the quality of the fit improves significantly, as shown in figure 3.7.

Of course such a practice of ‘fitting away’ an unwanted effect is highly unsatisfactory. Furthermore, it is not clear why a scattering or absorption mechanism taking place at the *bottom* mirror should sharply discriminate between quantum numbers, or why, upon collision with a vibrating mirror surface, a neutron should gain energy but never loose some. Within the framework of this text we shall therefore try to understand the suppression of the lowest states using the completely different ansatz to be developed in the following section.

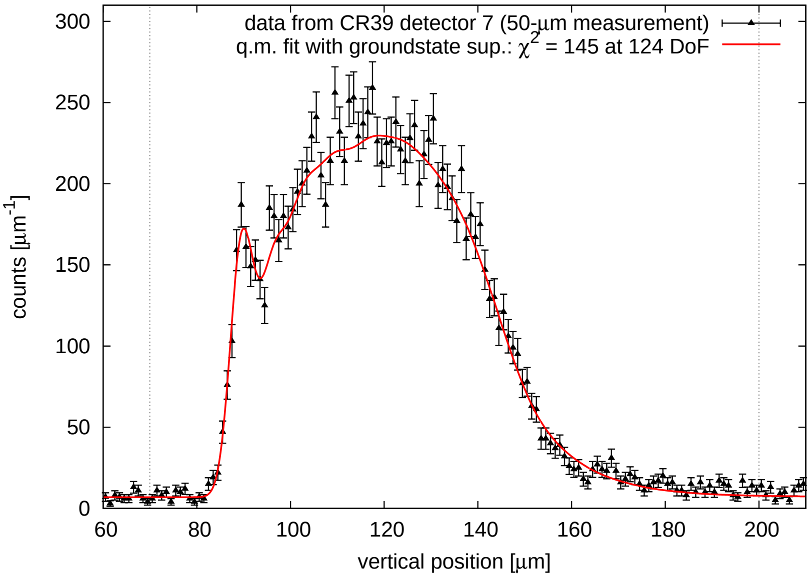

Figure 3.7: The best fit of the data to a model involving uniformly distributed starting populations, but suppressing the ground state according to equation (3.29).

3.4 The Starting Population

We have made significant efforts in order to come to an understanding of the quantum mechanics taking place *within* the waveguide. There is however one process that we have quite strikingly neglected: the transition of the wavefunction from free space ('region 0' in figure 3.2) *into* the waveguide. In the preceding section we have simply *assumed* through equation (3.27) that, at the beginning of region I, all eigenstates were equally populated. Obviously, if this assumption turns out to be unjustified, this could explain why the data fits to equation (3.28) so badly.

3.4.1 Transition into the Waveguide

Let us have a closer look at the wavefunctions' transition from free space into the waveguide, i.e. the transition from region 0 to region I.

From figure 2.2 we see that in region 0 the neutron is in fact also subject to boundary conditions of the 'quantum bouncer'-type. The only difference is that the lower boundary is defined by the floor of the vacuum chamber, a few *centimeters* below the zero height defined by the surface of the first mirror. Hence, instead of the boundary conditions (1.15) and (1.16), we have

$$\begin{aligned}\psi_n^0(z \to \infty) &= 0 \\ \psi_n^0(z \approx -4 \text{ cm}) &= 0 \ . \end{aligned} \tag{3.30}$$

Still, the wavefunction Ψ^0 has to be a linear combination of quantum bouncer eigenstates ψ_n^{WKB} as given by equation (1.20). Equation (3.30) only means that neutrons capable of entering the waveguide at $z = 0$ must have *very high* quantum numbers in region 0. Recall from equation (1.19) that, in the WKB approximation, an eigenstate ψ_n^{WKB} corresponds to a classical turning point height

$$z_n = R\,\epsilon_n^{\text{WKB}} \ ,$$

where ϵ_n^{WKB} is the WKB approximation of the reduced energy eigenvalues given by (1.18). Now we need

$$z_n \approx 4 \text{ cm}$$

which, according to equations (1.18) and (1.19) requires

$$n \approx 120000 \ .$$

At quantum numbers so high, the energy difference between neighboring states becomes very small: From equation (1.18) we obtain

$$\Delta E_{120000} = E_{120001}^{\text{WKB}} - E_{120000}^{\text{WKB}} \approx 0.023 \text{ peV} \ .$$

For comparison, we take a look at the energy uncertainty of the bound states in region I of the waveguide. As can be seen from figure 3.1, a neutron typically needs the time

$$t = 16 \text{ ms}$$

to travel the first mirror. From Heisenberg's Principle we therefore derive

$$\mathrm{d}E_n \geq \frac{2\pi\hbar}{t} \approx 0.26 \text{ peV}$$

for the energy uncertainty $\mathrm{d}E_n$ of a bound state in region I. Thus the differences of energy levels in free space are much smaller than the energy uncertainty of states bound in the waveguide:

$$\mathrm{d}E_n \gg \Delta E_{120000}$$

Hence the energy spectrum in region 0 may as well be regarded as *continuous*.

This means that the transition from region 0 to region I is fundamentally different from transitions *within* the waveguide. Transitions from or into a continuum of states take place on arbitrarily short time scales [Schwa98]. The transition from region 0 to I can therefore not be calculated in the 'sudden approximation' we have used in subsection 3.2.2 but has to be treated within the framework of time-dependent perturbation theory.

Let $|n\rangle$ be an eigenstate of region I and $|m\rangle$ one of region 0. It follows from time-dependent perturbation theory [Schwa98] that the probability $P_{m\to n}$ for a transition $|m\rangle \to |n\rangle$ to take place within the time interval dt is

$$P_{m\to n} = \frac{2\pi}{\hbar}\delta(E_n - E_m)\,|\langle n|V|m\rangle|^2\,\mathrm{d}t\ . \tag{3.31}$$

Therein E_n and E_m are the states' energies in the waveguide and in free space respectively, and $\langle n|V|m\rangle$ is the transition matrix element containing the perturbation potential V. The delta-distribution in (3.31) is to be understood in the sense that the energies of initial state $|m\rangle$ and final state $|n\rangle$ have to coincide within the uncertainty dE_n of the bound state.

We now *assume* that the matrix elements in (3.31) are approximately equal for all initial states. Then the probability $P_{\Psi^0\to n}$ for a given eigenstate $|n\rangle$ of region I to be populated by *whatever* free state $|m\rangle$ is the sum over all possible transitions (3.31):

$$P_{\Psi^0\to n} = \sum_m P_{m\to n} = \int \mathrm{d}E_m\ \rho(E_m)P_{m\to n} = \rho(E_n)\frac{2\pi}{\hbar}|\langle n|V|m\rangle|^2\mathrm{d}t \tag{3.32}$$

$\rho(E_n)$ is the *density of states* in the continuum in the energy interval dE_n around E_n. Equation (3.32) was derived in 1928 by Pauli and is generally known as 'Fermi's Golden Rule'.

As in subsection 3.2.2, the overall transition probability into an eigenstate is equal to the population of that state. As stated above, we neglect a possible dependence of the matrix elements on the quantum numbers and write

$$p_n^{\mathrm{I}}(0) \sim \rho(E_n)\ . \tag{3.33}$$

In plain words, the starting population $p_n^{\mathrm{I}}(0)$ of an eigenstate ψ_n^{I} depends only on the density of continuum states at that state's energy E_n.

We could now try to derive the density of states in region 0 from a quantum mechanical calculation. However, this would be quite laborious a process, as, unlike for states in the waveguide, time-dependence of the wavefunction does matter for neutrons in region 0. Hence we follow another path. As we have seen, quantum numbers in region 0 have to be very high. Thus we hope that, according to Bohr's Principle, the system will behave classically and that it will be sufficient to derive the *energy spectrum* at the entrance of the waveguide from classical statistical mechanics. In order to do so, we first need to have a careful look at the collimating system already briefly described in chapter 2.

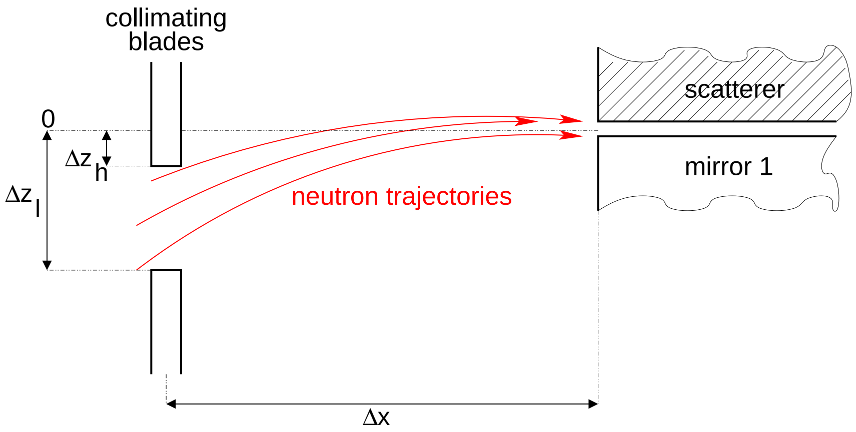

Figure 3.8: Schematic view of the collimating system. The geometry of the setup is completely determined by the three parameters Δz_h, Δz_l and Δx.

3.4.2 The Collimating System

Look at figure 2.2 for an illustration of the collimator. In section 2.2 we have stated without proof that the waveguide selects neutrons from the UCN gas delivered by the turbine in such a way that *vertical velocities* v_z at the entrance of the waveguide are of the order of a few cm/s only. In the following we are going to demonstrate and quantify this statement.

As can be seen in figure 3.8, the geometry of of the collimator can be completely described by three parameters: Again, let $z = 0$ be the height of the first mirror. We call Δx the *horizontal* distance between the collimating blades (outside the vacuum chamber) and the entrance of the waveguide. We further denote by Δz_h and Δz_l the *vertical* height differences between the waveguide entrance at $z = 0$ and the edges of the upper and lower collimating blade respectively. These lengths have not been measured, however they can be taken to have orders of magnitude of one millimeter for the vertical distances and ten centimeters for Δx.

From subsection 3.1.2 we know that the spectrum of horizontal velocities v_x is a Gaussian of mean $\overline{v_x} = 6.3$ m/s and of width $\sigma_{vx} = 1.1$ m/s. Furthermore, due to the small height of the entrance window, it is safe to assume that the beam intensity is constant inside the collimator. This means that the horizontal velocities v_x and the starting heights z_0 of neutrons at the blades are distributed according to

$$P_{vx}(v_x) = \frac{1}{\sqrt{2\pi}\sigma_{vx}} \exp\left(-\frac{1}{2}\frac{(v_x - \overline{v_x})^2}{\sigma_{vx}^2}\right) \tag{3.34}$$

$$P_{z0}(z_0) = \begin{cases} 1/(\Delta z_l - \Delta z_h) & : \quad -\Delta z_l \leq z_0 \leq -\Delta z_h \\ 0 & : \quad \text{else} \end{cases} \quad . \tag{3.35}$$

We are only interested in neutrons on trajectories leading into the waveguide, all others are lost to the system. Such trajectories must fulfill the conditions

$$\begin{aligned} v_x t &\overset{!}{=} \Delta x \\ -\frac{1}{2} g t^2 + v_{z0} t + z_0 &\overset{!}{=} 0 \ , \end{aligned}$$

where t is the time elapsed since the neutron's passage between the collimating blades at $x = 0$. Hence we obtain the following requirement on the starting velocity v_{z0}:

$$v_{z0} \overset{!}{=} \frac{1}{2} \frac{\Delta x}{v_x} g - z_0 \frac{v_x}{\Delta x}$$

The corresponding *vertical velocity* v_z at the entrance of the waveguide is then

$$\begin{aligned} v_z(v_x, z_0) &= -gt + v_{z0} \\ &= -\frac{1}{2} \frac{\Delta x}{v_x} g - z_0 \frac{v_x}{\Delta x} \quad . \end{aligned}$$

Since, from (3.34) and (3.35), we know the probability distributions of v_x and z_0, we can derive that of the vertical velocities v_z in the waveguide:

$$\tilde{P}_{vz}(v_z) = \iint \mathrm{d}z_0 \ \mathrm{d}v_x \ P_{vx}(v_x) P_{z0}(z_0) \ \delta \left(v_z + \frac{1}{2} \frac{\Delta x}{v_x} g + z_0 \frac{v_x}{\Delta x} \right)$$

Finally, after integration of the delta-distribution, we are left with

$$\tilde{P}_{vz}(v_z) = \int \mathrm{d}v_x \frac{\Delta x}{v_x} \ P_{vx}(v_x) P_{z0} \left(\frac{\Delta x}{v_x} v_z - \frac{1}{2} \left(\frac{\Delta x}{v_x} \right)^2 \right) \quad . \tag{3.36}$$

Equation (3.36) is the probability distribution of vertical velocities v_z at the entrance of the waveguide. Since the horizontal velocity distribution is known, it depends only on the geometric parameters indicated in figure 3.8. Figure 3.9 presents plots of the v_z-distribution (3.36) for various combinations of the parameters Δz_l, Δz_h and Δx. We observe two notable properties of the function:

1. Independent of the parameters, the v_z-distribution can always be well approximated by a normal distribution.
2. Both the width and the mean of this approximate Gaussian depend on the setup geometry. However this dependence is not very strong; the width of the v_z-spectrum is of the order of a few cm/s for *any* setup imaginable.

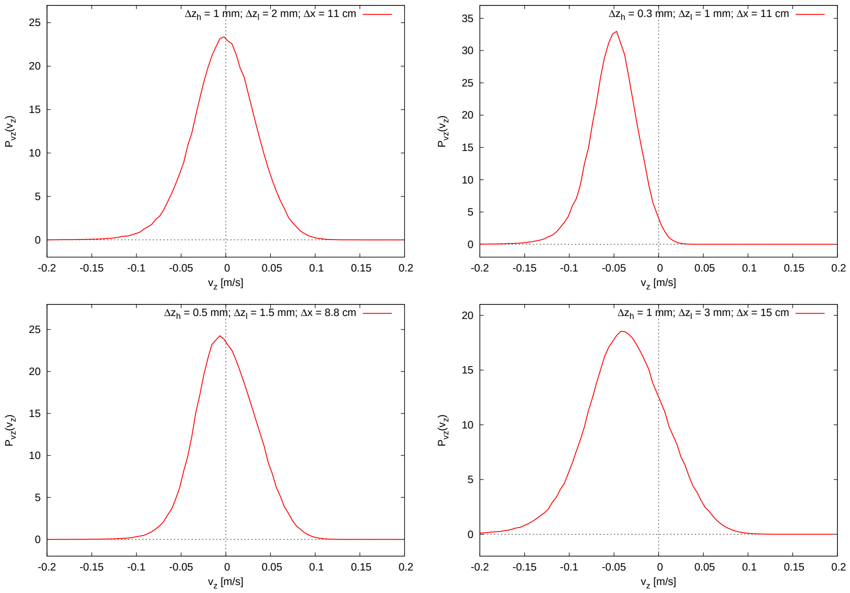

Figure 3.9: Plots of the v_z-distribution (3.36) for different combinations of the geometric parameters Δz_h, Δz_l and Δx.

As mentioned above, the parameters describing the setup geometry have unfortunately not been measured during the experiment. On the other hand we do not want to add as much as three additional free parameters to our waveguide model. We therefore *assume* that the v_z-distribution is centered at zero. Although this may seem a random assumption, it is not: While preparing the the installation for measurement, the correct collimator setting is found by observing the integral flux through the waveguide using the ^{3}He detector and maximising it. As the scatterer is known to primarily remove neutrons with high absolute values of v_z, this flux should be maximal precisely in the situation where the vertical velocity distribution is centered at zero.

The *width* of the v_z-spectrum, on the other hand, cannot be fixed by such a simple argumentation. It is therefore a new free parameter which we call σ_{vz}. Hence, we finally adopt the expression

$$\tilde{P}_{vz}(v_z) \approx P_{vz}(v_z) = \frac{1}{\sqrt{2\pi}\sigma_{vz}} \exp\left[-\frac{1}{2}\left(\frac{v_z}{\sigma_{vz}}\right)^2\right] \tag{3.37}$$

for the distribution of vertical velocities at the entrance of the waveguide and take note that reasonable values for σ_{vz} have to be of the order of a few cm/s.

3.4.3 The Energy Spectrum

Having understood the effect of the collimator, we are now able to deduce the classical distribution of energies at the entrance of the waveguide. Thereby we understand the distribution of the *total* energy carried by arriving neutrons in their vertical motion component

$$E = T + V \ .$$

We denote by T the kinetic and by V the potential energy of a neutron. Obviously, T is related to the vertical velocity spectrum we have just derived. Its probability density P_T is linked to P_{vz} by

$$P_T(T) = \int \mathrm{d}v_z \ P_{vz}(v_z) \ \delta\left(T - \frac{1}{2}mv_z^2\right) \ .$$

Integrating the delta-function yields

$$P_T(T) = \frac{1}{\sqrt{\pi m T}\sigma_{vz}} \exp\left(-\frac{T}{m\sigma_{vz}}\right) \ . \tag{3.38}$$

Correspondingly, the distribution of V is governed by that of the starting heights z of arriving neutrons above the mirror surface. Again, as the scatterer height h is very small compared to the dimensions of the collimating system, we may safely take these to be uniformly distributed:

$$P_z(z) = \left\{ \begin{array}{ccc} 1/h & : & 0 \leq z \leq h \\ 0 & : & \text{else} \end{array} \right. \tag{3.39}$$

From this we derive the probability density for the potential energies

$$P_V(V) = \int \mathrm{d}z \ P_z(z) \ \delta(V - mgz)$$

with the final result

$$P_V(V) = \left\{ \begin{array}{ccc} 1/mgh & : & 0 \leq V \leq mgh \\ 0 & : & \text{else} \end{array} \right. \ . \tag{3.40}$$

Kinetic and potential energy may now sum up to a given total energy E in arbitrary constellations. Thus the probability distribution of the latter is given by

$$\begin{aligned} P_E(E) &= \iint \mathrm{d}T\mathrm{d}V \ P_T(T)P_V(V) \ \delta(E - T - V) \\ &= \int \mathrm{d}V \ P_T(E - V)P_V(V) \end{aligned}$$

Some attention now has to be paid to the integration limits in the last expression. From equation (3.40) we see that V can never be greater than mgh. On the other hand, V may also not be greater than a given total energy E, thus we distinguish two cases:

1. Let $E \leq mgh$. In this situation we integrate over V from 0 to E. Inserting (3.38) and (3.40) yields

$$\begin{aligned} P_{E,1}(E) &= \int_0^E \mathrm{d}V \, \frac{1}{\sqrt{\pi m(E-V)}\sigma_{vz}} \exp\left(-\frac{E-V}{m\sigma_{vz}^2}\right) \frac{1}{mgh} \\ &= \operatorname{erf}\left(\sqrt{\frac{E}{m\sigma_{vz}^2}}\right) \frac{1}{mgh} \, . \end{aligned}$$

2. Let $E > mgh$. The integration now goes from 0 to mgh and we get

$$\begin{aligned} P_{E,2}(E) &= \int_0^{mgh} \mathrm{d}V \, \frac{1}{\sqrt{\pi m(E-V)}\sigma_{vz}} \exp\left(-\frac{E-V}{m\sigma_{vz}^2}\right) \frac{1}{mgh} \\ &= \left[\operatorname{erf}\left(\sqrt{\frac{E}{m\sigma_{vz}^2}}\right) - \operatorname{erf}\left(\sqrt{\frac{E-mgh}{m\sigma_{vz}^2}}\right)\right] \frac{1}{mgh} \, . \end{aligned}$$

Hence we obtain the following final expression for the probability distribution of total energies at the entrance of the waveguide:

$$\boxed{P_E(E) = \begin{cases} \frac{1}{mgh} \operatorname{erf}\left(\sqrt{\frac{E}{m\sigma_{vz}^2}}\right) & : \; E \leq mgh \\ \frac{1}{mgh}\left[\operatorname{erf}\left(\sqrt{\frac{E}{m\sigma_{vz}^2}}\right) - \operatorname{erf}\left(\sqrt{\frac{E-mgh}{m\sigma_{vz}^2}}\right)\right] & : \; E > mgh \end{cases}} \, . \qquad (3.41)$$

As we can see, $P_E(E)$ depends on two parameters: The scatterer height h and the width of the vertical velocity spectrum σ_{vz}. Figure 3.10 shows the energy distribution $P_E(E)$ for $h = 50$ μm and various values of σ_{vz}. Obviously, the spectrum is far from being uniform. $P_E(E)$ rises monotonously up to $E = mgh$ which corresponds to the potential energy at the height of the scatterer, then it decreases more or less rapidly depending on the value of σ_{vz}. The larger is σ_{vz}, the broader is the corresponding energy spectrum.

3.4.4 Starting Populations

Recall from (3.33) that, upon transition from free space into the waveguide, we expect the eigenstates ψ_n^{I} of region I to be populated according to the density of states in the continuum $\rho(E)$. In a semi-classical approximation we expect the latter to be *equivalent* to the classical total energy distribution we have just derived:

$$P_E(E) \sim \rho(E) \qquad (3.42)$$

Both the classical and the quantum mechanical distributions are essentially phase space factors which contain information about how frequently a given energy E

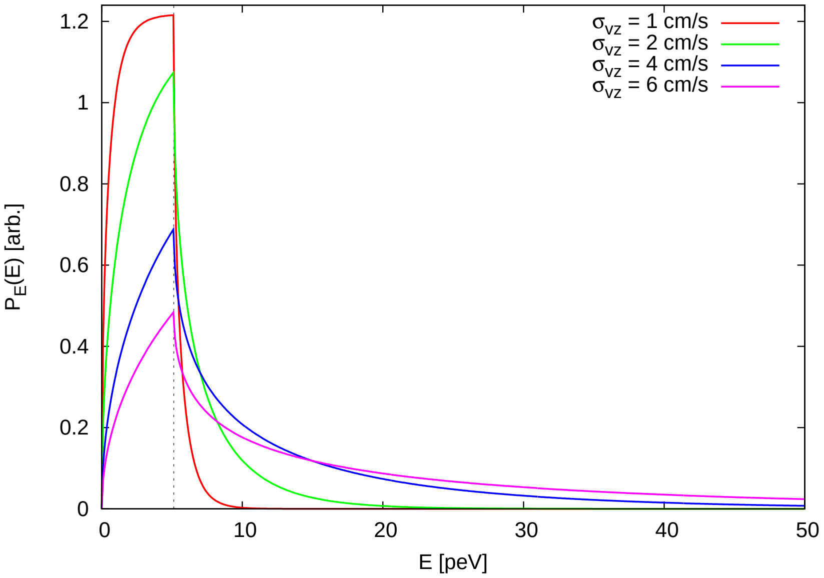

Figure 3.10: The probability distribution for the total energy $P_E(E)$ at the entrance of the waveguide for various values of σ_{vz}. The dashed line corresponds to the potential energy at the scatterer height mgh.

occurs in the continuum. In the given regime of high quantum numbers (see subsection 3.4.1) these two informations are virtually identical and we rewrite (3.33) as

$$\boxed{p_n^{\mathrm{I}}(0) \sim P_E(E_n)} \; . \tag{3.43}$$

From figure 3.10 we see that doing so naturally results in a non-uniform starting population. States ψ_n^{I} with energies E_n close to mgh are favored by the transition while their counterparts with lower or higher energies receive lower populations.

3.5 Fit to the Experimental Data

We now repeat the procedure of fitting the datasets obtained from the CR39 detectors to our quantum mechanical model as described in section 3.3. This time however, we are *not* assuming *equal* starting populations in region I, but we populate the eigenstates following equations (3.43) and (3.41) respectively.

The remaining of the procedure is the same as in section 3.3. Thus we now have *seven* free parameters:

1. The width of the waveguide w,
2. the efficiency of the scatterer per unit length β,
3. the detector resolution σ,
4. the width of the vertical velocity distribution at the waveguide entrance σ_{vz},
5. the offset of the measured distribution z_{off},
6. the norm of the distribution a
7. and the scattered neutron background b_{scatt}.

As we see from figure 3.10 high quantum states are heavily suppressed already by the phase space factor $P_E(E)$, hence we can now restrict the number of eigenstates taken into account in computations to

$$n_{\max} = 25 \ .$$

3.5.1 The 50-μm Measurement (Detector 7)

Let us first look at the measurement with waveguide width $w \approx 50\ \mu$m which we already tried to fit in section 3.3. Again the detector background is taken to be the average track density in the height interval from 26 μm to 80 μm:

$$b_{\text{det.7}} = (6.9 \pm 0.3)\ \mu\text{m}$$

and the data points to fit to equation (3.28) are taken from the region between 70 μm and 200 μm.

The best fit of the model to the data can be seen in figure 3.11. The improvement relative to figure 3.6 is outstanding. The χ^2-test now yields

$$\chi^2 = 138 \text{ at 124 degrees of freedom} \tag{3.44}$$

or

$$\tilde{\chi}^2 = 1.11$$

which corresponds to a probability

$$P(\chi^2) \approx 19\% \ .$$

We can therefore conclude that, with the additional phase space factor $P_E(E)$, the data is now accurately described by the quantum mechanical model we developed throughout this chapter. Table 3.3 summarises the best fit values for the seven free parameters. It is noteworthy that σ_{vz} fits at

$$\sigma_{vz} = (4.0 \pm 2.5)\ \text{cm/s}$$

which lies exactly in the range we estimated in section 3.4.2.

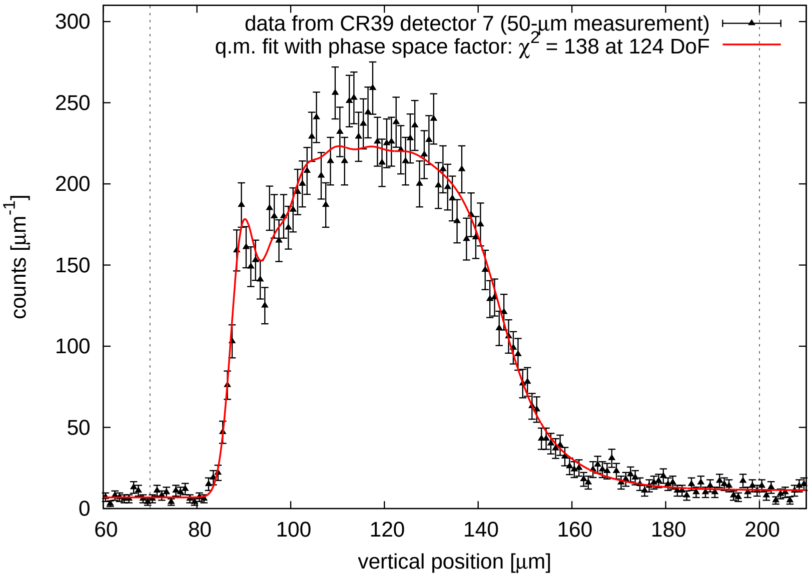

Figure 3.11: The best fit of the data from the 50-μm measurement to the complete quantum mechanical model of the waveguide

parameter	best fit value
waveguide width w	$(51 \pm 2)\ \mu$m
scatterer efficiency β	$(3100^{+1200}_{-800})\ \mathrm{m}^{-1}$
detector resolution σ	$(2.1 \pm 0.4)\ \mu$m
width of velocity spectrum σ_{vz}	(4.0 ± 2.5) cm/s
scattered background b_{scatt}	$(4 \pm 2)\ \mu\mathrm{m}^{-1}$
norm a	$(0.0118 \pm 0.0004)\ \mu\mathrm{m}^{-1}$
offset z_{off}	$(86.2 \pm 0.5)\ \mu$m

Table 3.3: Best values for the free parameters upon fit of the data from the 50-μm measurement (detector 7) to the complete quantum mechanical model of the waveguide.

3.5.2 The 25-μm Measurement (Detector 6)

As we have seen, statistics on the second detector ('detector 6' in figure 2.8) is very low. Obviously, it should have been irradiated longer in order to deliver useful information. Nevertheless, our model should be able to describe the data within it's uncertainties. Unfortunately it turns out that with all seven of the above parameters set free, the fitting routine is unable to localise χ^2-minima for the detector resolution σ and the width of the velocity spectrum σ_{vz}. It seems that the amount information contained in the dataset is just too low for such faint effects to be observable. We therefore fix these two parameters at the best fitting values found from detector 7, as none of them should depend on the waveguide width:

$$\sigma = 2.1\ \mu\text{m}$$

$$\sigma_{vz} = 4\ \text{cm/s}$$

This leaves us with five free parameters for this measurement. The detector background is determined by the data in the region from 20 μm to 70 μm to :

$$b_{\text{det.6}} = (5.4 \pm 0.3)\ \mu\text{m}^{-1}$$

and the fit takes data points in the region from 80 μm to 160 μm] into account. The fit is depicted in figure 3.12 and the values of the five free parameters summarised in table 3.4. The most notable among these is, in this case, the waveguide width w. The fit yields

$$w = (24^{+5}_{-4})\ \mu\text{m}$$

which, at this instance, is in good agreement with the value of 25 μm we aimed at. The statistical test yields

$$\chi^2 = 92 \text{ at } 76 \text{ degrees of freedom,}$$

corresponding to

$$\tilde{\chi}^2 = 1.21$$

or a probability

$$P(\chi^2) \approx 10\%\ ,$$

which means that, although the data is to weak to be conclusive, there is no disagreement with our quantum mechanical description.

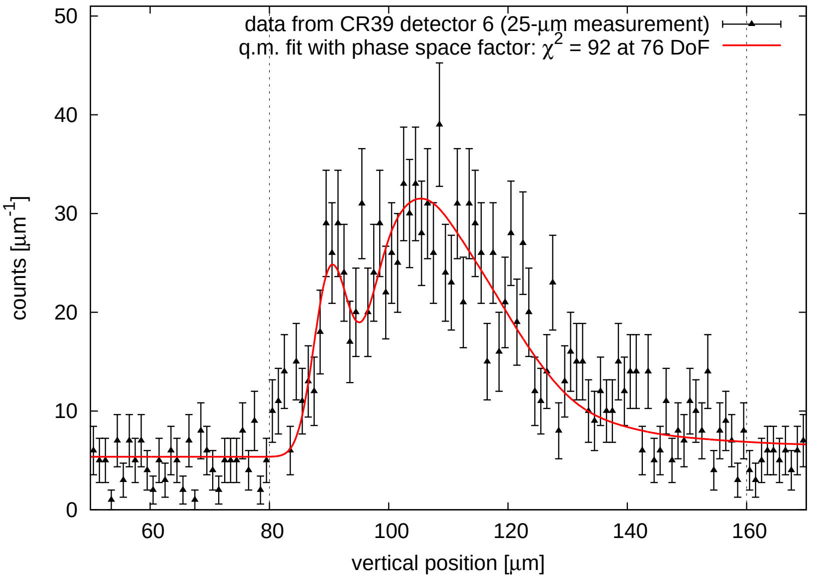

Figure 3.12: The best fit of the data obtained from the 25 μm measurement to the complete quantum mechanical model of the waveguide. The detector resolution σ and the width of the vertical velocity spectrum σ_{vz} are fixed to the values obtained from the 50-μm measurement.

parameter	best fit value
waveguide width w	$(24^{+5}_{-4})\ \mu$m
scatterer efficiency β	$(500^{+900}_{-400})\ \mathrm{m}^{-1}$
scattered background b_{scatt}	$(1 \pm 2)\ \mu\mathrm{m}^{-1}$
norm a	$(0.0008 \pm 0.0001)\ \mu\mathrm{m}^{-1}$
offset z_{off}	$(86 \pm 1)\ \mu$m

Table 3.4: Best values for the free parameters fitting the data from the 25-μm measurement (detector 6) to the complete quantum mechanical model of the waveguide.

Chapter 4

Alternative Interpretations

In the preceding chapter we have developed a quantum mechanical model describing the vertical position measurement of gravitationally bound neutrons. As we have verified, this model is in good agreement with the data obtained from the experiment, itself laid out in chapter 2. Even though this is a very encouraging result, it still does not permit us to claim having observed quantum effects in the gravitational potential. For this it is necessary to rule out possible alternative interpretations of the measurements. In particular, there are two aspects that must be checked:

1. We must verify that we indeed observe a *quantum* phenomenon, i.e. that the data cannot be explained within the framework of classical mechanics.
2. There is in principle the possibility that we *do* face a quantum system but that it is dominated by factors other than the gravitational potential. This scenario also has to be ruled out.

4.1 Classical View of the Experiment

Let us first look at the classical hypothesis. Within such a framework, the neutrons' motion through the waveguide is governed by Newtonian mechanics for point masses alone. We have to check whether the measured height distributions (see figure 2.8) can be explained under such an assumption or not.

In [Rueß00], F. Rueß analytically derives a classical prediction for the distribution of neutron heights in a simplified model of the waveguide. Under the assumption of a 'perfect' scatterer, i.e. one that instantly removes *every* neutron that reaches its surface, and neglecting the effect of the mirror step he arrives at a neutron height density distribution $P_{\text{class}}(z)$ given by

$$P_{\text{class}}(z) \sim \sqrt{h-z} \ , \tag{4.1}$$

where z is the neutron height above the mirror surface at $z = 0$ and h the scatterer position.

However, we are confronted with a setup including a step of height

$$s \approx 13.5 \ \mu\text{m}$$

between the first and the second bottom mirror, as described in section 2. Additionally, our quantum theory accounts for the scatterer action by including an 'efficiency' parameter β which is free and finite. In the classical analogy, this means that a neutron's probability to 'survive' a collision with the scatterer surface may be small, but not equal to zero.

In order to permit a fair comparison between classical and quantum mechanical predictions, equation (4.1) would have to be extended in order to account for these two effects. Paradoxally, this is more complicated to achieve in a classical framework than in the quantum mechanical one.

We will therefore not try to derive an analytical expression for the classical height distribution, but *simulate* it numerically. This can be done with the aid of a simple Monte-Carlo simulation of the neutrons' motion trough the waveguide.

4.1.1 Classical Simulation of the Waveguide

A Monte-Carlo simulation has to provide a numerical model for each elementary process taking place within the system. Let us have a look at figure 4.1 showing a schematic view of the waveguide and illustrating possible processes in the behaviour of *classical* neutrons as they travel it.

Reflection at a Bottom Mirror: In a purely classical model, neutrons in the gravitational field move along parabolic trajectories, i.e. their equations of motion are given by

$$\begin{aligned} x(t) &= v_x t + x_0 && (4.2)\\ z(t) &= -\frac{1}{2} g t^2 + v_{z0} t + z_0 \ , && (4.3) \end{aligned}$$

where x and z are the horizontal and vertical spatial coordinates respectively and t is the time elapsed since the passage at $x = x_0$ and $z = z_0$.

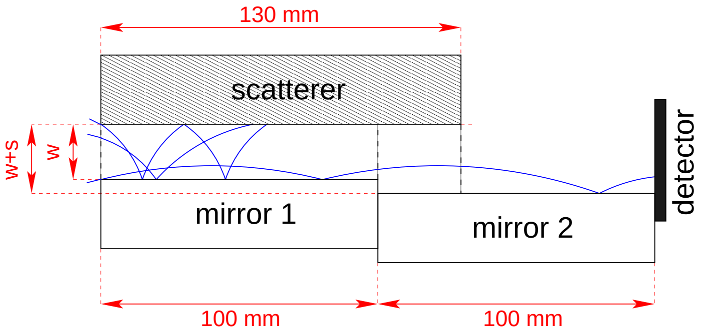

Figure 4.1: Schematic section through the waveguide. Three possible trajectories for classical, point like neutrons are indicated in blue.

Just as in our quantum mechanical analysis, we assume that the mirrors are perfectly plane, totally reflecting surfaces. Suppose a neutron hits the mirror surface placed at $z = z_{\text{mir}}$ at a time $t = t_{\text{mir}}$. According to (4.3) it has, at that moment, a vertical velocity

$$v_z(t_{\text{mir}}^-) = \left.\frac{\partial z(t)}{\partial t}\right|_{t \to t_{\text{mir}}^-} = -g t_{\text{mir}} + v_{z0} \ .$$

Upon reflection at the mirror, the vertical velocity is changed into its opposite, while the motion along the x direction is unaffected:

$$v_z(t_{\text{mir}}^+) = -v_z(t_{\text{mir}}^-) \tag{4.4}$$

Thus, introducing

$$v'_{z0} = v_z(t_{\text{mir}}^+) = g t_{\text{mir}} - v_{z0}$$

and

$$x'_0 = v_x t_{\text{mir}} + x_0 \ ,$$

we can describe the neutron's motion after the mirror collision by the set of equations

$$x(t) = v_x t' + x'_0 \tag{4.5}$$

$$z(t) = -\frac{1}{2} g t'^2 + v'_{z0} t' + z_{\text{mir}} \ . \tag{4.6}$$

This is exactly the same form than equations (4.2) and (4.3). t' now denotes the time since the last mirror collision.

Thus it is clear how to simulate a neutron bouncing above a reflecting surface: Given a neutron on a trajectory of the form (4.2) and (4.3), the simulation has to solve the equation

$$z(t_{\text{mir}}) = z_{\text{mir}} \ , \tag{4.7}$$

where, due to the step, the coordinate of the mirror surface is itself a function of x. The solution t_{mir} yields new starting values for the horizontal and vertical motion components: x_0', v_{z0}' and z_{mir}. From these a new set of equations (4.5) and (4.6) is constructed, which in turn yields the coordinates of the next mirror collision, and so forth.

Interaction with the Scatterer Surface: As is already familiar to us, part of the waveguide is covered by the scatterer. Interaction of neutrons with its surface can be simulated in the following way:

1. Upon each collision with the scatterer, a neutron has a probability P_{scat} to be 'removed' from the system.
2. If the neutron happens to survive the collision (with probability $1 - P_{\mathrm{scatt}}$), it is specularly reflected at the surface of the scatterer just as if it was a mirror.

This parametrisation is in analogy to the quantum mechanical description from chapter 3: The wavefunctions ψ_n^{I} and ψ_n^{II} from equations (3.16) and (3.17) were derived as if the scatterer was a perfectly flat, reflecting boundary at $z = h$. In equation (3.25), we then parametrised the 'removal' mechanism by a scattering probability per unit time β which depends on the quantum number n. In the above classical view, we have a scattering probability per collision P_{scatt}, thus the higher is the number of collisions, the lower are the neutron's chances to pass the waveguide.

Simulation Procedure: Hence, a program simulating a swarm of classical, point like neutrons moving along the waveguide should basically proceed in the following way:

1. At the waveguide entrance at $x = 0$, arbitrary starting values for a neutron's height z_0 above the first mirror as well as for the vertical and horizontal velocities v_{z0} and v_x and are chosen using a random number generator. We know from chapter 3 that the z_0 are uniformly distributed, while the vertical and horizontal velocities have Gaussian distributions:

$$P_{z0}(z_0) = \begin{cases} 1/h & : \quad 0 \le z_0 \le h \\ 0 & : \quad \text{else} \end{cases} \tag{3.39}$$

$$P_{vz}(v_{z0}) \approx \frac{1}{\sqrt{2\pi}\sigma_{vz}} \exp\left[-\frac{1}{2}\left(\frac{v_{z0}}{\sigma_{vz}}\right)^2\right] \tag{3.37}$$

$$P_{vx}(v_x) = \frac{1}{\sqrt{2\pi}\sigma_{vx}} \exp\left(-\frac{1}{2}\frac{(v_x - \overline{v_x})^2}{\sigma_{vx}^2}\right) . \tag{3.34}$$

2. From these starting values, a set of equations of motion as given by (4.2) and (4.3) is constructed.
3. By solving these solutions, the simulation has to determine whether the next collision will take place at the scatterer or at the bottom mirror:
   (a) If the neutron hits the bottom mirror, the solution yields a new set of starting parameters x'_0, v'_{z0} and z'_0, hence new equations of motion (4.5) and (4.6). With these the simulation repeats step 3.
   (b) If the neutron hits the scatterer, a random number generator decides wether it will be destroyed (with probability P_scatt) or survive (with probability $1 - P_\text{scatt}$). If it survives, it is reflected just as in the case of a mirror collision. If it is scattered, it is lost to the system and the simulation continues at step 1 with another neutron.
4. If a neutron reaches the detector, i.e. if $x = x_\text{det}$, its height z above the mirror at that point is registered and the simulation restarts at step 1 with a new particle.

Thus, by repeating the above procedure with a large number of neutrons, we obtain a classical height distribution $\tilde{P}_\text{class}(z)$ analogous to (4.1) but with the effects of the mirror step and of the finite scatterer efficiency correctly taken into account.

Within the framework of this thesis such a simulation ('PingPong') has been written. Thus we can now test if the measured data as depicted in figure 2.8 can be reproduced by the purely classical model laid out above.

4.1.2 Classical Fit to the 50-μm Measurement

As we have seen while fitting the quantum mechanical model to the data, the information contained in the 25-μm measurement (detector 6) is not very conclusive. We shall therefore restrict ourselves to the data from the measurement with 50 μm waveguide width which is by far superior in terms of statistics.

It is clear that the classical simulation of the waveguide, and thereby $\tilde{P}_\text{class}(z)$, directly depends on three parameters: the height of the scatterer above the first mirror h, the classical scatterer efficiency P_scatt and the width of the vertical velocity spectrum σ_{vz}. Additionally, just as in the case of quantum mechanical fits, the fit function must include parameters for norm, offset and background:

$$F_\text{class}(z) = a\ \tilde{P}_\text{class}(z - z_\text{off}) + b_\text{det} + b_\text{scatt}\Theta(z - z_\text{off}) \tag{4.8}$$

Again, b_det and b_scatt are the detector and scattered background respectively, z_off is the offset between the theoretical and measured distributions and a the normalisation factor.

Convolution with the Gaussian corresponding to the detector resolution yields the final distribution to be fitted to the data:

$$\boxed{\tilde{F}_{\mathrm{class}}(z) = \frac{1}{\sqrt{2\pi}\sigma} \int \mathrm{d}z' \; F_{\mathrm{class}}(z') \cdot \exp\left[-\frac{1}{2}\left(\frac{z'-z}{\sigma}\right)^2\right]} \tag{4.9}$$

Hence, the classical model describing the experiment also includes seven free parameters:

1. the height of the scatterer h,
2. the classical scattering probability P_{scatt},
3. the width of the vertical velocity distribution σ_{vz},
4. the detector resolution σ,
5. the scattered neutron background b_{scatt},
6. the offset of the height distribution z_{off}
7. and the norm of the height distribution a.

Comparing this with the fit model from section 3.5, we see that all of these parameters have got their equivalents in the quantum mechanical calculation.

Upon fitting it turned out, that the fit routine could not find an upper limit to σ_{vz}. This behaviour was however expected, as the classical model is over-parametrised in the sense that a broader velocity spectrum can be compensated by a correspondingly high value for the scattering probability P_{scatt}. We therefore fixed σ_{vz} at a set of values between 2 cm/s and 10 cm/s and let the remaining six parameters adapt themselves accordingly. As in section 3.5, the detector background is measured to

$$b_{\mathrm{det.7}} = (6.9 \pm 0.3)\ \mu\mathrm{m}$$

and the fit region goes from 70 μm to 200 μm.

Figure 4.2 shows how the minimum value of χ^2 evolves as the width of the vertical velocity spectrum changes. As we can see, the fit improves rapidly, down to $\chi^2 \approx 215$, for σ_{vz} going from 2 cm/s to 4 cm/s. For larger values of σ_{vz}, χ^2 does not decrease further nor does the fit worsen again. This is the reason why, as mentioned above, a simultaneous fit of all seven parameters cannot find a minimum χ^2.

In section 3.4.2 we estimated that physically meaningful values for the width of the velocity spectrum must be of the order of a few cm/s. There is thus little point

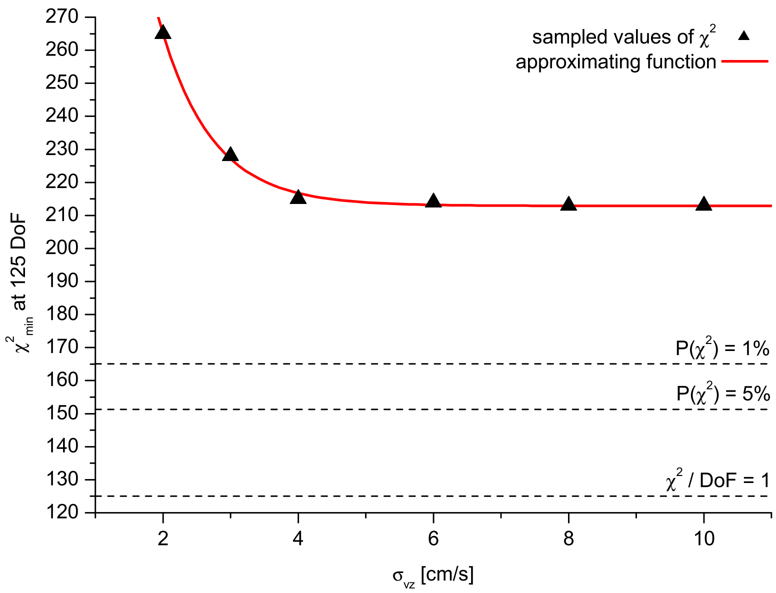

Figure 4.2: The minimum χ^2 of a classical fit to the data of the 50-μm measurement as a function of the width of the vertical velocity distribution σ_{vz}. The red curve approximates the dependence $\chi^2(\sigma_{vz})$ using an exponential decrease.

in sampling at values higher than $\sigma_{vz} = 10$ cm/s and from figure 4.2 it is clear that the statistical test cannot yield a value better than

$$\chi^2 \approx 215 \text{ at 125 degrees of freedom,}$$

corresponding to a reduced χ^2 of

$$\tilde{\chi}^2 \approx 1.72$$

or a probability

$$P(\chi^2) < 10^{-5}.$$

Thus we conclude that the classical model fits to the data badly. Figure 4.3 shows the best fit of the classical prediction to the data for a value of $\sigma_{vz} = 4$ cm/s. Corresponding best fit values for the remaining six parameters are summarised in table 4.1. It is worth pointing out that the classical model agrees with its quantum mechanical counterpart about the width of the waveguide, which fits at approximately 50 μm for both of them.

We conclude with the observation that, given an equivalent set of free parameters, the classical prediction is statistically refuted by the measurement. As is visible

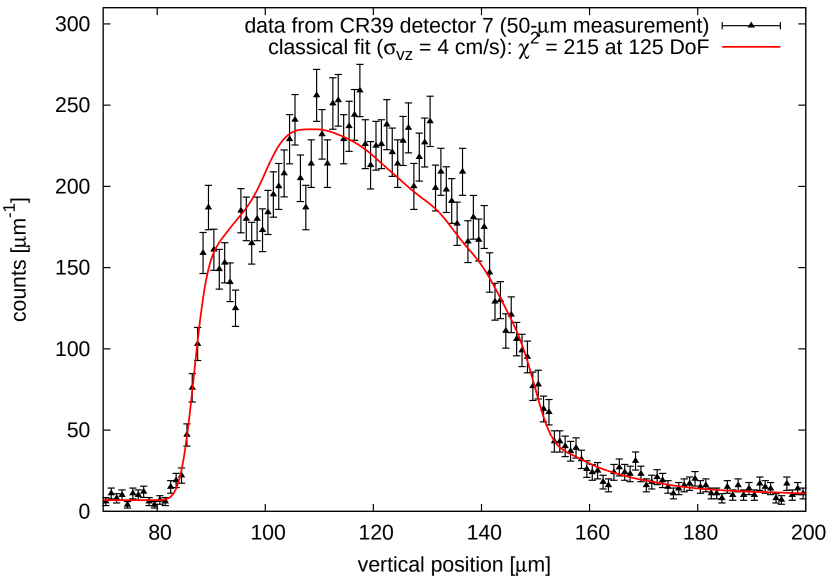

Figure 4.3: The best fit of the data from the 50-μm measurement to the classical model of the waveguide for $\sigma_{vz} = 4$ cm/s.

parameter	best fit value
scatterer height h	(52.2 ± 1.0) μm
scattering probability P_{scatt}	$(32 \pm 3)\%$
detector resolution σ	(1.9 ± 0.6) μm
scattered background b_{scatt}	(2 ± 2) μm^{-1}
norm a	(0.0120 ± 0.0003) μm^{-1}
offset z_{off}	(86.8 ± 0.4) μm

Table 4.1: Best values for the free parameters fitting the data of the 50-μm measurement (detector 7) to the purely classical model of the waveguide. The width of the vertical velocity distribution is fixed at $\sigma_{vz} = 4$ cm/s.

in figure 4.3, it seems to be unable to reproduce the shape of the left part of the measured height distribution which corresponds to neutrons with low energy in their vertical motion component, thus occupying low quantum numbers. This is indeed the part of the dataset where we expect quantum effects to be most dominating. In this sense the measurement of the neutron height distribution yields an analogous result than that of the integral flux (see figure 2.3): In the regime of high energies the system behaves classically while in the limit of low quantum numbers, close to the ground state, the classical prediction fails.

4.2 The Gravityless View

In the time of integral flux measurements a critique put forward about our experiment was the hypothesis that the measurements were ambiguous in the sense that it was not clear that the effect observed in the neutron count rate was indeed *gravitationally* induced. In [Han02] and [Han03], J. Hansson *et al.* tried to deduce the threshold effect in the count rate (see section 2.3) from a quantum mechanical model taking into account geometric boundary conditions only, i.e. neglecting the gravitational potential inside the waveguide. These arguments have already been addressed by V. Nesvizhevsky *et al.* in [Nesv03].

Now that we can directly image the neutrons' probability density in position space, we may be in able to refute the gravityless hypothesis in a much more direct way. In this section we are going to develop a quantum mechanical model of the waveguide neglecting gravity and will show that the height distribution measured using the CR39 detector cannot be explained within this framework.

4.2.1 The Waveguide without Gravity

Let us have another look at the schematic drawing of the waveguide in figure 3.2: Once more we have to solve the Schrödinger equation in each of the three regions I, II and III. Additionally, we need to address the problem of transitions from on region to another. Thanks to our detailed treatment from chapter 3 much of this work has already been done as we are able to reuse some of our previously obtained results.

Regions I and II

Regions I and II of the waveguide can be treated in complete analogy to chapter 3. Neglecting the gravitational potential simply means that a neutron confined between bottom mirror and scatterer corresponds to a particle bound in an infinitely high square well potential.

This problem is treated in any text on one-dimensional quantum mechanics [Schwa98]: Consider an eigenstate $\tilde{\psi}_n^{\mathrm{I}}$ of region I, i.e. confined between the mirror surface at $z = 0$ and the scatterer at $z = h$, but not subject to any other potential. The well-known solution to this problem is

$$\tilde{\psi}_n^{\mathrm{I}}(z) = \begin{cases} \sqrt{\frac{2}{h}}\ \sin\left(\frac{n\pi z}{h}\right) & : \quad 0 < z < h \\ 0 & : \quad \text{else} \end{cases} . \tag{4.10}$$

Correspondingly, an eigenstate $\tilde{\psi}_n^{\mathrm{II}}$ of region II which is limited by the second mirror at $z = -s$ and the scatterer at $z = h$ is given by

$$\tilde{\psi}_n^{\mathrm{II}}(z) = \begin{cases} \sqrt{\frac{2}{h+s}}\ \sin\left(\frac{n\pi(z+s)}{h+s}\right) & : \quad -s < z < h \\ 0 & : \quad \text{else} \end{cases} . \tag{4.11}$$

In region I or II, the neutrons wavefunction will thus be a linear combination of eigenstates $\tilde{\psi}_n^{\mathrm{I}}$ or $\tilde{\psi}_n^{\mathrm{II}}$ respectively, given by equations (4.10) and (4.11). The populations p_n^{I} and p_n^{II} of these eigenstates are governed by the mechanisms we already know from chapter 3:

1. Within one region the states decay due to the scatterer action according to equation (3.25)

   $$p_n(L) = p_n(0)\exp\left(-\beta\ L \int_w^{w+2\rho} \mathrm{d}z \left|\tilde{\psi}_n(z)\right|^2\right) ,$$

   where only the bound states in the gravitational potential are to be replaced by their counterparts from equations (4.10) and (4.11).

2. The repopulation caused by the transition from region I to region II is calculated in the ‘sudden approximation’, i.e. given by equation (3.21):

   $$p_n^{\mathrm{II}} = \sum_m p_m^{\mathrm{I}} \left|\langle\tilde{\psi}_n^{\mathrm{II}}|\tilde{\psi}_m^{\mathrm{I}}\rangle\right|^2$$

3. As for the starting populations, the phase space factor derived in chapter 3 cannot be reused as it is true only in the case of neutrons falling in gravity. As we know that the effect of the starting population on the height distribution is relatively small, we will, in a first order approximation, neglect it and assume that at the entrance of the wave guide, all eigenstates are equally populated:

   $$p_n^{\mathrm{I}} \sim 1 \quad \text{for all } n.$$

Region III

The neutrons behaviour in region III is not obvious anymore. As the gravitational potential is now gone, there simply *are* no bound states in region III. The wavefunction is well limited by the bottom mirror, but free to propagate in the positive z direction.

In this situation it is reasonable to switch to a new coordinate system, where the origin of heights is located at the middle of the waveguide exit:

$$z \longrightarrow z' = z - \frac{a}{2} \; , \tag{4.12}$$

where

$$a = h + s \tag{4.13}$$

is the total width of the waveguide exit in region II.

Thus we are facing a time dependent problem. In absence of any potential, the neutron's wavefunction in region III is a linear combination of free-particle states. Its most general form is [Schwa98]

$$\psi^{\mathrm{III}}(z', t) = \frac{1}{\sqrt{2\pi}} \int \mathrm{d}k \; A(k) \; \exp[\mathrm{i}(kz' - \omega t)] \; , \tag{4.14}$$

where k is the wave number, linked to the frequency ω by the dispersion relation

$$\omega = \frac{\hbar k^2}{2m} \; . \tag{4.15}$$

The shape of the wave packet (4.14) is defined by the *spectral function* $A(k)$. We want to know how an eigenstate $\tilde{\psi}_n^{\mathrm{II}}$ evolves after leaving region II at the time $t = 0$. Hence, we know that, at $t = 0$, the wavefunction (4.14) is equal to $\tilde{\psi}_n^{\mathrm{II}}$:

$$\psi^{\mathrm{III}}(z', 0) \equiv \tilde{\psi}_n^{\mathrm{II}}(z') = \frac{1}{\sqrt{2\pi}} \int \mathrm{d}k \; A(k) \; \exp(\mathrm{i}kz') \tag{4.16}$$

Thus we see that the spectral function $A(k)$ is equal to the Fourier transform ($\mathcal{FT}$) of $\tilde{\psi}_n^{\mathrm{II}}(z')$. In our new coordinate system, centred on the waveguide exit, the latter reads

$$\tilde{\psi}_n^{\mathrm{II}}(z') = \begin{cases} \sqrt{\frac{2}{a}} \; \sin\left(\frac{n\pi(z'-a/2)}{a}\right) & : \quad -a/2 < z' < a/2 \\ \qquad 0 & : \qquad \text{else} \end{cases} \; .$$

Inserting this into equation (4.16) we find

$$\begin{aligned} A(k) &= \frac{1}{a\pi} \int_{-a/2}^{a/2} \mathrm{d}z' \sin\left(\frac{n\pi(z'-a/2)}{a}\right) \exp(-\mathrm{i}kz') \\ &= \frac{1}{\sqrt{a\pi}} \frac{an\pi \exp(-\mathrm{i}ka/2) \; [1 - \exp(\mathrm{i}ak)\cos(n\pi)]}{a^2k^2 - \pi^2 n^2} \\ &=: A_n(k) \; . \end{aligned}$$

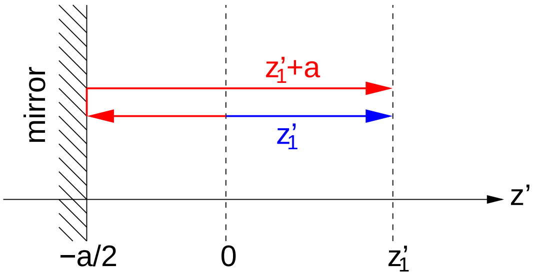

Figure 4.4: Schematic view of the reflection of a partial wave at the bottom mirror in a reference frame centred on the waveguide exit. For any given z', the distance covered by the reflected wave is $z' + a$. Upon reflection, the wave is phase-shifted by an angle π.

In other words, the spectral function $A_n(k)$ depends on the quantum number n of the original state $\tilde{\psi}_n^{\mathrm{II}}$:

$$\boxed{A_n(k) = \mathcal{FT}\left[\tilde{\psi}_n^{\mathrm{II}}(z')\right]} \tag{4.17}$$

Thus every eigenstate $\tilde{\psi}_n^{\mathrm{II}}$ emerging from region II leads to a wave packet in region III given by

$$\psi_n^{\mathrm{III}}(z',t) = \frac{1}{\sqrt{2\pi}} \int \mathrm{d}k \; A_n(k) \; \exp\left(\mathrm{i}kz' - \mathrm{i}\frac{\hbar k^2}{2m}t\right) \; . \tag{4.18}$$

Now we need to account for the presence of the bottom mirror, which in the new coordinate system is located at $z' = -a/2$. Upon reflection at the mirror surface a partial wave with wave number k inverts its propagation direction. Look at figure 4.4 for an illustration of this process: We see that at any given coordinate z', the reflected wave has traveled a distance $a + z'$. Additionally, reflection at the mirror has shifted its phase by an angle π. The complete wavefunction in region III is, at each space coordinate z', the superposition of incident and reflected waves. Thus we have to modify (4.18) into:

$$\boxed{\tilde{\psi}_n^{\mathrm{III}}(z',t) = \begin{cases} \frac{1}{\sqrt{2\pi}} \int \mathrm{d}k \; A_n(k) \; [\exp(\mathrm{i}kz') + \exp(-\mathrm{i}k(a+z') + \mathrm{i}\pi)] & \\ \qquad\qquad \cdot \exp\left(-\mathrm{i}\frac{\hbar k^2}{2m}t\right) & : \; z' > -\frac{a}{2} \\ 0 & : \; z' \leq -\frac{a}{2} \end{cases}} \tag{4.19}$$

The corresponding expression $\tilde{\psi}_n^{\mathrm{III}}(z,t)$ in our familiar coordinate system centred at the mirror surface can be obtained using the coordinate transformation (4.12) and equation (4.13).

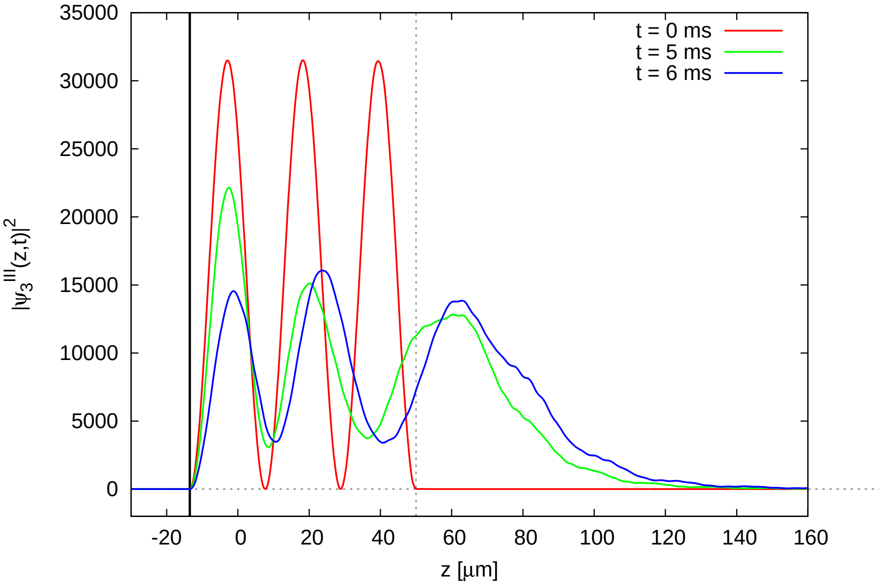

Figure 4.5: Evolution of the spatial probability density in region III of the waveguide for an initial bound state with quantum number $n = 3$. The solid and dashed vertical lines indicate the positions of the bottom mirror and scatterer respectively.

Together with (4.17), equation (4.19) describes the evolution of an eigenstate $\tilde{\psi}_n^{\text{II}}$ after it has left region II at the time $t = 0$. Figure 4.5 provides an illustration of this process, taking the third eigenstate as an example.

4.2.2 Gravityless Fit to the 50-μm Measurement

We want to know if the gravityless description of the waveguide we just developed can describe the measured neutron height distributions. For this we need to construct a fit function from the quantum theory of region III laid out above.

In analogy to chapter 3 we assume that a neutron's position probability density in region III is an incoherent superposition of the wave packets given by equation (4.19):

$$\left|\tilde{\Psi}^{\text{III}}(z,t)\right|^2 = \sum_n p_n^{\text{II}}(L^{\text{II}}) \left|\tilde{\psi}_n^{\text{III}}(z,t)\right|^2$$

As usual, the populations $p_n^{II}(L^{\text{II}})$ depend on the scatterer height and efficiency in regions I and II. We see that, although there are no interference terms, the probability density $|\tilde{\Psi}^{\text{III}}(z,t)|^2$ is time-dependent. This reflects the fact that we are

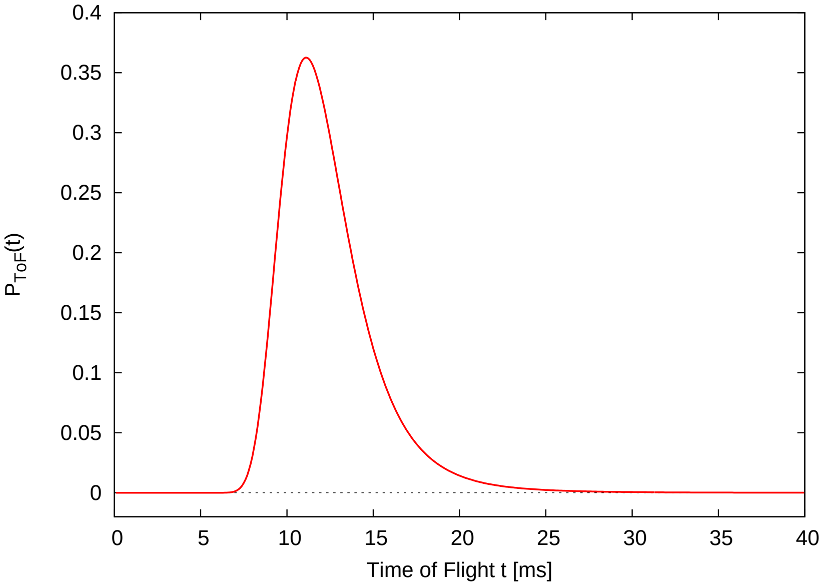

Figure 4.6: Time-of-flight spectrum for neutrons arriving at the detector after having left region II of the waveguide at $t = 0$.

now dealing with *running* wave packets in region III whose shapes depend on time (c.f. figure 4.5).

Thus, in order to obtain the time-independent height distribution, $|\tilde{\Psi}^{\mathrm{III}}(z,t)|^2$ has to be convoluted with the neutron's time-of-flight spectrum $P_{\mathrm{ToF}}(t)$ when covering the distance $L^{\mathrm{III}} = 7$ cm. The latter is shown in figure 4.6.

With the usual free parameters for detector and scattered neutron background b_{det} and b_{scatt}, for the norm a and for the offset z_{off} of the distribution, we construct the fit function for a gravityless setup:

$$F_{\mathrm{noG}}(z) = a\left(\int \mathrm{d}t\ P_{\mathrm{ToF}}(t)\ \left|\tilde{\Psi}^{\mathrm{III}}(z - z_{\mathrm{off}}, t)\right|^2\right) + b_{\mathrm{det}} + b_{\mathrm{scatt}}\Theta(z - z_{\mathrm{off}}) \qquad (4.20)$$

Convolution with the detector resolution σ yields

$$\boxed{\tilde{F}_{\mathrm{noG}}(z) = \frac{1}{\sqrt{2\pi}\sigma}\int \mathrm{d}z'\ F_{\mathrm{noG}}(z')\cdot\exp\left[-\frac{1}{2}\left(\frac{z'-z}{\sigma}\right)^2\right]}\ , \qquad (4.21)$$

which is the final function to be fitted to the data.

Again, we want to fit the model to the data from the 50-μm measurement ('detector 7'). Upon doing so it quickly turns out that the gravityless model fits the data *very* badly. In order to allow the fitting program to work at all, several of the parameters had to be held constant:

1. The detector resolution σ was set to a value of $\sigma = 2.1\ \mu$m obtained from the previous fits to the data.
2. The scattered neutron background had to be neglected completely by setting $b_{\text{scatt}} = 0\ \mu\text{m}^{-1}$.
3. The scatterer efficiency β seemed to be constantly running towards arbitrarily high values. Following the same procedure than for the classical fits, we therefore sampled different values of β and had the fit routine search for the corresponding minimum χ^2.

The remaining free parameters are thus:

1. The waveguide width w,
2. the offset of the height distribution z_{off} and
3. the norm of the distribution a.

As usual the detector background is measured to be

$$b_{\text{det}} = (6.9 \pm 0.3)\ \mu\text{m}^{-1} \ .$$

The data points taken into account in the fit range from 60 μm to 200 μm.

Figure 4.7 summarises the best values of χ^2 for different values of the scatterer efficiency β. It is worth mentioning that, in figure, the scatterer efficiency has been sampled up to unreasonably high values: The computation shows that, for a value of $\beta = 5 \cdot 10^6$, the state populations at the exit of region II are

$$p_n^{\text{II}}(L^{\text{II}}) \approx 10^{-41}$$

which means that the overall transmission probability for a neutron would practically be zero, in disagreement with the finite neutron flux that has been measured.

It is therefore quite obvious from figure 4.7 that at any reasonable values of β, χ^2 will never drop beneath a value of

$$\chi^2 \approx 850 \text{ at 137 degrees of freedom}$$

corresponding to a reduced χ^2 of

$$\tilde{\chi}^2 \approx 6.2$$

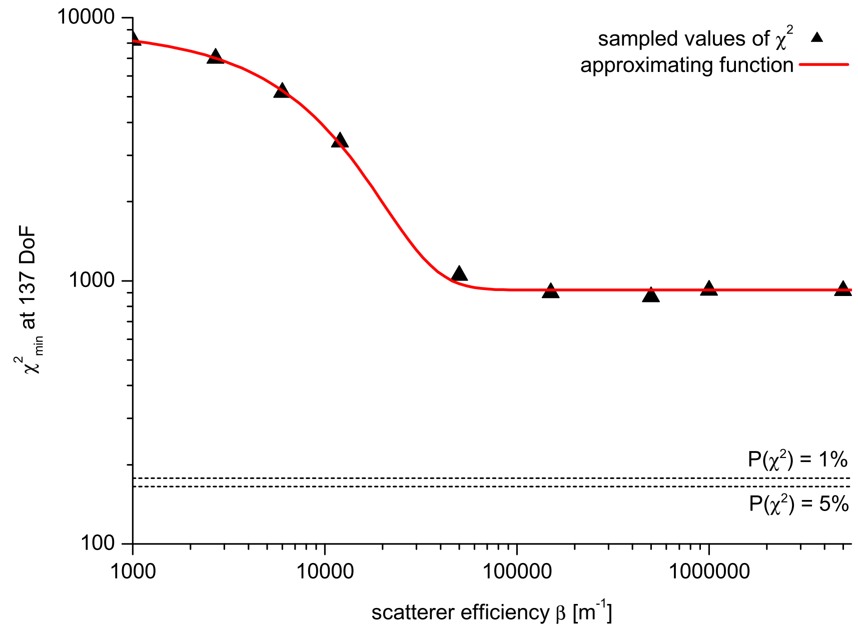

Figure 4.7: The evolution of the minimum χ^2 as a function of the scatterer efficiency. The red curve approximates the dependence $\chi^2(\beta)$ using an exponential decrease. Note the logarithmic scales.

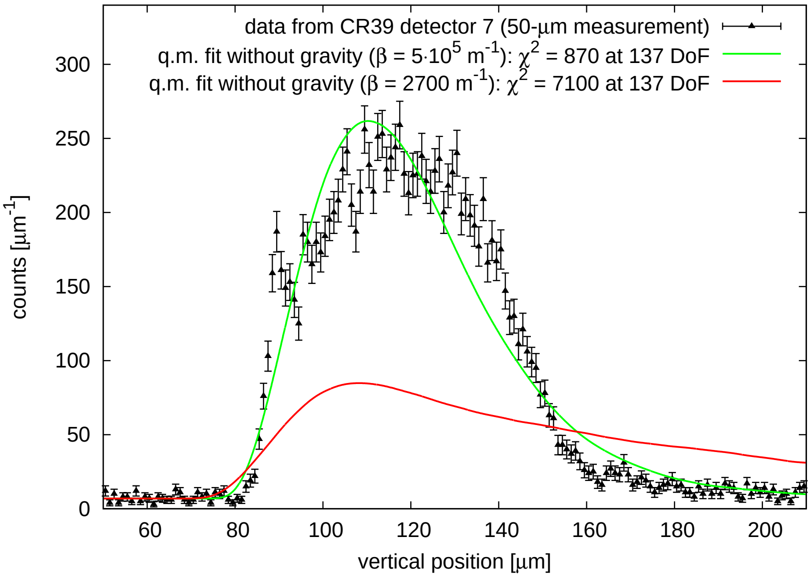

Figure 4.8: The best fits of the gravityless quantum theory to the data from the 50-μm measurement for two different values of β. Obviously, the model does not describe the data at all.

or a probability

$$P(\chi^2) < 10^{-100} \ .$$

Confronted to such devastating a result, we may safely conclude that predictions from a gravityless theory of the experiment are in contradiction with the measured height distributions. Figure 4.8 shows the best ‘fits’ to the data for two different values of β. Unlike the classical model, which can at least describe the high energetic part of the dataset, the quantum theory we derived neglecting gravity is unable to reproduce the shape of the neutron height distribution even on the largest scale.

Chapter 5

Gravity at Small Length Scales

Over the last decade a number of theories aiming at a quantum field description of gravity have arisen which predict deviations from Newtonian gravity at small but experimentally accessible length scales. As a consequence, there is today a renewed interest in experimental probes of the gravitational potential at distances below 1 mm.

Our experiment observes gravitationally bound quantum systems of characteristic sizes around 10 μm, thus in principle it probes the gravitational potential (1.8) at distances of this order of magnitude or below. Upper limits on the deviations from Newtonian gravity have already been derived from integral flux measurements performed with our experiment and are reported in [Abe03] and [Nesv04].

Within the framework of this thesis, we want to determine if such upper limits can also be obtained from the measurements of neutron height distributions described in this text.

5.1 Deviations from Newtonian Gravity

The most accurate model of gravity available today is provided by the General Theory of Relativity. It describes the attraction of masses from cosmological length and energy scales down to everyday phenomena. Newton's law of gravitation (1.8) which we have used all through the preceding chapters is no more than the non-relativistic limit of Einstein's field equations. Yet, General Relativity being a classical field theory, it is expected to fail on the scale of elementary particles, whose dynamics is known to be governed by quantum physics.

The views of the universe inherent to Quantum Theory and General Relativity are so radically different that this antagonism is commonly regarded as one of the most challenging physical problems of our time. For decades, theoreticians have sought to bridge this gap between gravity and the three other fundamental interactions. The most promising models aiming in this direction have become known under the collective name of *'String Theories'*. Therein the fundamental constituents of matter and the field bosons are seen as excitations of underlying one-dimensional objects called 'strings'. The mathematics of these theories requires that the strings themselves 'live' in an eleven-dimensional space-time. However, General Relativity, Quantum Field Theory, and eventually everyday experience tell us that our world is effectively characterised by a four-dimensional space-time. For the three non-gravitational interactions, high energy physics has established that this effective four-dimensionality holds down to the length scale of quarks and leptons.

String theories account for this by assuming that seven of the spatial dimensions present on the string scale bend back into themselves. These *extra-dimensions* are thereby *compactified*, usually down to the Planck length scale of 10^{-35} m, such that no interaction between particles can be mediated through them at larger distances. This ensures that such theories are not in contradiction to present experimental results but it also leaves little hope of probing their predictions in the not-too-distant future.

However, a few years ago it was shown [Ark98] [Ark99] that it is also possible to construct frameworks in which the three non-gravitational interactions are confined to four space-time dimensions while gravity could, in addition, propagate through one or more *large extra-dimensions*. The latter might then have compactification radii of up to one millimeter, such that deviations from Einsteinian gravity could be observable at these length scales.

It can be shown [Ark98] that such admixture of large extra-dimensions mediating gravity would lead to an additional short-ranged term in the gravitational potential $V(r)$ for two masses m_1 and m_2 separated by the distance r:

$$V(r) = -G\,\frac{m_1 m_2}{r}\,\left[1 - \alpha\ \exp\left(-\frac{r}{\lambda}\right)\right] \tag{5.1}$$

A detailed calculation can also be found in [Wes01]. The left part of equation (5.1) is the usual Newtonian gravitational potential as in equation (1.8), while the exponential Yukawa-like term contains the additional interaction at short distances due to large extra dimensions. The latter is often referred to as the *'fifth force'*. λ corresponds to the range of the additional interaction while α parametrises its strength in units of the gravitational constant G. It can be shown [Wes01] that, in contrast to 'normal' gravity, this short ranged potential can be both attractive or repulsive, i.e. α may be positive or negative.

A good summary of present experimental limits on the fifth force parameters α and λ is provided by figure 5.1 which is taken from [Hoy04]. The constraints on $|\alpha|$

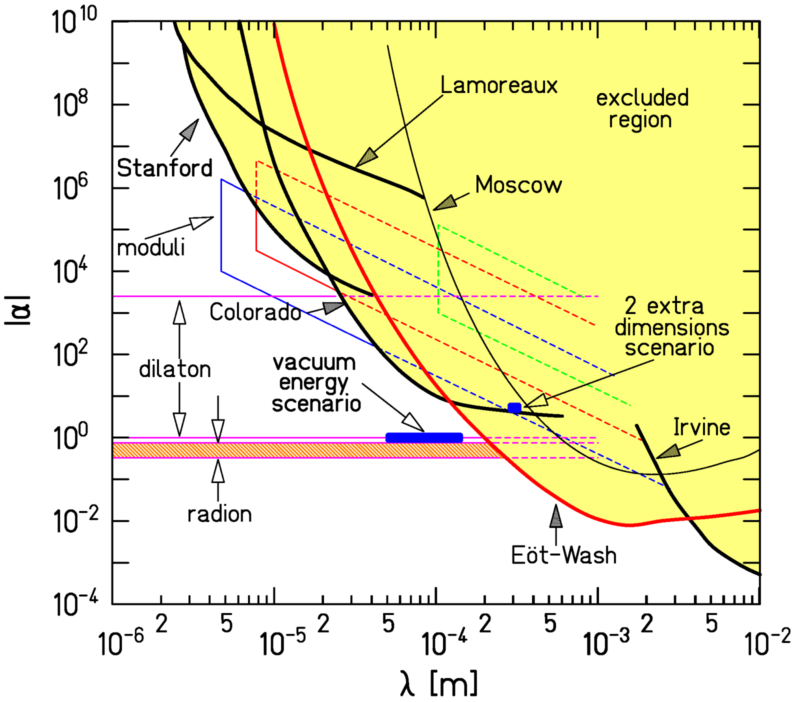

Figure 5.1: Current experimental constraints on a hypothetic short-ranged admixture to the gravitational potential as given by equation (5.1). The excluded region is marked in yellow. The picture is taken from [Hoy04]. For an explanation of annotations see [Hoy04] and references therein.

are very restrictive for ranges λ of 1 mm and up. At smaller length scales however, the precision of the mechanical experiments normally used to probe gravity worsens considerably, and below 3 μm $|\alpha|$ might be as large as 10^{10}.

A few micrometers is precisely the length scale of the gravitationally bound quantum states we observe in our experiment. From the integral flux measurement of 1999 (c.f. figure 2.3) H. Abele *et al.* derived an upper limit [Abe03]

$$|\alpha|_{\max} \approx 10^{12} \ , \tag{5.2}$$

corresponding to a 90% confidence interval, for values of λ between 1 μm and 10 μm. In [Nahr05] S. Nahrwold confirmed this limit using data from another integral flux measurement of 2002.

Within the framework of this thesis we want to elucidate the question if such limits can also be obtained from the height distribution measurements presented in chapter 2. This means that we have to extend the quantum mechanical description developed in chapter 3 in such a way that it incorporates the fifth force strength and range, α and λ, as two additional parameters.

5.2 A Model of the Experiment including Fifth Forces

In principle the effect of a hypothetic non-Newtonian gravity can easily be included in our quantum mechanical calculations. We are interested in small values of λ only, thus a neutron inside the waveguide will be subject only to fifth force admixtures caused by the mirrors and scatterer. As for its gravitational interaction with the Earth or even with other elements of the experimental setup, the effect of the Yukawa-like term in (5.1) is negligible due to its exponential decrease.

Hence we derive from equation (5.1) that a neutron located at a height z above the mirror of mass density ρ_{m} has a gravitational potential energy

$$U_{\mathrm{mir}}(z) = mgz + 2\pi m \rho_{\mathrm{m}} G \alpha \lambda^2 \ \exp\left(-\frac{z}{\lambda}\right) \ , \tag{5.3}$$

where we have taken the mirror to have infinite volume and integrated r over the corresponding half-sphere of infinite radius. A detailed calculation can be found e.g. in [Wes01].

A neutron located between a mirror and the scatterer placed at $z = h$ feels an additional short ranged force from the scatterer surface:

$$U'(z) = mgz + 2\pi m \rho_{\mathrm{m}} G \alpha \lambda^2 \left[\exp\left(-\frac{z}{\lambda}\right) + \exp\left(-\frac{h-z}{\lambda}\right)\right] \tag{5.4}$$

However, the scatterer surface is not flat but characterised by a roughness of amplitude $\rho \approx 0.75\ \mu$m. This leads [Wes04] to a small correction that has to be applied to (5.4) and yields

$$U_{\mathrm{mir/sca}}(z) = mgz + 2\pi m \rho_{\mathrm{m}} G \alpha \lambda^2 \left[\exp\left(-\frac{z}{\lambda}\right) + \exp\left(-\frac{h-z}{\lambda}\right) C(\rho, \lambda)\right] \ , \tag{5.5}$$

with

$$C(\rho, \lambda) = 1 + \frac{\exp(2\rho/\lambda)(2\rho - \lambda) + \lambda}{2\rho} \ .$$

From figure 3.2 we see that, in regions I, II and III of the waveguide, a neutron is subject to gravitational potentials of the forms (5.5) or (5.3) respectively, where the origin of heights $z = 0$ has to be adapted according to the mirror step. Figure 5.2 depicts the shape of the gravitational potential in region III of the waveguide for $\lambda = 2\ \mu$m and three different values of α. Just as in chapter 3 we need to find eigenstates of the Schrödinger equation for every region of the waveguide.

The potentials (5.3) and (5.5) are too complicated to allow any analytic treatment, hence, eigenstates and eigenvalues have to be computed numerically for each couple of values α and λ. Given the large number – 25 – of states we want to include in our fits, this is quite laborious a task even for a fast personal computer, yet there are no fundamental difficulties in this procedure. As an example, figure 5.3 shows the second eigenstate of region III of the waveguide for different Yukawa admixtures. It is clearly visible how a positive value of α repells the wavefunction from the mirror surface, while a negative one attracts it.

5.2.1 Fitting the Experimental Data

The eigenstates derived from (5.3) and (5.5) can easily be inserted into our quantum mechanical theory of the waveguide from chapter 3: They just replace their counterparts from equations (3.16), (3.17) and (3.9), the principles of the model remain untouched: The starting populations of the states are governed by the phase space factor (3.41), the states' decay due to the scatterer is parametrised by equation (3.25), and repopulations at mirror step and scatterer edge are computed in the sudden approximation.

However, in order to reduce the amount of numerical computation required, we have to make two restrictions:

1. We fix the waveguide width w at the value obtained from the 'normal' quantum mechanical fit:
$$w = (52.6 \pm 2.0)\ \mu\text{m}$$
This effectively reduces the number of eigenstates to be numerically computed by a factor of ten. Without this limitation, the overall computation time would have been forbiddingly long (several weeks) which we cannot afford within the timeframe of this diploma work. However, since the waveguide width has not been measured independently, this means that the analysis to follow *cannot* yield experimental limits on α. It should rather be regarded as a feasibility study, telling us what constraints on the fifth force *could* be obtained from our experiment had the scatterer height been precisely measured.

2. We restrict ourselves to *two* values of the fifth force range λ, namely $\lambda = 2\ \mu$m and $\lambda = 4\ \mu$m.

Within these restrictions, we fit the model to the data obtained from the 50-μm measurement shown in figure 2.8. For the two values of λ we sample α in the range from -10^{14} to 10^{14} and let the remaining six parameters, described section 3.5, adapt themselves accordingly. By taking note of every corresponding best fit value

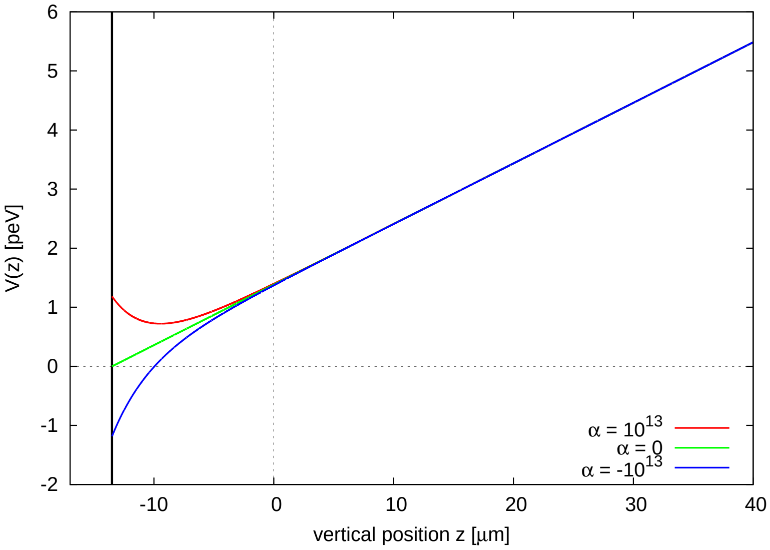

Figure 5.2: The neutrons potential energy above the second mirror in region III for an attractive, a repulsive and no fifth force at all. The solid vertical line represents the mirror surface. The fifth force range λ is set to 2 μm.

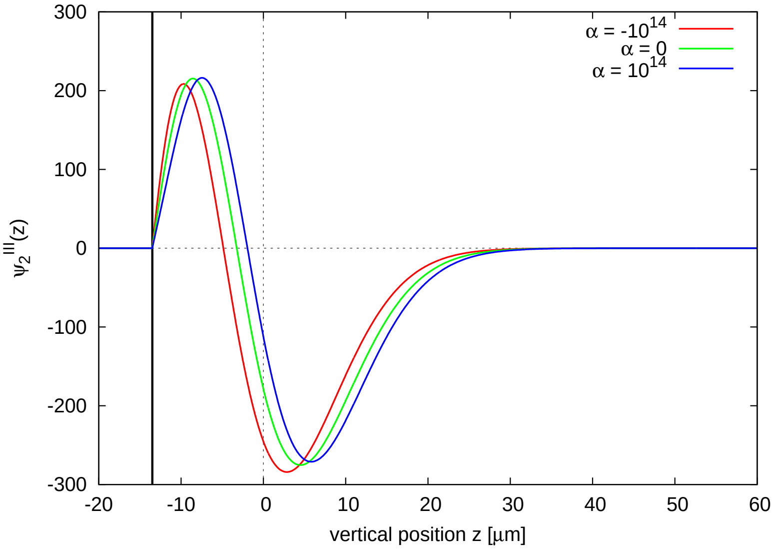

Figure 5.3: The second eigenstate of region III for different values of α and $\lambda = 2$ μm. The solid vertical line represents the mirror surface.

of χ^2, we obtain the functional dependences

$$\chi^2(\alpha)$$

for both given values of λ. These are shown in figure 5.4, the sampled values of $\chi^2(\alpha)$ have been interpolated into fourth-order polynomials plotted in red. The intersections of the latter with the dashed vertical lines correspond to 90% confidence limits of the best fit values of α.

5.2.2 Discussion of the Fit Results

For the given values of λ, the fit yields best values of α of

$$\alpha = (-3.8^{+2.5}_{-2.3}) \cdot 10^{13} \quad \text{for } \lambda = 2\ \mu\text{m}$$

and

$$\alpha = (-4.5^{+2.9}_{-2.8}) \cdot 10^{12} \quad \text{for } \lambda = 4\ \mu\text{m}.$$

The corresponding 90% confidence limits can be seen in figure 5.4. Although not centred at zero, they are in rough agreement with $\alpha = 0$, thus not indicating evidence for deviations from Newtonian gravity within the framework of this feasibility study.

In our interpretation, the most likely source of misunderstood systematics is the scatterer, whose neutron ‘removal’ mechanism we have modeled in a very heuristic way. Although the parametrisation (3.25) describes the process well enough to obtain good fits in the realistic situation of normal, Newtonian gravity, fits of α and λ seem to overstress it. Additionally, considering the scatterer efficiency β a *free* parameter in principle contradicts physical reality: the efficiency should be a pure surface property of the scatterer, independent of α and λ. However, as mentioned in chapter 3, work aiming at a quantum mechanical understanding *ab initio* of the scattering mechanism is underway [Vor05] [Wes06]. Such a complete theory of the scatterer should eventually allow to derive the efficiency of the scatterer from measured quantities.

Within the feasibility study the present analysis is, we can simulate this situation by repeating the above fitting process with the efficiency parameter β held constant at the value obtained under the assumption of non-existent fifth forces. In an analogous way than laid out above we then obtain 90% confidence regions for α of

$$\alpha_{\min} = -1.2 \cdot 10^{13},\ \alpha_{\max} = 0.8 \cdot 10^{13} \quad \text{for } \lambda = 2\ \mu\text{m}$$

and

$$\alpha_{\min} = -2.6 \cdot 10^{12},\ \alpha_{\max} = 1.0 \cdot 10^{12} \quad \text{for } \lambda = 4\ \mu\text{m}$$

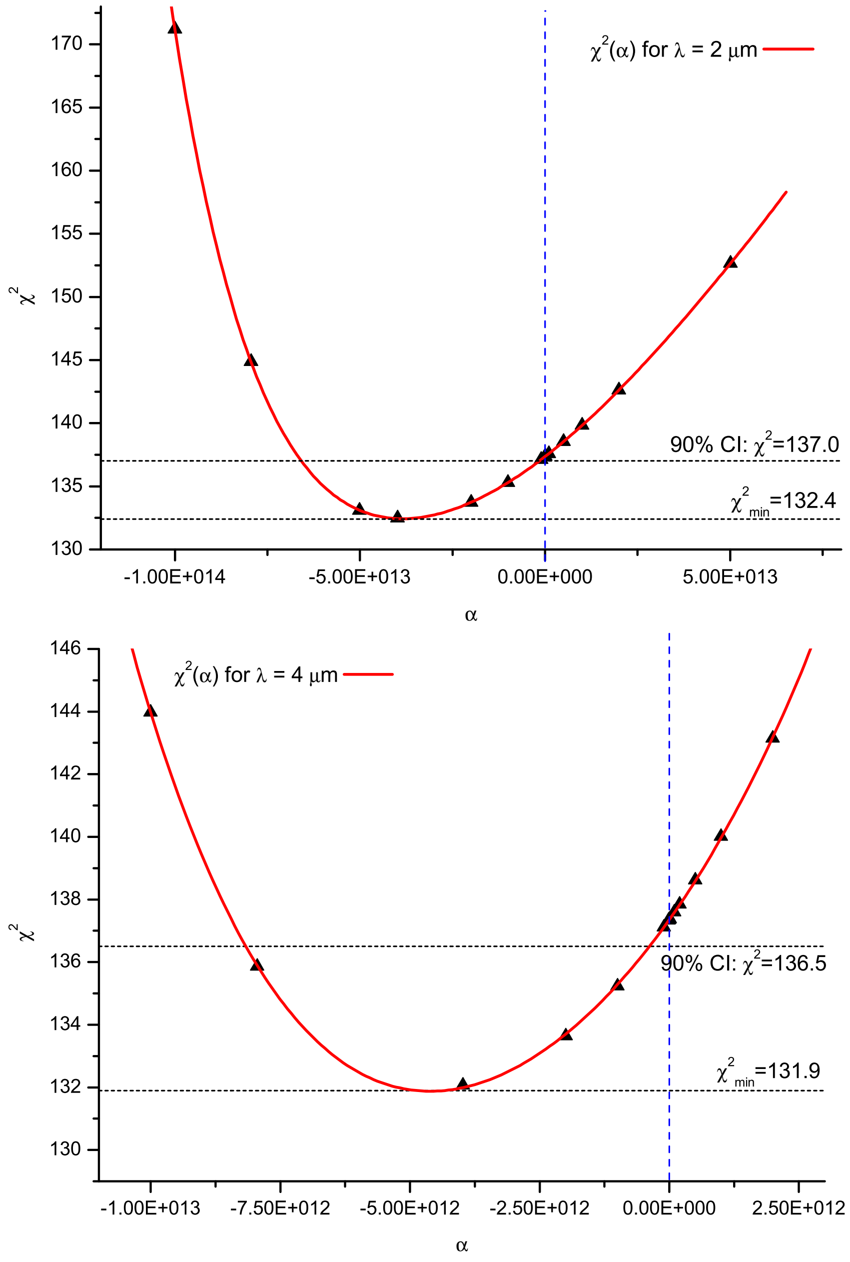

Figure 5.4: χ^2 minima upon fitting the quantum mechanical model including fifth forces to the data from the 50-μm measurement. The red curves are fourth-order polynomials approximating the sampled values of $\chi^2(\alpha)$. Their intersections with the dashed lines delimit the 90% confidence intervals for the best fit value of α.

Hence, we can gain approximately half an order of magnitude. These limits on α are in the same order of magnitude than those derived from integral flux measurements [Nahr05]. Thus we have to conclude that, in the present situation of not well understood scatterer action and statistics limited by the very low UCN flux density, position sensitive measurements of a neutron's probability density above a mirror cannot be used to derive upper limits on fifth forces more competitive than those we already have.

Summary

Within the framework of this diploma thesis we have carried out an experiment at the *Institut Laue Langevin* to detect bound quantum states of ultracold neutrons in the Earth's gravitational potential. Operating the existing experimental installation, we have used position resolving neutron detectors in order to directly image the height distribution of neutrons bouncing in gravity above a totally reflecting glass mirror. Already from the raw data it was clear that the spatial resolution achieved in the detection and data correction process was as good as a few micrometers, quantitative analysis then revealed a resolution as good as approximately 2 μm.

Two measurements of this kind have been made, but one of them contains so low a number of neutron counts that it is practically useless when it comes to interpretation of the experiment, as the uncertainties on the measured distribution are too large to allow any conclusive analysis regarding its shape. However, the other detector contained much higher statistics and a very valuable dataset could be extracted from it.

We have developed a complete quantum mechanical model of the waveguide and presented a new way of computing the starting populations of the eigenstates. The latter takes in account the density of states at the location of the waveguide entrance and leads to a phase space factor which causes the eigenstates to have unequal starting populations. With this effect taken into account, the model yields a prediction for the neutron height distribution above the mirror surface which is in good agreement with the measurement.

In order to rule out a possible misinterpretation of the dataset, we have developed two alternative theoretical models of the measurement. The first assumes that the neutrons propagate along the waveguide as point like particles governed by the laws of classical mechanics. It has been realised using a Monte-Carlo simulation. The second consists of a quantum mechanical description in which the gravitational potential is neglected, i.e. in which the eigenstates of neutrons in the waveguide correspond to those of free particles.

It was found that the gravityless view cannot describe the measured height distribution in even a qualitative way and that it can be rejected without any doubt. Fitting of the classical prediction showed that it is able to qualitatively describe the higher energetic part of the dataset, while it fails at heights above the mirror of less than about 20 μm. In a quantum mechanical view, this behaviour is expected, as for large quantum numbers the system should, according to Bohr's Principle, behave semi-classically.

Although the classical description fits the data better than the gravityless one, only the complete quantum mechanical model – including gravity – can pass a quantitative statistical test. Thus we conclude that the measurement provides strong evidence for quantised motion of neutrons in the Earth's field of gravity, as has already been observed via integral flux measurements using our setup [Nesv02].

We have studied the possibility of deriving upper limits on short-ranged Yukawa type admixtures to the linear gravitational potential. Such deviations are predicted by a number of theories aiming at a quantum description of gravity [Ark98] [Ark99]. The analysis yields that, in the present situation, the limits derived from neutron height distribution measurements can only be as good than those already obtained through integral flux measurements.

Bibliography

[Abe02] H. Abele *et al.*, *Is the Unitarity of the Quark-Mixing CKM Matrix Violated in Neutron β-Decay?*, Physical Review Letters, Volume 88 (2002)

[Abe03] H. Abele, S. Baeßler, A. Westphal, *Quantum States of Neutrons in the Gravitational Field and Limits for Non-Newtonian Interaction in the Range between 1 μm and 10 μm*, Lecture Notes in Physics, Volume 631, Springer (2003)

[Abe05] H. Abele, private communication (2005)

[Ark98] N. Arkani-Hamed, S. Dimopoulos, G. Dvali, *The Hierarchy Problem and New Dimensions at a Millimeter*, Physics Letters B, Volume 429 (1998)

[Ark99] N. Arkani-Hamed, S. Dimopoulos, G. Dvali, *Phenomenology, Astrophysics, and Cosmology of Theories with Submillimeter Dimensions and TeV Scale Quantum Gravity*, Pysical Review D, Volume 59, (1999)

[Flü99] S. Flügge, *Rechenmethoden der Quantentheorie*, Springer (1999)

[Gähl89] R. Gähler *et al.*, Nuclear Instruments and Methods, Volume A289 (1989)

[Gol91] R. Golub, D. Richardson, S. K. Lamoreaux, *Ultra-Cold Neutrons*, Adam Hilger (1991)

[Han02] J. Hansson *et al.*, *Critique of an Experiment Regarding Quantum States in a Gravitational Field and Possible Geometrical Explanations*, arXiv:quant-ph/0206034 (2002)

[Han03] J. Hansson *et al.*, *Comment on "Measurement of Quantum States of Neutrons in the Earth's Gravitational Field"*, Physical Review D, Volume 68 (2003)

[Hoy04] C. D. Hoyle *et al.*, *Sub-Millimeter Tests of the Gravitational Inverse-Square Law*, arXiv:hep-ph/0405262 (2004)

[Nahr05] S. L. Nahrwold, *Development of a Detector for Bound Quantum States of Neutrons in the Earth's Gravitational Field*, Diploma Thesis, Heidelberg (2004)

[Nesv02] V. Nesvizhevsky, H. Abele *et al.*, *Quantum States of Neutrons in the Earth's Gravitational Field*, Nature, Volume 415 (2002)

[Nesv03] V. Nesvizhevsky *et al.*, *Reply to "Comment on 'Measurement of Quantum States of Neutrons in the Earth's Gravitational Field' "*, Physical Review D, Volume 68 (2003)

[Nesv04] V. Nesvizhevsky, K. Protasov, *Constraints on Non-Newtonian Gravity from the Experiment on Neutron Quantum States in the Earth's Gravitational Field*, arXiv:hep-ph/0401179 (2004)

[Nesv05] V. Nesvizhevsky *et al.*, *Study of the Neutron Quantum States in the Gravity Field*, European Physical Journal C, Volume 40 (2005)

[Nesv05b] V. Nesvizhevsky, private communication (2005)

[Pdg04] The Particle Data Group, http://pdg.lbl.gov (2004)

[Roc05] S. Roccia, private communication (2005)

[Rueß00] F. Rueß, *Quantum States in the Gravitational Field*, Diploma Thesis, Heidelberg (2000)

[Schwa98] F. Schwabl, *Quantenmechanik I*, Springer (1998)

[Vor05] A. Voronin *et al.*, *Quantum Motion of a Neutron in a Wave-Guide in the Gravitational Field*, arXiv:quant-ph/0512129 (2005)

[Wes99] A. Westphal, *Rapport de stage*, ILL (1999)

[Wes01] A. Westphal, *Quantum Mechanics and Gravitation*, Diploma Thesis, Heidelberg (2001)

[Wes04] A. Westphal, private communication (2004)

[Wes06] A. Westphal, to be published (2006)